Universidad del País Vasco Euskal Herriko Unibertsitatea

NAZIOARTEKO BIKAINTASUN CAMPUSA
CAMPUS DE EXCELENCIA INTERNACIONAL

PhD Thesis

Virtual sensing of large machines for remaining useful life oriented to the fatigue problem.

Presented by:

Bartomeu Mora Torres

in

Departamento de Ingeniería Mecánica

of the

Universidad del País Vasco

To obtain the degree of:

Doctor

Directed by:

Prof. Dr. Joseba Albizuri Irigoyen y Dr. Urko Leturiondo Zubizarreta

Bilbao, in 13 of july of 2024

ACKNOWLEDGMENTS

The research carried out in this thesis has been done in Ikerlan S. Coop, a research center member of the Basque Research and Technology Alliance, in collaboration with the University of the Basque Country (UPV-EHU). I would like to thank these organisations for making possible this thesis.

I would like to thank in first place Jon Basurko, the direct supervisor of this thesis, for his work, help and advice throughout the years that this work has lasted. I would also like to thank the directors of this thesis, Urko Leturiondo and Joseba Albizuri, for their help and supervisory work.

I wish to express my gratitude to Iman Sabahi, from KU Leuven (Belgium), coauthor of one of our publications, for their help and collaboration with the first study case of this thesis and its corresponding article. I wish also to express my gratitude to Mikel Escalero, Eneko Lorenzo, Mario Álvarez and Giovanna Calvín for their collaboration with the second study case of this thesis. Also, my gratitude with Juan Manuel Pagalday, research supervisor of Ikerlan, for all the advice provided over these years.

I am grateful to my colleagues from Monitoring and Mechanical Reliability departments of Ikerlan. Special thanks David Cubillas, Rocío Mingorance, Diego Sandoval, Javier Anduaga, Marcos Aguirre, Jorge Rodríguez, Josep Rueda, Héctor Martín, Estela Nieto, Rafael Espadas, Rafael Gago and Marcos Rodríguez for their help throughout the years that this thesis has lasted.

Finally, I would like to thank my family for the support after all these years.

Bartomeu Mora Torres

Arrasate-Mondragón, 2024

ABSTRACT

Virtual Sensing are techniques that allow to estimate measurement data at unmeasured points of a system, by combining the use of a model of the system with data from real sensors. These techniques are useful when integrated into Condition Monitoring and Structural Health Monitoring systems because they allow to obtain measurements at points where installing sensors is not feasible, and because they allow to reduce the number of real sensors in structures and industrial machines.

In this thesis, different model-based virtual sensing algorithms are selected and tested in different use cases, with the aim of obtaining strain/stress estimations. Some of these algorithms are taken from the existing bibliography and others are adaptations based on existing algorithms. Deterministic algorithms (like the Direct Strain Observer and the Least Squares Strain Estimation) and stochastic algorithms (like the Kalman filter, Augmented Kalman filter and Static-Strain Kalman filter) are implemented in different use cases working under conditions of unmeasured loads (which results of special interest, since in many cases it is not possible to measure the external loads on a system). For the implementation of the VS algorithms, reduced models are extracted from much more detailed Finite Element Methods models.

The first use case consists of a scale prototype of an offshore wind turbine, where an inertial shaker is installed in the nacelle to replace mass components (such as the generator or gearbox). The shaker allows to excite the turbine in different directions. The applied loads generate dynamic effects in the prototype, with the aim of studying the performance of the virtual sensing algorithms under these conditions.

The second use case consists of a scaled prototype of a bed press. Cyclic loads are applied to the prototype using a fatigue test machine, in order to cause a fatigue break due to accumulated damage at critical points. In this study case, first is evaluated that if reliable strain estimations can be obtained with the tested virtual sensing algorithms, and then the accumulated fatigue damage at critical points is estimated using virtual measurements.

Results show that it is possible to obtain satisfactory virtual strain/stress measurements without measuring external loads, both in cases of static/quasistatic loads and in cases of dynamic loads, using a model extracted from a FEM model and a limited number of strain gauges as input sensors. Results also show that obtained virtual strain/stress measurements can be used to estimate accumulated fatigue damage at critical points of a monitored system. The results and knowledge obtained in this thesis can be useful to facilitate the monitoring of industrial equipment and structures, helping to reduce maintenance costs and increasing safety.

RESUMEN

Se conoce como sensorización virtual (en inglés, *virtual sensing*) al conjunto de técnicas que, aplicadas a un sistema como una máquina industrial o una estructura, permiten estimar medidas en puntos no directamente medidos con sensores. Para ello, las técnicas de sensorización virtual combinan modelos del sistema con medidas reales disponibles. Estas técnicas resultan de gran utilidad integradas en sistemas de *Condition Monitoring* (CM, aplicadas sobre todo en maquinaria industrial y vehículos) y *Structural Health Monitoring* (SHM, aplicadas sobre todo en estructuras e ingeniería civil), porque permiten obtener medidas en puntos donde no sería posible instalar un sensor real (por diversos motivos como falta de espacio, condiciones advers, etc) y también porque permiten reducir el número de sensores reales en un sistema de monitorización (con la consecuente reducción de costes que ello supone).

Hasta el día de hoy se han planteado muchos métodos distintos de sensorización virtual, clasificándose principalmente en métodos basados en datos (*data-driven*) y métodos basados en modelos físicos (*model-based*), habiendo también métodos híbridos que combinan los dos anteriores. Los métodos basados en datos (los cuales incluyen redes neuronales o regresiones de distintos tipos) no requieren de un conocimiento profundo de la física del sistema, pero requieren en cambio de grandes cantidades de datos reales de ejemplo como entrenamiento, estando su funcionamiento en parte limitado por los datos de entrenamiento utilizados. Por el contrario, los métodos basados en modelos físicos (los cuales incluyen filtros de Kalman y similares, o métodos basados en mínimos cuadrados) sí requieren de un conocimiento profundo de la física del sistema para construir el modelo, pero una vez planteados son capaces de cubrir una gran cantidad de escenarios, así como adaptarse más fácilmente a posibles cambios en el sistema real.

En esta tesis, diferentes métodos de sensorización virtual basados en modelos físicos son implementados y comparados entre sí, con el objetivo de estimar deformaciones y tensiones en puntos no medidos. Dentro del contexto de sistemas de

CM y SHM, la estimación de estas magnitudes resulta de especial interés para los cálculos relacionados con fatiga de materiales.

Tras revisar en la bibliografía muchas aplicaciones de sensorización virtual, se ha llegado a varias conclusiones. En primer lugar, que no existe un claro consenso sobre qué métodos de sensorización virtual son los más adecuados para implementarse en cada situación. En segundo lugar, que si bien la sensorización virtual ya está hoy en día bastante extendida en la monitorización de grandes estructuras (sistemas SHM), su uso en maquinaria industrial (sistemas CM) está mucho menos extendido. En último lugar, en muchas aplicaciones de sensorización virtual, los métodos utilizados requieren de medir las fuerzas o cargas externas sobre el sistema, suponiendo esto un limitante o dificultad añadidos en circunstancias habituales.

A partir de las conclusiones expuestas en el párrafo anterior, se define el propósito de esta tesis como la investigación de sensorización virtual para estimación de deformación y tensión en puntos no sensorizados. Para ello, se han instalado sensores virtuales en dos casos de uso, consistentes en dos prototipos a escala (en representación a dos aplicaciones industriales diferentes).

En base al propósito definido en el párrafo anterior, se enumeran los siguientes objetivos:

· Proponer algunas variaciones de los métodos de sensorización virtual existentes, específicamente orientadas a la estimación de deformaciones en condiciones de fuerzas externas no medidas. La idea es que estos métodos propuestos permitan simplificar la obtención de mediciones de deformación virtuales en diferentes aplicaciones.

· Testear diferentes métodos de sensorización virtual utilizando dos prototipos a escala (un prototipo de turbina eólica offshore y un prototipo de cama de prensa industrial) con el objetivo de obtener estimaciones de deformación en puntos no medidos. La idea es estudiar y comparar el rendimiento de los métodos de

sensorización virtual testeados en condiciones de fuerza externas no medida y utilizando diferentes configuraciones de sensores de entrada.

· Probar diferentes métodos de sensorización virtual en condiciones de fuerzas estáticas/ cuasiestáticas y de fuerzas dinámicas, con el fin de estudiar su desempeño bajo diferentes condiciones de carga que impliquen diferentes tipos de excitaciones en los casos de uso testeados.

· Estudiar si las estimaciones de tensión y deformación obtenidas con los métodos de sensorización virtual testeados son útiles para estimar el daño por fatiga acumulado. Para ello, uno de los casos de uso (el correspondiente al prototipo de cama de prensa industrial) es sometido a un ensayo de fatiga, con el objetivo de validar experimentalmente las estimaciones de fatiga obtenidas con los sensores virtuales (tanto en daño acumulado como en localización de los puntos críticos)

La investigación llevada a cabo en esta tesis tiene ciertas limitaciones, las cuales se enumeran a continuación:

· Esta tesis se centra en métodos de sensorización virtual basados en modelos, ya que se considera que son más adecuados para los casos de uso presentados. Por lo tanto, no se han testeado métodos de sensorización virtual basados en datos.

· El objetivo de los métodos de sensorización virtual testeados en esta tesis es la estimación de medidas de deformación en puntos no medidos. Conociendo las propiedades del material, puede conocerse la tensión a partir de las medidas de deformación. Si bien la sensorización virtual está centrada en la estimación de deformación/tensión, también se podrían estimar otras medidas como desplazamiento o aceleración.

· Se asume que el comportamiento de los prototipos utilizados como casos de uso es lineal e invariante en el tiempo (LTI). Por lo tanto, se utilizan métodos de sensorización virtual que requieren de modelos lineales que no varían.

· Para la estimación de fatiga acumulada mediante señales virtuales de deformación, se utilizan métodos clásicos de fatiga: cuenta de ciclos con algoritmo Rainflow y daño acumulado mediante ley de Palmgren-Miner. Se utiliza el enfoque High-Cycle fatigue. No se utilizan otros métodos de análisis fatiga.

En el trabajo desarrollado en esta tesis, diferentes algoritmos de sensorización virtual han sido implementados, todos ellos basados en modelos físicos, los cuales se enumeran a continuación.

En primer lugar, se ha adaptado un observador directo de deformación (DSO), consistente en el uso de un modelo reducido obtenido a partir de un modelo de elementos finitos, alimentado con las mismas fuerzas externas que el sistema real, del cual se obtienen estimaciones de deformación. La necesidad de medir las fuerzas externas supone un limitante en muchos casos.

En segundo lugar, se ha desarrollado un estimador de deformación basado en ajuste de mínimos cuadrados (en inglés, *Least Squares Strain Estimator* o LSSE), un método de tipo determinístico que permite estimar un conjunto de deformaciones en puntos no medidos a partir de un modelo reducido obtenido de un modelo de elementos finitos, y un número limitado de mediciones de deformación.

En último lugar, se han implementado varias variaciones del filtro de Kalman para la estimación de deformaciones, algoritmos recursivos de tipo Bayesiano que hacen uso de un modelo en espacio de estados (obtenido a partir de un modelo reducido obtenido a partir de un modelo de elementos finitos) y un número limitado de medidas de sensores. Los filtros de Kalman son métodos de tipo estocástico, ya que pueden gestionar las incertidumbres asociadas al sistema y a las medidas introducidas. En esta tesis se han implementado tanto el Filtro de Kalman convencional (KF) como el Filtro de Kalman Aumentado (AKF) (una variación que considera las fuerzas externas sobre el sistema como estados del modelo), además de haberse desarrollado una simplificación llamada *Static Strain Kalman filter* (SSKF)

únicamente para la estimación de deformación en sistemas sometidos a cargas estáticas o cuasiestáticas.

Todos los algoritmos anteriormente enumerados requieren de la obtención de modelos de orden reducido, para poder ofrecer resultados con mayor agilidad (incluso en *real-time*). Para ello, en esta tesis se describen varias técnicas de reducción de modelos, como la condensación estática de Guyan, la condensación de Craig-Bampton o la truncación modal.

En el primer caso de uso, en un prototipo de aerogenerador offshore a escala, los métodos LSSE, KF y AKF son implementados para obtener estimaciones de deformación en puntos no medidos, a partir de señales de aceleración y deformación. El prototipo se encuentra sometido a fuerzas que crean efectos dinámicos, aplicadas mediante un oscilador electromagnético ubicado en la parte superior del mismo. Las señales estimadas obtenidas son comparadas con señales reales obtenidas con sensores ubicados en esos puntos, para verificar el funcionamiento de los algoritmos testeados bajo distintos tipos de fuerza y utilizando diferente número y tipo de sensores de entrada. Tras la realización de los experimentos, se observa que se obtienen buenos resultados utilizando los algoritmos LSSE y AKF.

En el segundo caso de uso, en un prototipo de cama de prensa industrial, los métodos DSO, LSSE y SSKF son implementados para obtener estimaciones de tensión en los puntos críticos identificados en el mismo, con el objetivo de estimar el daño acumulado por fatiga en estos puntos. Se utilizan galgas de deformación como señales de input (excepto en el caso del DSO, donde la señal de fuerza aplicada es utilizada como input). El prototipo es ensayado a fatiga mediante la aplicación de cargas cíclicas (de naturaleza quasiestática). Tras la realización del experimento, se observa que se obtienen resultados ajustados estimando la iniciación de grieta (tanto el punto de aparición como el número de ciclos) utilizando las tensiones estimadas con los algoritmos LSSE y SSKF.

En conclusión, se considera que se cumplen los objetivos de la tesis.

LABURPENA

Sentsorizazio birtuala (ingelesez, virtual sensing) makina industrial edo egitura bati aplikatuz, zuzenean sentsoreen bidez neurtzen ez diren puntuetan neurketak zenbatesteko (estimatzeko) aukera ematen duen tekniken multzoa da. Horretarako, sentsorizazio birtualeko teknikek sistemaren ereduak eta beste puntu batzuetan lortutako neurri errealak konbinatzen dituzte. Teknika horiek oso erabilgarriak dira Condition Monitoring (CM, batez ere industria-makinetan eta ibilgailuetan aplikatuak) eta Structural Health Monitoring (SHM, batez ere egituretan eta ingeniaritza zibilean aplikatuak) sistemetan integratuta; izan ere, sentsore errealik instalatu ezin den puntuetan neurketak lortzeko aukera ematen dute (dela leku falta, baldintza desegokiengatik, etab.), eta, gainera, beharrezkoak diren sentsore kopurua murriztu dezakete, monitorizazio sistema merketuz.

Gaur egun arte, sentsorizazio birtualeko metodo asko planteatu dira, eta, nagusiki, datuetan oinarritutako metodoetan (data-driven) eta eredu fisikoetan oinarritutako metodoetan (model-based) sailkatu dira. Aurreko biak konbinatzen dituzten metodo hibridoak ere badaude. Datuetan oinarritutako metodoek (neurona-sareak edo mota desberdinetako erregresioak barne hartzen dituztenak) ez dute sistemaren fisika sakonki ezagutu beharrik, baina, datu erreal asko behar dituzte entrenamendu gisa, eta, hein batean, haien funtzionamendua mugatuta dago erabilitako entrenamendu-datuen egoeratara. Aitzitik, eredu fisikoetan oinarritutako metodoek (Kalmanen iragazkiak eta antzekoak dituztenak, edo karratu txikienen araberako metodoak) sistemaren fisika sakon ezagutu behar dute eredua sortu ahal izateko, baina, planteatu ondoren, gai dira eszenatoki asko estaltzeko eta sistema errealeko aldaketetara errazago egokitzeko.

Tesi honetan, eredu fisikoetan oinarritutako sentsorizazio birtualeko hainbat metodo erabili eta konparatzen dira, neurtu gabeko puntuetan deformazioak eta tentsioak zenbatesteko. CM eta SHM sistemen testuinguruan, magnitude horien zenbatespena bereziki interesgarria da materialen nekearekin lotutako kalkuluetarako.

Bibliografian sentsorizazio birtualeko hainbat aplikazio aztertu ondoren, ondorio batzuk atera dira. Lehenik eta behin, ez dago adostasun argirik sentsore birtualeko zein metodo diren egokienak egoera edo baldintza bakoitzean. Bigarrenik, sentsorizazio birtuala egitura handien (SHM sistemak) monitorizazioan nahiko hedatuta dagoen arren, askoz gutxiago erabiltzen da industria-makinetan (CM sistemak). Azkenik, sentsorizazio birtualeko aplikazio askotan erabiltzen diren metodoek sistemaren sarrera (inputa) neurtu beharra dute, eta hori mugatzailea edo zailtasun erantsia da zenbait egoeratan.

Aurreko paragrafoan azaldutako ondorioetatik abiatuta, tesi honen xedea, sentsorerik gabeko puntuetan deformazioa eta tentsioa zenbatesteko sentsorizazio birtualen ikerketa gisa definitzen da. Horretarako, bi erabilera-kasutan sentsore birtualak erabili dira: eskalan egindako bi prototipo, bi industria-aplikazio desberdinen ordezkari direnak.

Aurreko lerroaldean zehaztutako xedean oinarrituta, helburu hauek ezarri dira:

· Sentsorizazio birtualeko metodoen bariazio batzuk proposatzea, bereziki kanpoko indarren neurketa gabe deformazioak zenbatestera bideratuta daudenena. Proposatutako metodo horiek deformazio-neurketa birtualak hainbat aplikaziotan lortzen erraztea da asmoa.

· Sentsorizazio birtualeko hainbat metodo probatzea, eskalan egindako bi prototipo erabiliz (offshore turbina eoliko batena bata eta prentsa industrialeko ohe batena bestea), neurtu gabeko puntuetan deformazio-estimazioak lortzeko. Sentsorizazio birtualeko metodoen errendimendua aztertu eta alderatu nahi da, neurtu gabeko kanpoko indar-kondizioetan testeatuta eta sarrera-sentsoreen konfigurazio desberdinak erabiliz.

· Sentsorizazio birtualeko hainbat metodo probatzea indar estatiko/kuasiestatikoen eta indar dinamikoen eraginpean, kitzikapen-mota desberdinen aurrean beraien jokabidea aztertuz, aurkeztutako erabilera-kasuen bidez.

· Aztertzea, ea sentsorizazio birtualeko metodoen bidez lortutako tentsio- eta deformazio-zenbatespenak erabilgarriak diren nekeak eragindako kalteak egoki iragartzeko. Horretarako, erabilera-kasu batean (prentsa industrialeko ohe-prototipoari dagokiona) neke-entsieu bat egin da, sentsore birtualekin lortutako neke-zenbatespenak esperimentalki baliozkotzeko (bai metatutako kalteari dagokionez, bai puntu kritikoen kokapenari dagokionez).

Tesi honetan egindako ikerketak zenbait muga ditu. Hona hemen:

· Tesi hau, sistemen eredu fisikoetan oinarritutako sentsorizazio birtualeko metodoetara zuzenduta dago, aurkeztutako erabilera-kasuetarako egokienak direla uste baita. Beraz, ez da testatu datuetan oinarritutako sentsorizazio birtualeko metodorik.

· Tesi honetan jasotako sentsorizazio birtualeko metodoen helburua neurtu gabeko puntuetan deformazio-neurriak zenbatestea da. Materialaren propietateak ezagututa, deformazio-neurrien bidez tentsioa ere jakin daiteke. Deformazioa eta desplazamendua elkarrekiko estuki lotuta egonik, desplazamenduak modu beretsuan zenbatestu daitezke. Beste neurri-mota batzuk (abiadura, azelerazioak edo indarrak, esaterako) esku artean erabilitako zenbait metodorekin zenbatestu ahal badira ere, ez da arreta puntu nagusia izan.

· Erabili diren prototipoen portaera denboran zehar aldatzen ez dela eta lineala dela onartzen da. Beraz, eredu hauetara mugatutako sentsorizazio birtualeko metodoak aztertu dira.

· Deformazio-seinale birtualen bidez metatutako nekea zenbatesteko, ziklo kopuru ugarira zuzendutako neke-metodo klasikoak erabili dira, hara nola, Rainflow algoritmoa (tentsioaren ziklo-kontua egin ahal izateko) eta Palmgren-Miner legea (neke metatuazenbatzeko).

Tesi honetan egindako lanean, sentsorizazio birtualeko algoritmo batzuk landu dira, guztiak eredu fisikoetan oinarrituak. Hona hemen:

Lehenik eta behin, zuzeneko deformazio-behatzaile bat (ingelesez, Direct Strain Observer) landu da, sistemaren elementu finitu bidezko eredu xehe batetik lortutako eredu murriztu bat erabiltzean datzana. Sistema errealaren kanpo-indarrak neurtuz, hauek behatzailea elikatzen dute eta eredu horretatik deformazio-zenbatespenak lortzen dira. Aurretik esan bezala, kanpoko indarrak neurtzeko beharra mugatzailea da kasu askotan.

Bigarrenik, minimo karratuen doikuntzan (ingelesez, Least Squares Strain Estimator edo LSSE) oinarritutako deformazio-zenbatesle bat landu da. Metodo deterministikoa da honako hau. Bi sarrera behar ditu, elementu finituen eredu xehe batetik lortutako eredu murriztua eta kopuru mugatu batean neurtutako deformazio-neurketak. Hauek edukiz gero, metodoak neurtu gabeko nahi beste puntuetako deformazioa zenbatesteko aukera ematen du.

Azkenik, deformazioak zenbatesteko, Kalman-en iragazkiaren zenbait moldaketa ezarri dira; hain zuzen, egoera-espazioko eredu bat (elementu finituen eredu xehe batetik lortutako eredu murriztu batetik abiatuta sortutakoa) eta sentsore-neurri kopuru mugatua erabiltzen duten Bayes motako algoritmo errekurtsiboak. Kalman-en iragazkiak metodo estokastikoak dira, sistemari eta sartutako neurriei lotutako ziurgabetasunak kudea baititzakete. Tesi honetan, Kalman Iragazki konbentzionala (Kalman Filter) eta Gehitutako Kalman Iragazkia (Augmented Kalman Filter) landu dira. Azken hau, Kalman Iragazkiaren eraldaketa da, eta sisteman eragiten duten kanpo indarrak egoera-espazio ereduko egoera gehigarri gisa hartzen ditu. Horrez gain, Kalman Static Strain Kalman filter (SSKF) izeneko sinplifikazioa garatu da karga estatiko edo kuasi-estatikoak dituzten sistemen deformazioa zenbatesteko.

Arestian aipatutako algoritmo guztiek ordena murriztuko ereduak lortzea eskatzen dute, emaitzak bizkorrago eskaini ahal izateko (baita real-timean ere). Horretarako, tesi honetan eredu estrukturalak murrizteko zenbait teknika deskribatzen dira, hala nola Guyanen kondentsazio estatikoa, Craig-Bampton-en kondentsazioa edo modoen trunkazioa.

Lehenengo erabilera-kasuan, offshore aerosorgailuaren eskala-prototipo batean, LSSE, KF eta AKF metodoak erabili dira neurtu gabeko puntuetan deformazio-estimazioak lortzeko, azelerazio- eta deformazio-seinaleetatik abiatuta. Prototipoa efektu dinamikoak sortzen dituzten indarren mende dago, haren goiko aldean dagoen osziladore elektromagnetiko baten bidez aplikatuak. Kalkulatutako seinaleak puntu horietan kokatutako sentsoreen bidez lortutako seinale errealekin konparatu dira, hainbat indar-motaren arabera testatutako algoritmoen funtzionamendua egiaztatzeko eta sarrera-sentsore mota eta kopuru desberdinak erabiliz. Esperimentuak egin ondoren, emaitza onak lortu dira LSSE eta AKF algoritmoak erabiliz.

Bigarren erabilera-kasuan, industria-prentsako ohe-prototipo batean, DSO, LSSE eta SSKF metodoak bertan identifikatutako puntu kritikoetan tentsio-estimazioak lortzeko erabili dira, puntu horietan nekeak eragindako kalteak zenbatesteko. Deformazio-galgak erabili dira sarrera-seinale gisa (DSOren kasuan izan ezik, kasu horretan aplikatutako indar-seinalea input gisa erabili beharra dagoelako). Prototipoa nekean probatzen da karga ziklikoak aplikatuz (karga kuasi-estatikoak). Esperimentua egin ondoren, emaitza doituak lortu dira arrailduren hastapena zenbatetsiz (bai agertze-puntua, bai ziklo-kopuruari dagokienez), LSSE eta SSKF algoritmoekin zenbatetsitako tentsioak erabiliz.

Guzti honengatik, tesiaren helburuak betetzen direla uste da.

INDEX

FIGURE INDEX

TABLE INDEX

ACRONYMS

AKF	Augmented Kalman Filter virtual sensing algorithm
CAD	Computer Assisted Design
CB	Craig-Bampton model reduction method
CM	Condition Monitoring
DoF	Degree of Freedom
DSO	Direct Strain Observer virtual sensing algorithm
e%	percent error
EKF	Extended Kalman Filter virtual sensing algorithm
ENS	Effective Notch Stress method
FEM	Finite Element Methods
GR	Guyan Reduction method
HSS	Hot Spot Stress method
IIW	International Institute of Welding
KF	Kalman Filter virtual sensing algorithm
LCF	Low Cycle Fatigue
LSSE	Least Squares Strain Estimation virtual sensing algorithm
MAC	Modal Assurance Criterion
MCK	Mass-Spring-Damping model
MEM	Modal Expansion Method
MEMS	Micro Electromechanical System
MKE	Modal Kinetic Energy
NI	National Instruments corporation
NN	Neural Network
ODE	Ordinary Differential Equation
OWT	Offshore Wind Turbine
PCC	Pearson Correlation Coefficient
RRMSE	Relative Root Mean Square Error

SDS	Static Deflection Shape
SHM	Structural Health Monitoring
SMR	Static Modal Reduction method
SN	Stress life fatigue curve
SSKF	Static Strain Kalman Filter virtual sensing algorithm
UKF	Unscented Kalman Filter virtual sensing algorithm
VS	Virtual Sensing

SECTION 1

Introduction and theoretical content

Chapter 1

INTRODUCTION AND OBJECTIVES

This chapter is structured in six subchapters. In *1.1*, the state of the art of the developments of this thesis is described. In *1.2*, the problems detected analyzing the background are described. In *1.3*, the purpose and objective of this thesis are explained. In *1.4*, the scope and limitations of this thesis are detailed. In *1.5*, a general outline of the contents of the thesis is presented, and in *1.6*, the main developments of this thesis are remarked.

1.1 State of the art

Structural Health Monitoring (SHM) is the process of permanently sensing and monitoring structural facilities during its useful life, with the aim of estimating its condition and detecting anomalies that may indicate the presence of damage or degradation [1], [2]. Condition Monitoring (CM) is the equivalent process but applied to industrial machines, vehicles, and similar equipment [3], [4].

One of the main functions of CM and SHM systems is fatigue monitoring. Material fatigue (the phenomenon that causes the fracture of materials due to cyclic loads) has been a main issue since it was described at the beginning of the industrial era, in the 19th century. Since then, the study of fatigue has been a main topic of research in engineering, evolving in parallel with technological development and adapting to the arising needs (such as aeronautics, motorized transport, civil engineering, etc.). Throughout the 20th century, great advances were made in the study of fatigue and in the implementation of solutions to mitigate its effects [5]. In 1982, a study funded by the US Department of Commerce determined that the problems caused by fatigue had an annual imapct of 119 billion dollars in the US economy, plus a significant number of lives lost due to accidents. The same study estimated that up to 28 billion dollars per year could be saved in the future if more research on fatigue were made and preventive measures against it were implemented [6].

The implementation of SHM and CM systems in large civil and industrial facilities can provide important benefits [7]. Through the lifetime approach (calculating the

accumulated fatigue in critical areas), it is possible to update the remaining useful life of the structure, making possible a safe extension of the service life [8]. Through the damage detection approach, it is possible to identify degradation and damage in components or critical areas of the structure, making possible preventative repairs or component replacements in order to avoid significant breakdowns [9]. Both approaches suppose, on the one hand, an increase in the safety of the monitored facilities, and in the other hand, economical savings due to the optimization of maintenance actions and the extension of the service life. For example, in the aeronautical sector, some sources indicate that the application of CM systems in commercial airplanes can result in savings from 30 to 60% in maintenance costs [10]. In the wind energy sector, some sources estimate that the application of SHM systems in offshore wind turbines can lead in estimated savings between 11 and 18 million € (at 2019) in a wind farm per year [11] (see **Figure 1-1**)

Figure 1-1 a*rtistic representation of an offshore wind farm. Source: https://commons.wikimedia.org/*

For both abovementioned approaches, the measurement of strain or stress cycles at critical areas or components of a structure results of special interest [12], [13]. The strain is a relative and dimensionless measure of the change in dimensions of a solid material as a response to external loads. The stress is the distribution of loads inside a material in response of the external loads applied to it, having units of load divided by area. Assuming a material with linear elastic behaviour, strain and stress are related by factors specific to each material (Young elastic modulus, shear modulus and Poisson coefficient). By measuring the strain in a structure, it is possible to estimate the accumulated fatigue (allowing to update the estimated remaining useful life of the structure) and also to detect behaviour changes that may indicate the presence of damage. The accumulated fatigue can be estimated using both strain-life and stress-life fatigue approaches because, knowing the properties of the material of the structure, stress can be directly obtained from strain measurements [14]. Strain-life approaches are commonly used for low cycle fatigue, where plastic and elastic deformation effects are both present. Stress-life approaches are instead commonly used for high cycle fatigue, where only elastic deformation effects are present [15].

Often, it is not possible to obtain direct strain measurements in certain areas of a structure, because placing a sensor in those areas is not technically feasible (due to harsh environment, or lack of accessibility) or because it is necessary to measure a large number of points (not being feasible to locate a sensor in all of them) [16], [17]. For this reason, in SHM and CM systems, Virtual Sensing (VS) methods can be applied, which consist of estimating measurements at locations where real sensors are not installed. VS techniques work with information of the system and real data from sensors located at other points of the system. In SHM and CM, the implementation of virtual sensors is especially useful, because not only allows to obtain data from points where is not possible to install real sensors, but also because it can mean a reduction in the number of sensors needed to monitor the structure, with the cost reduction that this entails [18].

The methods can be classified into three main categories [19]: data-driven methods (also known as empirical methods or black-box methods), model-based methods (also known as parametric or white-box methods) and hybrid methods (also known as gray-box methods).

Data-driven VS methods do not use physical parameters, but numerical relations between input and output data extracted of the system. In VS data-driven approaches neural networks (NN) are frequently used [19], [20], even if there are also alternative methods to them, such as random forest or different types of regression models.

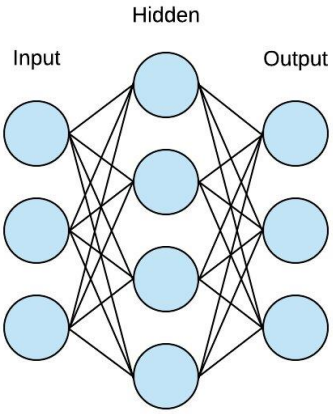

Figure 1-2 *Simplified diagram of a neural network* [21]

NN are artificial intelligence algorithms that consist of complex networks of nodes (neurons) adjusted using training data, which relates the provided input data with the desired outputs (see **Figure 1-2**). Artificial Neural Networks (ANN) and Convolutional Neural Networks (CNN) have been used for VS applications [22], [23]. ANN are simpler, because inputs are processed only in forward direction, while CNN are more complex because use multiple types of layers for processing the provided input data. The main advantage of this type of algorithms is that they do not require the implementation of models of the system. The main drawback is that, in order to create a data-driven model, important amounts of operational sensor data from the real structure must be provided as training data. Another drawback of this

type of models is that is not possible to vary specific parameters in order to update or change the model. Instead, the data-driven model must be rebuilt with new data.

Random Forest (RF) is an artificial intelligence algorithm alternative to NNs based on decision trees, each of them trained with subsamples of randomly selected data. RFs can work with less training data than NN (thus avoiding overfitting problems) if the provided data is more characterized. On the contrary, RFs are less flexible than NN and they have more difficulty finding complex patterns [24].

Regression algorithms are data-driven methods also used in VS applications. Just like the methods previously described, regressions are based on finding numerical relations between input data and output data, but in the case of regressions a simpler function is fitted, instead of complex networks of neurons or trees [24]. The modelling capability of regressions is generally much more limited [25]. Different types of regressions can be used in VS applications, some of them being the linear regression, the polynomial regression or the K-nearest neighbours regression [26].

The alternative to using data-driven VS methods is to use VS methods based on physical models (approach usually referred as parametric VS or white-box VS). These VS methods use models with parameters that represent the physical characteristics of the real structure. These models can be more complex to implement because they require more knowledge of the monitored system, but they allow to avoid the mentioned disadvantages of the data-driven methods [19].

In VS with physical models, both stochastic and deterministic algorithms are commonly used. One of the most known stochastic estimation algorithms is the Kalman filter (KF), a physics model-based algorithm proposed by R. Kalman in 1960 [27]. The KF uses a state-space model of the system to make state predictions (of mean and variance, assuming a Gaussian distribution) based on information from the previous states. The KF is then a Bayesian estimator [28], [29]. Input data from real sensors are used to correct the predictions and to update the algorithm parameters.

Some examples of the use of the KF for strain estimation are found in [30] and [31]. In both cases, the KF is used for strain estimation at unmeasured points, in the first reference in an offshore wind turbine and in the second reference in a sensorized beam in a laboratory. An implementation of the KF with an augmented state-space model (which estimates the inputs together with the states of the system) was first proposed in 1969 by B. Friedland [32], to perform a state estimation with unknown inputs. In 2010, E. Lourens et al. used the KF with the augmented state-space for dynamic loads identification, and the following year they consolidated the so-called augmented Kalman filter (AKF) [33], which has been used in later publications [34], [35]. Other variants of the KF for nonlinear systems have been proposed: for example, the Extended Kalman filter (EKF) [36], that performs a linearization of the estimated mean and covariance for each time step, or the Unscented Kalman filter (UKF) [37], that avoids linearization by applying an unscented transformation to the estimated mean and covariance. An alternative to the Kalman filter is the Particle filter (PF), which is also a stochastic Bayesian estimator [38]. For each time step, the PF generates multiple random estimations (particles) using Monte Carlo simulations. A weight is assigned to each particle, and the closest particles to the observation measurements are more weighted for the following time-steps.

Deterministic model-based VS algorithms also have been used for strain/stress estimation [12], [17], [38][39]. The use of a model in open-loop simulation (being known all the inputs on the system) to obtain estimations of measurements can be considered the simplest form of VS deterministic algorithm. Other approach of deterministic VS algorithm is the modal decomposition and expansion, which consists of describing the system using a set of modes, and from these obtain the full field of strains or stresses. In [12], this method is applied to a sensorized beam in a laboratory, and in [17] and [39] is used to obtain estimations of strain and stress for fatigue purposes in offshore wind turbines. Other example of a deterministic algorithm is the Dynamic Programming (DP), used for load identification. Some examples of application of the DP for VS purposes can be seen in [40] and [34].

Hybrid VS algorithms (also known as gray-box methods) are generally combinations of data-driven and model-based VS methods, which can be both serial and parallel [19].

As a summary, a general classification of VS algorithms can be seen in **Figure 1-3**. A main classification can be observed between data-driven, model-based and hybrid-methods. Within the model-based algorithms (which are the VS algorithms selected in this thesis), another classification can be made between deterministic and stochastic algorithms.

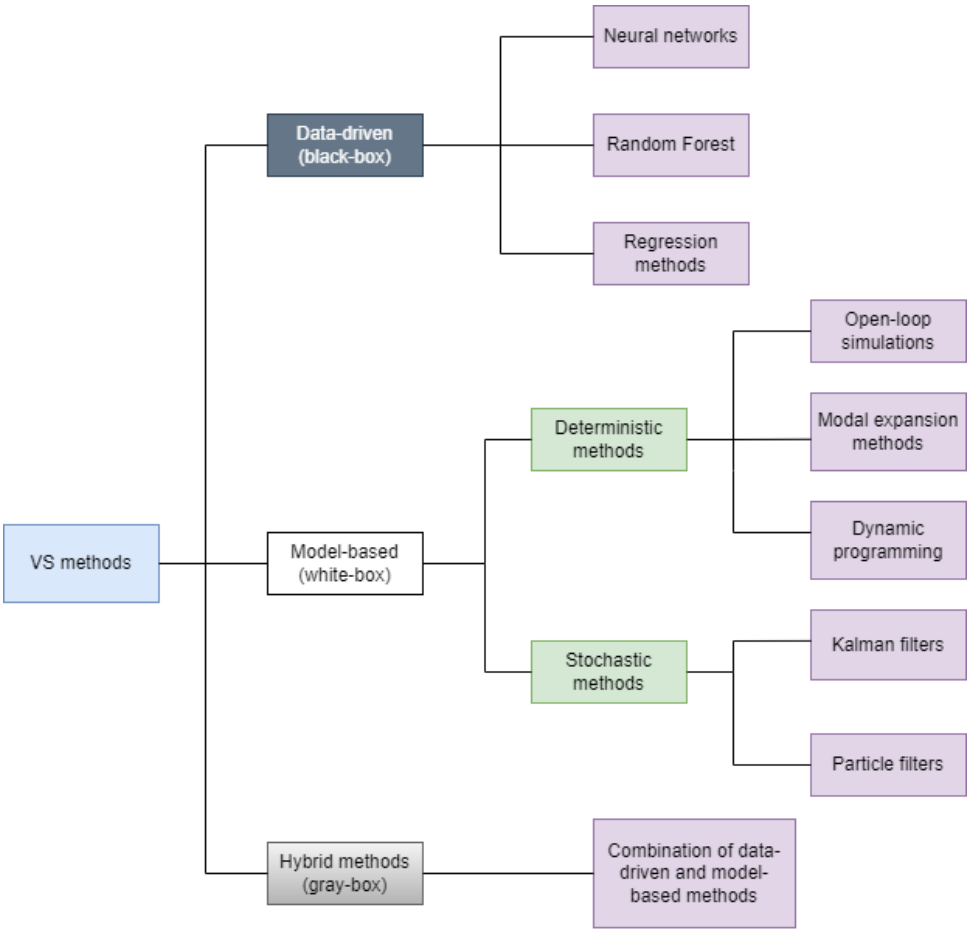

Figure 1-3 *Classification of VS algorithms.*

In recent years, many examples of application of virtual sensors can be found in the bibliography. Listed below are some of the applications of VS algorithms in SHM and CM systems found in recent years. The algorithms used, what input sensors they use, and the use case are indicated.

Different authors [41][42][41] used stress virtual sensors for fatigue estimation in a wind turbine support structure, using the AKF and a FEM model. Ren and Zhou [42] applied strain virtual sensors using the AKF, modal expansion and reduced models obtained from a FEM model. They used a scaled beam structure as use case, and strain sensors as inputs. Lourens and Fallais [43] used the KF and a modal truncated model for state, strain and load estimation using strain gauges and accelerometers as input sensors. They used a single beam as experimental prototype.

Ziegler et al. [44] reviewed different methods for VS to estimate loads over off-shore wind turbines, using a Craig-Bampton reduced model and strain gauges as input sensors. Branlard et al. [35] applied the AKF for load and state estimation in a wind turbine, using reduced-order models and accelerometers, turbine speed and generator torque as input sensors. Tarpo et al. [45] applied the modal expansion in combination with the SEREP reduction method to estimate strains and stresses in an offshore structure. Henkel et al. [39] used the modal expansion and a modal truncated model (obtained from a FE model) to estimate strains using strain gauges and accelerometers as input sensors in a monopile offshore wind turbine. Moghadam and Nejad [46] applied the modal expansion in a modal truncated model to obtain strain estimations in a monopile offshore wind turbine, using strain gauges as input sensors. Vettori et al. [47] used the AKF in combination with a modal truncated model (obtained from a FE model) for obtaining strain and input load estimations in a monopile offshore wind turbine, using strain sensors as input sensors.

Other implementations have used data-driven methods for applying virtual sensors in SHM systems. Azzam et al. [22] applied artificial neural networks for torque and load estimation in a wind turbine gearbox, using a multibody model and the gearbox

known parameters as input sensors. Puruncajas et al. [23] applied convolutional neural networks for damage estimation on a wind turbine scaled prototype using a FE model and accelerometers as input sensors.

Regarding CM systems, virtual sensors have been used in a wide variety of applications. Wang et al. [48] used data-based virtual sensors to monitor degradation status in gearboxes, using vibration data and oil debris sensors. Moi et al. [49] used virtual strain gauges for condition monitoring applied to cranes, using a scaled prototype for experimental validation. González [50] applied virtual sensors in elevators to estimate acceleration and loads on various components in his PhD thesis. Virtual sensors have also been applied in aircraft and automotive components, for example to estimate the external loads received on wheels and suspension systems [10], [51]. In the case of heavy industrial equipment such as presses and similar machines, CM systems have been occasionally used for fatigue monitoring and damage detection [52], [53], [54]. In these applications, the use of virtual sensors still seems uncommon, and few examples can be found. For example, Kurth et al. [55] applied strain virtual sensors in a digital-twin approach for CM in forming presses (see **Figure 1-4**).

Figure 1-4 *Example of an industrial press. Source: https://fagorarrasate.com/*

In conclusion, SHM systems are nowadays common in certain structural facilities. Wind turbines are one of the most common applications, and offshore structures and bridges are common applications too. Nowadays, the use of virtual sensors is quite common in SHM systems, being data-driven and model-based methods both commonly used. In the case of CM systems, the use of virtual sensors is less common.

Within the physical model-based methods, both stochastic algorithms (mainly variants of the Kalman filter) and deterministic algorithms (mainly least squares-based methods) are usually applied. Models are usually a reduced model obtained from a FE model. Different reduction methods are used, being the modal truncation one of the most used.

Acceleration and strain sensors are the most used input sensors in SHM systems and are also used in some CM systems. Strain gauges [17], [44], optical fiber [56], [57], [58] and microimage strain sensing (MISS) [59], [60] are some of the types of sensors used for strain measurement (see **Figure 1-5**). Piezoelectric [23], [61] and micromechanic (MEMS) [62] accelerometers are usually used for acceleration measurements (see **Figure 1-6**). The first are more suitable for vibration and high-frequency events measurements, and the second ones are more suitable for low-frequency measurements. Inertial motion units (IMU), which combine multiaxial acceleration and orientation sensors, are sometimes used, especially in floating structures [7].

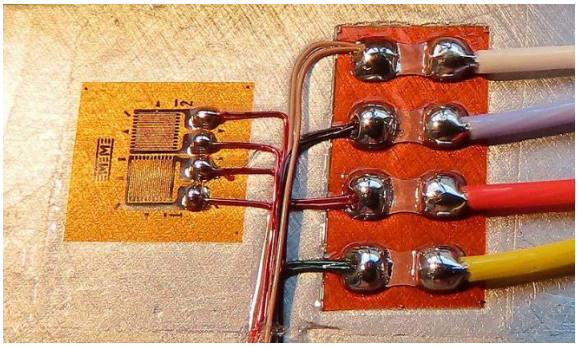

Figure 1-5 *Strain gauges installed in a metal component. Source: https://commons.wikimedia.org/*

Figure 1-6 *Triaxial accelerometer, manufactured by SparkFun. Source: https://commons.wikimedia.org/*

Other types of sensors are sometimes used. For example, in SHM systems, wind speed sensors (in the case of wind turbines and other tall structures) [63], [64], [65] or weight-in-motion sensors (in the case of bridges) are used [66], [67]. In CM systems, encoders, speed sensors, temperature sensors and oil debris sensors (in the case of engines and gearboxes) [48], [68] are often used. External loads are usually measured, being less the cases where VS systems are implemented without measuring the external loads.

1.2 Problem description

After reviewing a wide variety of VS applications in SHM and CM systems in recent years, the following considerations arise.

Virtual sensors are commonly used in SHM systems, being wind turbines one of the applications where the use of this technology is most widespread. In this field of application, it is common the use of strain sensors and accelerometers as input sensors. External loads are also usually estimated using the measured wind speed (which entails certain complexity and uncertainties). On the contrary, it has been observed a great disparity in the VS methods implemented in different applications, without an established consensus on which methods are the most appropriate for each necessity. Moreover, not enough information has been found on the quantity and location of input sensors that is needed to be installed in monitored systems, to obtain reliable VS estimations minimizing the costs.

In CM applied to industrial machines (such as presses and equivalent equipment), it has been observed that the use of virtual sensors is still uncommon. Moreover, very few applications of CM systems for strain measurement at critical points have been found in the bibliography. Generally, in this type of industrial equipment, CM systems are based on vibration analysis (using accelerometers as input sensors).

In certain cases, both in CM and SHM systems, the measurement of external loads can be difficult or even unfeasible, sometimes because the sensors necessary to measure the external loads are expensive and complex, and sometimes due to the uncertainties associated with external loads. A lack of consensus has been detected on which are the appropriate VS methods (along with which are the appropriate input sensors) when measurements of external loads are not available.

1.3 Purpose and objectives

The purpose of this thesis is to propose a methodology, and to adapt, test and evaluate different research on VS algorithms for strain/stress estimation at unmeasured points of structural systems, in order to help facilitate the implementation of strain/stress virtual sensors in different types of industrial systems, both to help reduce the number of sensors in monitoring systems (and thus reduce their cost) and to allow to estimate measurements at non-measurable points. For this thesis, the cases where external load measurements are not available are of special interest because to obtain direct measurement of loads is often expensive and require intrusive and complex measurement systems (such as force transducers). It is considered that, with what has been explained previously, a relevant contribution can be made within the field of CM and SHM systems.

This thesis has the following specific objectives:

• To propose some variations of existing VS algorithms, specifically oriented for strain/stress estimation under conditions of unmeasured external loads. There variants aim to simplify the implementation of virtual sensors in the specific conditions described.

• To test different VS algorithms (existing versions and proposed new versions) using two different scaled prototypes (offshore wind turbine prototype and industrial press bed prototype) with the aim of obtain strain estimations at unmeasured points. The objective is to study and compare the performance of the tested VS algorithms under conditions of unmeasured external loads and using different input sensor configurations, and to study the applicability of different VS algorithms in different industrial applications, which have different requirements and needs.

• To test different VS algorithms under static/quasistatic and dynamic loads, in order to study their performance under different load conditions that imply different types of excitations in the prototypes.

• To study if the strain estimations obtained with the tested VS algorithms can be used to estimate reliably the accumulated fatigue damage. For this purpose, one of the prototypes is subjected to a fatigue test, with the aim of validating experimentally the fatigue estimations obtained with the strain virtual sensors.

• To create a software library (in open-source code) which allows the VS algorithms described in this thesis to be applied flexibly in different structural systems.

1.4 Scope and limitations

In this subchapter, the main scopes and the limitations of the presented work are described.

In this thesis, different VS algorithms are tested to estimate strain at unmeasured points. As described in subsection 1.1, there are model-based and data-driven VS algorithms. This thesis is focused on model-based algorithms, therefore data-driven algorithms are not tested.

It is assumed that the scaled prototypes used in this thesis as use cases have a linear and time invariant behaviour. Thus, only linear models are used for implementing model-based VS methods. Algorithms designed to work with nonlinear systems (such as the EKF or the UKF) are not tested.

In this thesis, strain is the magnitude estimated by the tested VS algorithms. From the strain estimates and using the properties of the material, it is also possible to estimate the stress. Other magnitudes (such as accelerations or external loads) are not estimated in this thesis.

Regarding estimation of accumulated fatigue, in this thesis a classical fatigue approach is used, using SN curves (with the required factors and corrections) and cycle counting of strain/stress time series to estimate the accumulated damage. Alternative fatigue approaches (such as vibration fatigue) are not used. In the fatigue test performed, only the phase until crack initiation is studied. This thesis does not focus on the crack growth phase.

1.5 Outline

This thesis is organized as explained as follows. Section 1, titled *Introduction and theoretical content*, contents chapters 1, 2 and 3. Section 2, titled *Experiments performed*, contents chapters 4, 5 and 6.

Chapter 1 is titled *Introduction and objectives*. This chapter contains the main state of the art of this thesis and explains the problems and necessities found to which this thesis aims to provide solutions. The objectives to be achieved in this thesis (with their scopes and limitations) are described.

Chapter 2 is titled *Virtual sensing.* In this chapter, in first place the history and state of the art of the VS algorithms selected in this thesis is described, and the methodology used in this thesis for VS implementation is described. Theory related to systems modelling and model reduction is described. Each used VS algorithm is described in detail.

Chapter 3 is titled *Fatigue*. An introduction to the concept of material fatigue is made, and the use of SN curves and the calculation of accumulated damage is described. Crack propagation mechanics and probabilistic fatigue are explained. Fatigue applied to welded joints is also explained.

Chapter 4 and chapter 5 are titled *Study case 1* and *Study case 2*, respectively. The experiments carried out in both study cases are explained. The prototypes used are described, and the different phases for the implementation of virtual sensors in the prototype are also described. The obtained results in both experiments are presented and discussed.

Chapter 6 is titled *Conclusions.* In this chapter, the results obtained in the case studies carried out are analysed globally, and it is assessed whether the purposes and objectives set out in chapter 1 have been achieved. Possible future research lines are also commented.

1.6 Outcomes

In this subchapter, the developments generated in this thesis are listed, including methodologies, algorithms, research articles and software.

One of the developments of this thesis is a methodology for applying virtual sensors, described in subchapter 2.1.

Two VS algorithms for strain/stress estimation under unmeasured loads have been proposed in this thesis (based on existing VS algorithms): the Least Squares Strain Estimation (LSSE) and the Static Strain Kalman Filter (SSKF).

Three articles have been produced in the context of this thesis:

• Kalman-based virtual sensing for structural health monitoring, presented in the congress *DinEst 2021* in Gijón, Spain [69].

• Strain virtual sensing for Structural Health Monitoring under variable loads, published in *Sensors* in 2023 [70].

• Strain virtual sensing applied to industrial presses for fatigue monitoring, published in *Sensors* in 2024 [71].

Also, a software library derived from the developments of this thesis has been registered by Ikerlan: Python Virtual Structural Sensing Platform. This consists of a Python library which allows to easily apply VS algorithms, plus some extra features.

Chapter 2
VIRTUAL SENSING

This chapter is structured in fourteen subchapters. In *2.1*, the background of the model-based VS methods used in this thesis is explained. In *2.2*, the methodology used in this thesis for implementing virtual sensors is commented. In *2.3*, finite element modelling is introduced. In *2.4*, state-space modelling is explained. In *2.5*, the modal base transformation is explained. In *2.6*, the concept of model reduction is introduced, and various model reduction methods are explained. In *2.7*, the characteristics of strain/stress measurement are explained. From *2.8* to *2.12*, the different VS algorithms used in this thesis are explained, and in *2.13*, the evaluation methods used are explained.

2.1 History and background of model-based VS methods.

In subchapter 1.1, the concept of VS has been defined. A classification of the existing VS methods has been made, mainly differentiating between data-driven and model-based methods; and within the model-based methods, between stochastic and deterministic methods. Moreover, examples of VS application in the research literature and in industry have been shown, also identifying areas of application yet to be exploited. In this subchapter, the definition and evolution of the VS algorithms selected in this thesis (which can be seen later in **Table 2-1**) are described.

It is difficult to trace the history of direct model application in structural systems. One of the first precedents could be the Hooke's law, proposed by R. Hooke in the 17th century, later generalized in the theory of elasticity, that states that in a linear solid material, the strain is proportional to the stress applied (in turn linearly related to the applied loads) under static or quasistatic loads. Some works that use the linear relation between loads and strains for estimation of unknown variables can be found in the bibliography [72]. With the matrices obtained from a structural FEM model (in its full dimension or simplified using model reduction methods) it is possible to obtain a model capable of reproducing both the quasistatic and dynamic responses of a structural system.

In 1960, Rudolf Kalman presented the today known as Kalman filter (KF) [73], a Bayesian algorithm for state estimation that uses a state-space model of a system and a limited number of measurement data. Due to this algorithm allows to associate certain uncertainty values to the model and the input data, the KF is a stochastic model-based algorithm. Bucy and Schmidt also participated in the initial development of this algorithm, that is why the KF is sometimes also known as Kalman-Bucy filter or Schmidt-Kalman filter [74], [75]. Less capable algorithms had been proposed in the past, such as the Wiener filter proposed in the 1940s, which did not integrate a model with states [76].

The KF was early adopted in the 1960s by the NASA and the US Air Force for aircraft and spacecraft guidance purposes, becoming very popular to this day [77]. Starting in the 2000s, the KF has begun to be also applied for the estimation of unmeasured parameters in structures, which has led to the application of virtual sensors in the context of CM and SHM systems.

The KF in its original conception has several limitations, which have been solved in different improvements. One limitation is that the original KF needs a linear model, so to work with non-linear systems different variants of the algorithm were proposed. The Extended Kalman filter (EKF) is an early variant of the KF for non-linear systems that performs a linearization of the estimated mean and covariance for each time step [36]. The Unscented Kalman filter (UKF) is a later for non-linear systems that avoids linearization by applying an unscented transformation [37].

Another limitation is that the original KF needs information about the external inputs on the system, which is not always possible to measure. A solution to this problem is the combination of the KF with an augmented state-space model, which consists of extending a state-space model so that external inputs are also considered states. The Augmented Kalman filter (AKF) is the result of combining an augmented state-space model with a KF, being able to estimate both the states and external inputs of the system, or simply estimate the states with the external loads being unknown [34],

[78]. The first proposal of using KF in combination with an augmented state-space model was done by B. Friedland in 1969 [32]. In 2011, the AKF was implemented for the estimation of inputs and states in structures [34], and in 2012, a variant called Joint Input-Response Estimation (JIRE) was proposed [79].

When a KF or one of its variants is implemented in a structural system, a state-space model that contains both dynamic and static components is generally used (see subchapter *2.4*). In some cases, only the static component is required (because only static or quasi-static loads are expected), and the use of a model with both components represents excess complexity that can also lead to a lack of accuracy. To deal with these cases, is proposed in this thesis a simplification of the KF for strain estimation in systems subjected to only static and quasistatic loads and under conditions of unmeasured external loads, named Static Strain Kalman Filter (SSKF).

As an alternative to Kalman filters and their variants (that are stochastic model-based VS algorithms), there are deterministic model-based VS methods. The simplest VS deterministic algorithm consists of the use of a model in an open-loop simulation, which requires measuring the external loads on the system. Other deterministic VS methods are the based on least-squares optimization (LS). LS is a mathematic method used to find a best-fit solution in overdetermined systems, by minimizing the sum of the squares of the errors (the differences between the measured values and the values provided by a model). The LS was first proposed in parallel by the French mathematician A.M. Legendre and by the C.F. Gauss in early 19th century [80]. Since then, it has been applied to solve a huge variety of problems. In the 20th century, an important progress was made with the introduction of the pseudoinverse method, presented in parallel by E.H. Moore in 1920 and by R. Penrose in 1955, and known because this as the Moore-Penrose pseudoinverse [81]. This method allows to approximate numerically the inverse of both squared and non-squared matrices and can be used to compute least squares solutions for underdetermined, determined, and overdetermined equation systems. In the 1960s, the Modal Expansion Method (MEM) was established [82], that consists of applying the modal transformation to a

system (that means to describe the system using its mode shapes) in order to simplify the calculation of its response. In recent years, the MEM has been applied to obtain estimations of unmeasured parameters in structural systems [39], [83], [84].

Combining the pseudoinverse-based least squares estimation with the Modal Expansion, the Least Squares Strain Estimation (LSSE) is proposed in this thesis, that consists of deterministic VS method for strain estimation using only strain measurements as input data.

A classification of the VS algorithms used in this thesis can be seen in **Figure 2-1**. The reasons why these algorithms have been selected in this thesis are explained below.

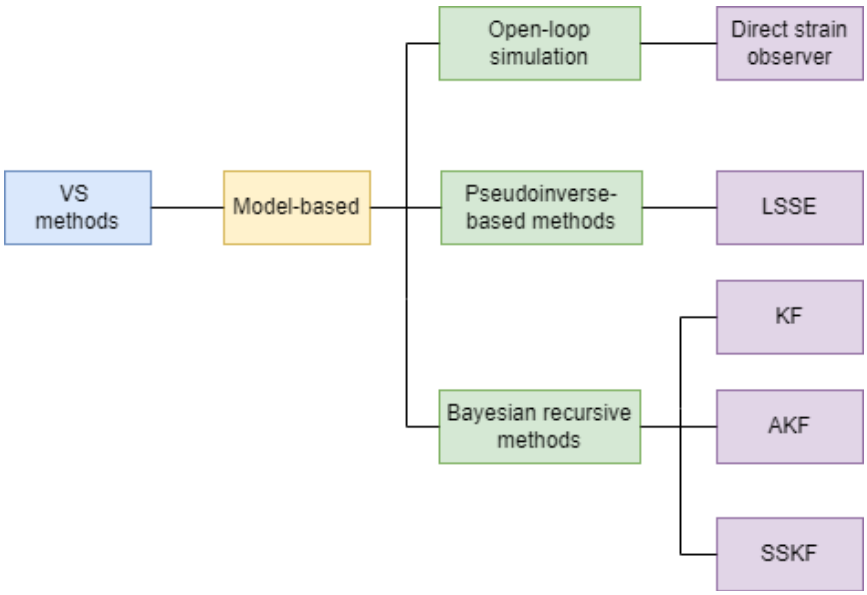

Figure 2-1 *Classification of VS algorithms used in this thesis.*

The open-loop simulation is used only in the second use case, because in that use case load measurement is available. This method is only used as a reference, to allow comparison with other more elaborate VS methods, because the interest in this thesis is to work with VS methods that do not require available load measurements.

The LSSE is proposed in this thesis as a representative deterministic model-based VS algorithm. This method can be implemented in both use cases and uses only strain measurements as inputs, being not necessary to measure the external loads. No other deterministic model-based VS algorithms suitable for the use cases of this thesis have been found in the bibliography.

In the case of stochastic model-based VS algorithms, different variants of the Kalman filter have been implemented. The classical KF has been selected as VS method in the first use case with the aim of testing its performance when external load measurements are not available (although in its conventional implementation, input measurements are required). The AKF, an alternative to classical KF designed to work without external load measurement, has been selected for the first use case to check if it is an upgrade compared to the KF (under conditions of non-measured loads). For the second use case, the SSKF has been proposed in this thesis as a special simplified variant only for cases under static/quasi-static loads. Other variants of the Kalman filter have been discarded for the purposes of this thesis. The Dual Kalman filter (DKF, an alternative to the AKF) has been also tested, but has been discarded in the early stages of this thesis due to its poor performance. Specific KF variants for non-linear systems (such as the EKF or the UKF) have not been selected since non-linearities are not considered in the use cases of this thesis. Particle Filters have been discarded due to their large computing capacity they require (PFs perform multiple Monte-Carlo simulations for each time step), making their use unfeasible due to the amounts of experimental data and fast sampling frequencies in both use cases.

In both use cases of this thesis, there is sufficient knowledge of the monitored systems to build detailed models of them. Because of this, data-driven VS methods are not

considered within the scope of this thesis, because they require a certain amount of training data to be implemented.

In **Table 2-1**, the main features of the selected VS methods are collected.

VS method	**Uncertainty management**	**Model used by the algorithm**	**Load measurement**	**Possible input sensor data**	**Sensing requirements**
Open-loop methods					
Direct observer	Deterministic	Static model Dynamic model	Required	External loads	-
LSSE	Deterministic	Strain matrix	Not required	Strain	Well-condition matrix
Closed-loop methods					
KF	Stochastic	State-space model	Optional	strain, displacement, velocity, acceleration, load	Observable
AKF	Stochastic	Augmented state-space model	Not required	strain, displacement, velocity, acceleration	Observable
SSKF	Stochastic	Static model	Not required	Strain	Observable

Table 2-1 *Summary of the selected VS algorithms in this thesis.*

2.2 Methodology for implementing virtual sensors in structural systems

In this thesis, the following methodology is proposed for implementing virtual sensors in different industrial applications (see **Figure 2-2**) [70], [71].

The starting point is the real system where virtual sensors are intended to be implemented. In the case of this thesis, we work with different structural facilities (see the use cases described in chapters 4 and 5). In first place, a finite element method (FEM) model of the system to be monitored is created (usually from a CAD model). The FEM model can be used to identify the critical points of the system, and also to choose the proper placement for the real sensors. Details about FEM modelling are explained in the subchapter 2.3. Once the FEM model is created, real sensors are placed in the system, and a data acquisition system necessary is set up to obtain real measurements. Real measurement data is used to verify if the behaviour of the generated FEM model resembles with enough precision the behaviour of the real system (or if, on the contrary, adjustments in the model are required).

From the verified FEM model, a reduced model is extracted from it. In subchapter 2.4, state-space modelling is explained, and in subchapter 2.6, the process of model reduction and different model reduction methods are explained. Once the data acquisition system is set up and a reduced model is available, a VS algorithm can be implemented. Different VS methods are described in subchapters 2.8 to 2.12.

To validate the virtual sensors implemented in the system and verify the proper functioning of the implemented VS algorithms, generally some virtual measurements are compared with equivalent real sensor data. In subchapter 2.13, some evaluation indicators are described.

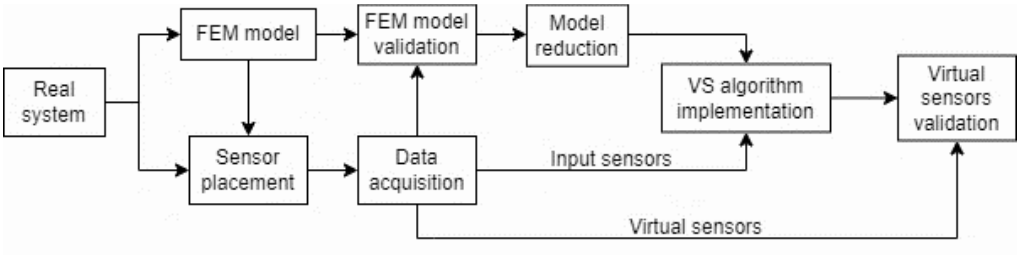

Figure 2-2 *Flowchart of the proposed methodology to implement virtual sensors.*

The Finite Element Methods (FEM) are numerical techniques used to obtain approximate solutions in a wide range of engineering and scientific problems, by discretizing a complex system into a large quantity of smaller parts, the so-called finite elements (see **Figure 2-3**). The interrelations between elements can be described by partial differential equations. Solving the resulting system that encompasses all the partial differential equations, a numerical solution of the problem can be found [85]. Some examples of problems usually solved with FEM are fluid mechanics, structural mechanics, heat transmission or impact simulations. In this thesis, structural FEM models are used.

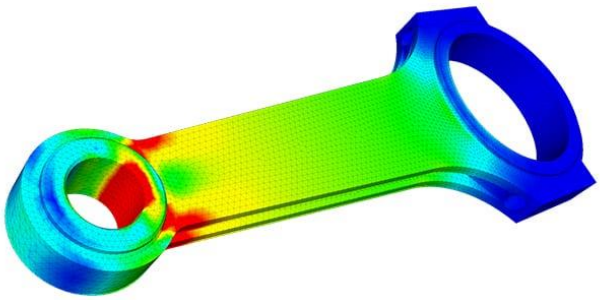

Figure 2-3 *Example of a FEM model of an engine rod. Source: https://www.simscale.com*

The FEM was first proposed in 1941 in Canada by A. Hrennikoff, who used the discretization into small elements to solve a problem of the elasticity of a plate [86]. During the 1950s, FEM began to evolve mainly with the involvement of aeronautical companies, but always limited by the scarce computing capacity of those years. In the 1960s, the first software programs for the application of FEM to various industrial problems began to emerge. Since then, the FEM has spread to most areas of the industry, with the help of the emergence of well-established commercial software,

such as NASTRAN or ANSYS (see **Figure 2-4**). The capabilities of the FEM have always been evolving hand in hand with the capacity of available computers [86].

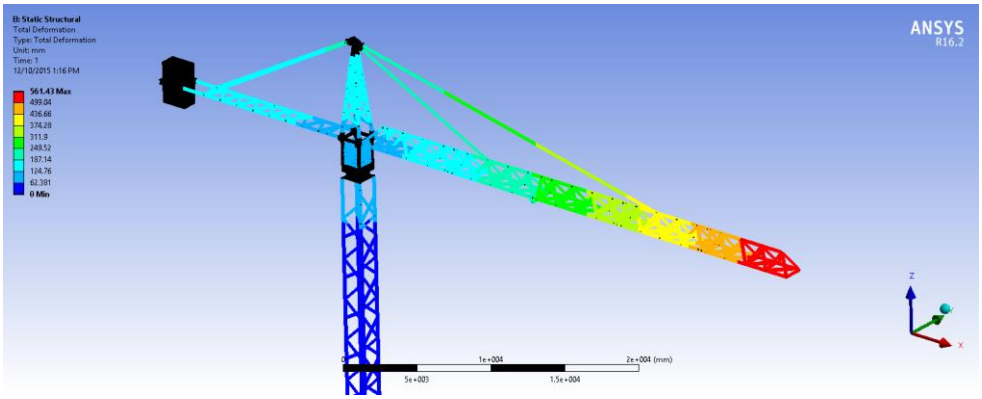

Figure 2-4 *Example of a FEM model of a complex structure in an ANSYS studio. Source: https://www.finiteelementanalysis.com.au/*

To solve a problem of structural mechanics using FEM, generally the following steps are followed:

First, a model of the structure or component to analyse is created. Usually, Computer-Aided Design (CAD) models are used. Depending on the case study, 2D or 3D models can be created, with a level of detail also adjusted to the needs of the problem. Next, the model is discretized into smaller elements, a process known as meshing. This process is usually automated by the FEM software used. However, the user must specify the characteristics of the mesh, such as minimum or maximum element size, type of elements, and number of nodes per element. Once the model is meshed, the appropriate boundary conditions must be set up by the user. These include the connections of the model with the environment, the external loads, or the interconnections between parts of the model (in case there are more than one). Finally, the FEM software creates the matrices that define the problem and assembles the corresponding matrix equations. After solving the equations numerically, a solution is offered.

When FEM are applied to a solid mechanics problem, a mass-spring-damper equation of the model is obtained. In this thesis, this equation is referred as the MCK equation, and it consists of a second-order differential matrix equation (equation 2-1).

A FEM model contains *s* number of nodes, and each node can have up to 6 degrees of freedom (DoFs): q_x, q_y, q_z displacements in x, y and z axes; and θ_x, θ_y, θ_z rotations with respect to x, y and z axes, respectively. *n* is the total number of DoFs of the model.

To build the MCK equation of a FEM model, first a displacement vector (**q**) is defined, containing the displacements (linear and angular) of each DoF of the model, with *n×1* dimension. The first and second derivatives of the displacement vector ($\dot{\mathbf{q}}$ and $\ddot{\mathbf{q}}$) correspond to the vectors of velocities and accelerations, respectively. **M**, $\mathbf{C_D}$ and **K** are the stiffness, damping and mass matrices of the model, respectively (the three of *n×n* dimension). **f** is the vector of loads, that contains the external loads applied to each DoF of the model (see figure **Figure 2-5**).

$$\mathbf{M}\ddot{\mathbf{q}}(t) + \mathbf{C_D}\dot{\mathbf{q}}(t) + \mathbf{K}\mathbf{q}(t) = \mathbf{f}(t) \qquad 2\text{-}1$$

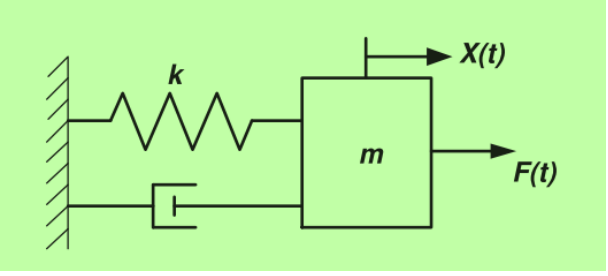

Figure 2-5 *Simple visual representation of a mass-spring-damper model* [87]

The stiffness matrix **K** is a symmetric and square matrix that describes the resistance to deformation of the model, defining the stiffness of each element of the model and of each connection between elements.

The damping matrix $\mathbf{C_D}$ is a square matrix (not necessarily symmetrical) that describes the capacity of the model of dissipating energy over time.

The mass matrix **M** is a symmetric and square matrix that describes how the total mass is distributed among the elements of the model. **M** is related to the internal kinetic energy of the model (**T**), as seen in equation 2-2.

$$\mathbf{T} = \frac{1}{2}\dot{\mathbf{q}}^{\mathbf{T}}(t)\mathbf{M}\dot{\mathbf{q}}(t) \qquad 2\text{-}2$$

A state-space model is a matrix representation of a system in terms of state variables, which are a set of internal variables that fully describe the state of the system at any instant of time (see **Figure 2-6**). The state-space representation of a MCK model is a time-domain approach that redescribes the system in terms of inputs, outputs, and states, and simplifies its resolution by avoiding the second-order differential equations (using instead first-order differential equations).

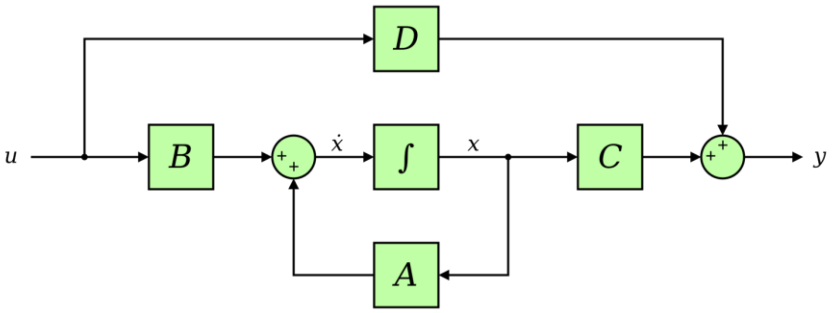

Figure 2-6 *Block diagram representation of a state-space model. Source: https://commons.wikimedia.org/*

In the case of a structural MCK model, the states of the model are the displacements and the velocities of each DoF. The state-space representation is shown in equation 2-3. **x**(t) is the states vector of the model, with *2n×1* dimension (see equation 2-4), and $\dot{\mathbf{x}}$(t) is the first derivative of the states vector (that contains the velocities and the accelerations of each DoF), also with *2n×1* dimension (see equation 2-5). **u**(t) is the

external inputs vector, that contains the external loads applied to each DoF, with *n×1* dimension (see equation 2-6).

$$\begin{cases}\dot{\mathbf{x}}(t) = \mathbf{A}\mathbf{x}(t) + \mathbf{B}\mathbf{u}(t) \\ \mathbf{y}(t) = \mathbf{C}\mathbf{x}(t) + \mathbf{D}\mathbf{u}(t)\end{cases} \quad 2\text{-}3$$

$$\mathbf{x}(t) = \begin{pmatrix}\mathbf{q}(t) \\ \dot{\mathbf{q}}(t)\end{pmatrix} \quad 2\text{-}4$$

$$\dot{\mathbf{x}}(t) = \begin{pmatrix}\dot{\mathbf{q}}(t) \\ \ddot{\mathbf{q}}(t)\end{pmatrix} \quad 2\text{-}5$$

$$\mathbf{u}(t) = (\mathbf{f}(t)) \quad 2\text{-}6$$

A is the state matrix, that relates the state variables with their derivatives with a size of *2n*×2*n*. Its construction is shown in equation 2-7. **B** is the input matrix, that relates the external loads with the state derivatives, with a size of *2n*×*n*. Its construction is shown in equation 2-8.

$$\mathbf{A} = \begin{bmatrix}\mathbf{0} & \mathbf{I} \\ -\mathbf{M}^{-1}\mathbf{K} & -\mathbf{M}^{-1}\mathbf{C_D}\end{bmatrix} \quad 2\text{-}7$$

$$\mathbf{B} = \begin{bmatrix}\mathbf{0} \\ \mathbf{M}^{-1}\end{bmatrix} \quad 2\text{-}8$$

y(t) is the outputs vector of the system, and its content is defined by the user. **C** and **D** are the output and feedthrough matrices respectively, that relate the state variables and external loads with the defined outputs. If the defined outputs consists of displacements, velocities, accelerations of each DoF and external loads, the outputs vector has *4n×1* dimension (see equation 2-9), and the **C** and **D** matrices have *4n×2n* (see equation 2-10) and *4n×n* (see equation 2-11) dimension respectively.

$$\boldsymbol{y}(t) = \begin{pmatrix}\mathbf{q}(t) \\ \dot{\mathbf{q}}(t) \\ \ddot{\mathbf{q}}(t) \\ \mathbf{f}(t)\end{pmatrix} \quad 2\text{-}9$$

$$\mathbf{C} = \begin{bmatrix}\mathbf{I} & \mathbf{0} \\ \mathbf{0} & \mathbf{I} \\ -\mathbf{M}^{-1}\mathbf{K} & -\mathbf{M}^{-1}\mathbf{C_D} \\ \mathbf{0} & \mathbf{0}\end{bmatrix} \quad 2\text{-}10$$

$$\mathbf{D} = \begin{bmatrix} \mathbf{0} \\ \mathbf{0} \\ \mathbf{M^{-1}} \\ \mathbf{I} \end{bmatrix} \quad \text{2-11}$$

A state-space model is usually used in a discrete-time approach, in which a time step Δt is defined and the model is solved iteratively for each time increment. To be used in a discrete-time approach, a state-space model must be discretized. $\mathbf{A_d}$ (see equation 2-12) and $\mathbf{B_d}$ (see equation 2-13) are the discretized versions of the **A** and **B** state-space matrices, respectively. Matrices **C** and **D** do not suffer alterations after their discretization (see equations 2-14 and 2-15). The discretized representation of the state-space system (seen in equation 2-3) can bee seen in equation 2-16.

$$\mathbf{A_d} = e^{\mathbf{A}\Delta t} \quad \text{2-12}$$

$$\mathbf{B_d} = \left(\int_{t=0}^{T} e^{\mathbf{A}t} dt\right)\mathbf{B} = \mathbf{A^{-1}}(\mathbf{A_d} - \mathbf{I})\mathbf{B} \quad \text{2-13}$$

$$\mathbf{C_d} = \mathbf{C} \quad \text{2-14}$$

$$\mathbf{D_d} = \mathbf{D} \quad \text{2-15}$$

$$\begin{cases} \mathbf{x_{t+1}} = \mathbf{A_D x_t} + \mathbf{B_D u_t} \\ \mathbf{y_t} = \mathbf{C_D x_t} + \mathbf{D_D u_t} \end{cases} \quad \text{2-16}$$

The MCK equation of a model can be also described using its mode shapes (see **Figure 2-7**). For this purpose, the modal matrix (**Φ**) is used. Each column of **Φ** is an eigenvector ($\boldsymbol{\varphi_n}$), which corresponds to a specific mode shape of the model. Each eigenvector contains the normalized displacements of all DoF of the model for its corresponding mode shape. The eigenvectors are also associated to the eigenvalues (λ_n), which correspond to the square roots of the natural frequencies of the modes of the model (ω_n). All the eigenvalues are contained in the eigenvalues vector **λ**, with *n×1* dimension. The size of **Φ** in its full form is *n×n*, containing as many modal shapes as DoFs has the model. The eigenvalues of an undamped system are generally real values, but in the case of damped systems, complex eigenvalues (with real and imaginary parts) appear [88].

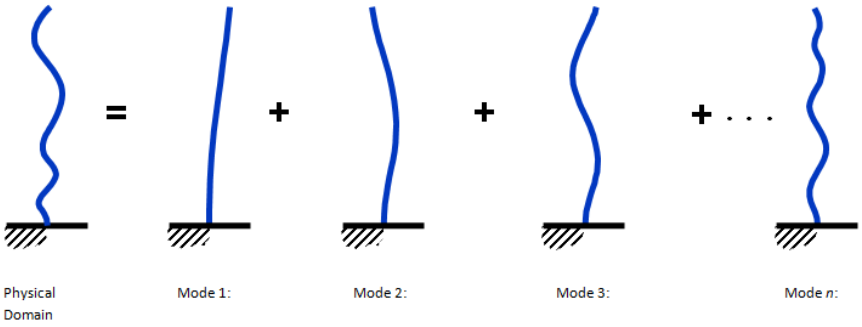

Figure 2-7 *The state of deformation of a system can be represented by a linear combination of its mode shapes. This technique is known as modal decomposition. Source: https://www.svibs.com (ARTeMIS Modal)*

Φ can be obtained solving the undamped equation 2-17, discarding the trivial solution **Φ=0**. **Φ** can be unit-normalized or mass-normalized. In the case of unit-normalization, all the displacements of the DoFs are multiplied by a factor so that the maximum value is 1, for each mode shape. In the case of mass-normalization, each mode shape is multiplied by a factor so that the expression 2-18 is satisfied.

$$(\mathbf{K} - \boldsymbol{\lambda}\mathbf{M})\boldsymbol{\Phi} = (\mathbf{K} - \boldsymbol{\omega}^2\mathbf{M})\boldsymbol{\Phi} = \mathbf{0} \quad \text{2-17}$$

$$\boldsymbol{\Phi}^{\mathbf{T}}\mathbf{M}\boldsymbol{\Phi} = \mathbf{I} \quad \text{2-18}$$

The equation 2-1 can be transformed to its modal equivalent using $\boldsymbol{\Phi}$ (see equation 2-19). $\mathbf{z}(t)$ is the vector of modal displacements (also known as generalized displacements), obtained with the transformation $\mathbf{q}(t) = \boldsymbol{\Phi}\,\mathbf{z}(t)$ [89].

$$\boldsymbol{\Phi}^{\mathbf{T}}\mathbf{M}\boldsymbol{\Phi}\ddot{\mathbf{z}}(t) + \boldsymbol{\Phi}^{\mathbf{T}}\mathbf{C}_{\mathbf{D}}\boldsymbol{\Phi}\dot{\mathbf{z}}(t) + \boldsymbol{\Phi}^{\mathbf{T}}\mathbf{K}\boldsymbol{\Phi}\mathbf{z}(t) = \boldsymbol{\Phi}^{\mathbf{T}}\mathbf{f}(t) \quad \text{2-19}$$

A model reduction method is a procedure that allows to reduce the number of DoFs of a structural model but maintaining a sufficient degree of precision in its behaviour in a limited range of use. Reduced models are generally extracted from FEM models that represent complex structures (generally made of thousands or even millions of DoFs), to obtain models with a much smaller number of DoFs, which require much shorter computing times to be solved (see **Figure 2-8**).

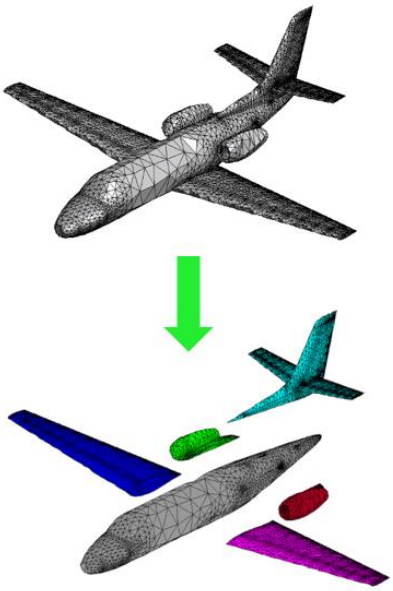

Figure 2-8 *Schematic representation of the application of a reduction method on the FEM model of an airplane* [90]. *In the picture above, a complete FEM model of an airplane can be seen. In the picture below, the reduced model condensed into several components (remarked in colours) can be seen.*

Model reduction methods can be generalized to the obtention of a transformation matrix $\mathbf{T}_{\mathbf{red}}$ and the subsequent application of it to the mass (equation 2-20), damping (equation 2-21) and stiffness (equation 2-22) matrices of the MCK model.

$$\mathbf{T_{red}}^{\mathbf{T}}\mathbf{M}\mathbf{T_{red}} = \mathbf{M_{red}} \quad 2\text{-}20$$

$$\mathbf{T_{red}}^{\mathbf{T}}\mathbf{C_D}\mathbf{T_{red}} = \mathbf{C_{D\,red}} \quad 2\text{-}21$$

$$\mathbf{T_{red}}^{\mathbf{T}}\mathbf{K}\mathbf{T_{red}} = \mathbf{K_{red}} \quad 2\text{-}22$$

Different reduction methods can be found in the bibliography. One of the first developed reduction methods was the Guyan static condensation method (GR), presented by R. Guyan in 1965 [91]. In this method, a set of nodes is selected (called master nodes, which will be the nodes of the reduced model. The behaviour of the complete model is condensed in these nodes. The rest of nodes of the model remain as slave nodes. If a FEM model has *m* total nodes and *p* master nodes are selected, the number of slave nodes (the rest of nodes) is *m*-*p*=*s*. $\mathbf{M_{p\times p}}$ and $\mathbf{K_{p\times p}}$ are the reduced matrices, $\mathbf{q}_p$ is the displacement vector corresponding to the master nodes, $\mathbf{M_{s\times s}}$ and $\mathbf{K_{s\times s}}$ are the matrices corresponding to the slave nodes, $\mathbf{q_s}$ is the displacement vector of the slave nodes, and $\mathbf{f_p}$ the equivalent external loads applied to the master nodes. $\mathbf{M_{ps}}$ and $\mathbf{K_{ps}}$ (and their transposed versions $\mathbf{M_{sp}}$ and $\mathbf{K_{sp}}$) relates the master nodes with the slave nodes (see equation 2-23).

$$\begin{bmatrix}\mathbf{M_{pp}} & \mathbf{M_{ps}}\\ \mathbf{M_{sp}} & \mathbf{M_{ss}}\end{bmatrix}\begin{pmatrix}\ddot{\mathbf{q}}_p\\ \ddot{\mathbf{q}}_s\end{pmatrix} + \begin{bmatrix}\mathbf{K_{pp}} & \mathbf{K_{ps}}\\ \mathbf{K_{sp}} & \mathbf{K_{ss}}\end{bmatrix}\begin{pmatrix}\mathbf{q_p}\\ \mathbf{q_s}\end{pmatrix} = \begin{pmatrix}\mathbf{f_p}\\ \mathbf{0}\end{pmatrix} \quad 2\text{-}23$$

The GR transformation matrix ($\mathbf{T_{GR}}$) is obtained as seen in equation 2-24. $\mathbf{T_{GR}}$ allows to obtain the Guyan's reduced mass (see equation 2-25) and stiffness matrices (see equation 2-26).

$$\begin{pmatrix}\mathbf{q_p}\\ \mathbf{q_s}\end{pmatrix} = \begin{bmatrix}\mathbf{I_{pp}}\\ -\mathbf{K_{ss}}^{-1}\mathbf{K_{sp}}\end{bmatrix}(\mathbf{q_p}) = \mathbf{T_{GR}}(\mathbf{q_p}) \quad 2\text{-}24$$

$$\mathbf{T_{GR}}^{\mathbf{T}}\mathbf{K}\mathbf{T_{GR}} = \mathbf{K_{GR}} \quad 2\text{-}25$$

$$\mathbf{T_{GR}}^{\mathbf{T}}\mathbf{M}\mathbf{T_{GR}} = \mathbf{M_{GR}} \quad 2\text{-}26$$

Different improvements of the GR have been proposed in the bibliography, known as Improved Reduction Systems [92]. The standard IRS was presented by J. O'Callahan in 1989. It consists of a reduction method that improves the GR adding inertia terms. The transformation matrix ($\mathbf{T_{IRS}}$) is obtained as seen in equation 2-27.

$$\mathbf{T_{IRS}} = \mathbf{T_{GR}} + \begin{bmatrix} \mathbf{0} & \mathbf{0} \\ \mathbf{0} & \mathbf{K_{ss}}^{-1} \end{bmatrix} \mathbf{M T_{GR}} \mathbf{M_{GR}}^{-1} \mathbf{K_{GR}} \qquad 2\text{-}27$$

The Craig-Bampton reduction method (CB) was presented by R. Craig and M. Bampton in 1968 [93]. It is a component mode synthesis method that combines the static reduction of the GR with a limited number of internal modes (corresponding to the slave nodes of the structure, remaining the selected master nodes as fixed) (see equation 2-28). These internal modes can provide extra information to the reduced model, compared to a Guyan reduced model. The matrix of internal modal shapes (eigenvectors) $\mathbf{\Phi_{CB}}$, is obtained by applying the eigenvectors equation to the slave nodes matrices, discarding the trivial solution. A CB reduced model has *m* master nodes (with their corresponding displacements $\mathbf{q_m}$) and *n* internal modes (with their corresponding modal displacements $\mathbf{z_{CB}}$). The CB transformation matrix ($\mathbf{T_{CB}}$) is obtained as seen in equation 2-29.

$$(\mathbf{K_{ss}} - \boldsymbol{\omega}^2{}_{\mathbf{ss}} \mathbf{M_{ss}}) \mathbf{\Phi_{CB}} = \mathbf{0} \qquad 2\text{-}28$$

$$\begin{pmatrix} \mathbf{q_p} \\ \mathbf{q_s} \end{pmatrix} = \begin{bmatrix} \mathbf{I} & 0 \\ -\mathbf{K_{ss}}^{-1} \mathbf{K_{sp}} & \mathbf{\Phi_{CB}} \end{bmatrix} \begin{pmatrix} \mathbf{q_m} \\ \mathbf{z_{CB}} \end{pmatrix} = \mathbf{T_{CB}} \begin{pmatrix} \mathbf{q_m} \\ \mathbf{z_{CB}} \end{pmatrix} \qquad 2\text{-}29$$

The modal truncation is a model reduction that consists of first describe a model using modal decomposition (as seen in equation 2-19) and then select only a limited number of them, discarding the rest [94]. The modal truncation uses the Φ-transformation (see equation 2-17) but removing from $\mathbf{\Phi}$ all those modes whose frequencies are out of the range of frequencies of interest. For a *k* number of modes kept, $\mathbf{\Phi}$ is reduced to $\mathbf{\Phi_K}$, with its dimension reduced to $n \times k$ (see equation 2-30).

$$\boldsymbol{\Phi_K} = [\boldsymbol{\varphi_1}, \boldsymbol{\varphi_2} \dots \boldsymbol{\varphi_k}] \qquad 2\text{-}30$$

Applying the transformation matrix $\boldsymbol{\Phi_K}$ to a MCK model, a modal-truncated model is obtained. If $\boldsymbol{\Phi_K}$ is mass-normalized (as seen in equation 2-18), the modal-truncated MCK equation can be also described using the equation 2-31. $\boldsymbol{\Phi_K}^T\mathbf{M}\boldsymbol{\Phi_K}$ corresponds to an identity matrix $\mathbf{I}$. $\boldsymbol{\Phi_K}^T\mathbf{C_D}\boldsymbol{\Phi_K}$ corresponds to a diagonal matrix $\boldsymbol{\Sigma}$ that contains the damping ratios (ξ) associated with each mode. $\boldsymbol{\Phi_K}^T\mathbf{K}\boldsymbol{\Phi_K}$ corresponds to a diagonal matrix Ω that contains the natural frequencies of the model (ω).

$$\ddot{\mathbf{z}}(t) + 2\boldsymbol{\Sigma\Omega}\dot{\mathbf{z}}(t) + \boldsymbol{\Omega}^2\mathbf{z}(t) = \boldsymbol{\Phi_k}^T\mathbf{f}(t) \qquad 2\text{-}31$$

The main criteria to apply the modal truncation are to keep the modes whose frequencies are expected to be excited in the operational conditions of the system, and to kept modes should contain an effective modal mass of at least the 90% of the real mass of the structure [95].

The System Equivalent Reduction-Expansion Process (SEREP) is an improvement of the modal truncation method, presented by J. O'Callahan and P. Avitabile in 1989 [96]. The vector of modal displacements ($\mathbf{z}$) is divided into retained ($\mathbf{z_r}$) and discarded ($\mathbf{z_d}$) (see equation 2-32). $\boldsymbol{\Phi_{rr}}$ is the modal matrix with the retained modes and $\boldsymbol{\Phi_{dd}}$ with the discarded modes. The SEREP transformation matrix ($\mathbf{T_{SEREP}}$) is obtained as follows. Unlike in the modal truncation, the SEREP retains information of the discarded modes in the reduction process (equation 2-33).

$$\mathbf{q} = \boldsymbol{\Phi_Z} = \begin{bmatrix} \boldsymbol{\Phi_{rr}} & \boldsymbol{\Phi_{rd}} \\ \boldsymbol{\Phi_{dr}} & \boldsymbol{\Phi_{dd}} \end{bmatrix} \begin{pmatrix} \mathbf{z_r} \\ \mathbf{z_d} \end{pmatrix} \qquad 2\text{-}32$$

$$\mathbf{T_{SEREP}} = \begin{pmatrix} \boldsymbol{\Phi}_{rr} \\ \boldsymbol{\Phi}_{dr} \end{pmatrix} \boldsymbol{\Phi}_{rr}{}^{-1} = \begin{pmatrix} \mathbf{I} \\ \boldsymbol{\Phi}_{dr}\boldsymbol{\Phi}_{rr}{}^{-1} \end{pmatrix} \qquad 2\text{-}33$$

The DoF of a FEM model, or of a reduced model extracted from it, are the displacements and rotations of the nodes. Hence, these are the results obtained after solving a model in a static calculation. In the case of a dynamic transient calculation, the displacements/rotations and their derivatives (velocities and accelerations) of the nodes over time are obtained after solving a model.

In many cases, the desired results include other quantities, such as the different strain or stress components of the model. In this thesis, strain is the main magnitude of interest to be estimated by the VS algorithms.

Strain is a relative and dimensionless magnitude that relates the deformation experimented by a material with its original shape. Normal strains (ε) are defined as the partial derivatives of the displacements (see equation 2-34), and shear strains (γ) are defined as the partial derivatives of the rotations (see equation 2-35).

$$\varepsilon_x;\ \varepsilon_y;\ \varepsilon_z = \frac{\partial q_x}{\partial x}\ ;\ \frac{\partial q_y}{\partial y}\ ;\ \frac{\partial q_z}{\partial z} \qquad 2\text{-}34$$

$$\gamma_{xy};\ \gamma_{yz};\ \gamma_{xz} = \frac{\partial q_x}{\partial y} + \frac{\partial q_y}{\partial x}\ ;\ \frac{\partial q_y}{\partial z} + \frac{\partial q_z}{\partial y}\ ;\ \frac{\partial q_x}{\partial z} + \frac{\partial q_z}{\partial x} \qquad 2\text{-}35$$

Knowing the properties of the material (the Young modulus (E), the shear modulus (G_{sh}) and the Poisson ratio (ν)) and assuming that it is an isotropic material (their properties are the same in all directions), the stress components can be obtained from the strain components. In the case of a single component of strain, the stress is directly related with the equation 2-36. In the case of the strain in a plane (with three components), the stress components can be obtained using equation 2-37. For obtaining all six components of the Cauchy's stress tensor (see **Figure 2-9**), the generalized form of the Hooke's law can be used [97]. The six components of the Cauchy's stress consist of three normal stresses (σ) and three shear stresses (τ).

$$\sigma_x = \frac{E}{1-\nu^2}\varepsilon_x \qquad 2\text{-}36$$

$$\begin{pmatrix}\sigma_x\\ \sigma_y\\ \tau_{xy}\end{pmatrix} = \begin{bmatrix}\frac{E}{1-\nu^2} & \frac{\nu E}{1-\nu^2} & 0\\ \frac{\nu E}{1-\nu^2} & \frac{E}{1-\nu^2} & 0\\ 0 & 0 & G_{sh}\end{bmatrix}\begin{pmatrix}\varepsilon_x\\ \varepsilon_y\\ \gamma_{xy}\end{pmatrix} \qquad 2\text{-}37$$

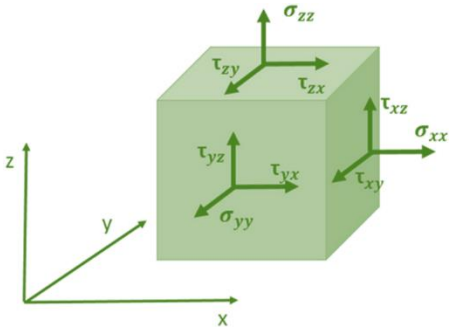

Figure 2-9 *Cauchy's stress tensor* [98]

In this thesis, a method is proposed to obtain estimations of strain measurements at a limited number of points of a system, using a reduced model. This method consists of a model expansion process but limited to a specified set of measurements. A strain matrix **G** is defined from the FEM model. This matrix relates the displacements of the model with the strains at specified points of the system (see equation 2-38). **G** has *n*×*g* dimension, being *n* the number of DoFs (**q**) of the reduced mode, and *g* the number of points where strain is calculated (collected in the vector **g**, with *1*×*g* dimension).

$$\mathbf{g}(t) = \mathbf{G}\mathbf{q}(t) \qquad 2\text{-}38$$

For each DoF of the reduced model (*1* to *n*), the strain results offered by the FEM model at each specified point is collected ($\varepsilon_{1,1}$ to $\varepsilon_{n,g}$), as seen in equation 2-39. If a reduced model with cartesian DoFs is used (such as a GR model), each row of **G** is obtained by applying a unitary load at each DoF in a static analysis, keeping the rest of them fixed. If a modal reduction is used, a normalized modal analysis must be

performed with the FEM model. Each row of **G** is obtained by collecting the strains at the specified points for each mode shape.

$$\mathbf{G} = \begin{bmatrix} \varepsilon_{1,1} & \cdots & \varepsilon_{1,g} \\ \vdots & \ddots & \vdots \\ \varepsilon_{n,1} & \cdots & \varepsilon_{n,g} \end{bmatrix} \quad \text{2-39}$$

There is an alternative consisting of obtaining a **G** matrix using the static modal reduction (SMR). This method uses a set of static deflection shapes (SDSs). Given specific boundary conditions, each SDS corresponds to a shape in which the structure deforms for a specific applied load. This **G** matrix can only be used for cases where only static and quasi-static loads are applied, and no dynamic excitations are expected in the structure.

2.8 Direct strain observer

The direct strain observer is a VS method that consists of the open-loop simulation of a state-space model of a structural system, with the aim of obtaining strain measurements at selected points. To use this VS method, the external loads applied to the real system must be known.

If an MCK model is available (with mass, damping and stiffness matrices, see equation 2-1), it is possible to obtain the value of the model states (displacements of the DoFs and their consequent derivatives) over time under both static/quasistatic and dynamic loads. A second-order differential system of equations must be solved, for which numerical integration must be applied using an ODE-type solver. Initial conditions, integration time step, and a vector of external loads for each time step must be provided to obtain the value of the mode states over time.

Assuming a structural system subjected only to static or quasistatic loads (which do not cause dynamic effects), there is a linear relation between the loads applied and the displacements. Considering this, the stiffness matrix **K** relates the applied loads **f** with the displacements **q** of each DoF of a model (see equation 2-40). With the measured external loads, the displacements of the DoF model for each time step are obtained using the inverse of **K** (see equation 2-41), not being necessary to use an ODE-type solver.

$$\mathbf{K}\mathbf{q}(t) = \mathbf{f}(t) \tag{2-40}$$

$$\mathbf{q}(t) = \mathbf{K}^{-1}\mathbf{f}(t) \tag{2-41}$$

In both cases, it is possible to obtain strain measurements at selected points from the displacements of the DoF, using the relation shown in equation 2-38. A **G** strain matrix must be available (see equation 2-39).

The direct observer is an open-loop VS method, so the precision of the estimated measurements is limited by the precision with which the used model is able to replicate the behaviour of the real structural system and by the quality of the input measurements. Because it is a deterministic method and there is no feedback data from the real system, there is no improvement of the estimations provided by the virtual sensors.

2.9 Least Squares Strain Estimation

The Least Squares Strain Estimation (LSSE) is a VS algorithm that allows to estimate unmeasured strains from strain data only. It is a deterministic algorithm that uses a matrix generalized inversion to obtain the best fit solution of the unknown strains (using a least squares approximation). The LSSE uses the Moore-Penrose pseudoinverse, a numeric method that allows to obtain an approximation of the generalized inverse of any squared or non-squared matrix.

In a linear structural system, the displacements **q**, and the measured strains **zi** at certain points of the structure are linearly related, so it is possible to relate the displacements with the strains through the strain matrix **G** (see equation 2-39).

To apply the LSSE, the **G** matrix is divided in two parts. $\mathbf{G_i}$ is the corresponding part with the measured strains ($\mathbf{z_i}$), with $n \times o$ dimension (being o the number of measured strains, and n the number of considered DoF of the model) (see equation 2-42). $\mathbf{G_{VS}}$ is the corresponding part with the virtual strain sensors ($\mathbf{z_{VS}}$), with $n \times v$ (being v the number of unknown strains) (see equation 2-43). The size of full matrix **G**, with $n \times g$ dimension, being $g = v + o$.

$$\mathbf{z_i}(t) = \mathbf{G_i}\,\mathbf{q}(t) \qquad 2\text{-}42$$

$$\mathbf{z_{vs}}(t) = \mathbf{G_{vs}}\,\mathbf{q}(t) \qquad 2\text{-}43$$

Using $\mathbf{G_i}^+$ (the generalized inverse of $\mathbf{G_i}$), the statements 2-42 and 2-43 can be combined to obtain estimation of a set of unknown strains from a limited number of real strain measurements, as seen in statement 2-44.

$$\mathbf{z_{vs}}(t) = \mathbf{G_{vs}}\left[\mathbf{G_i}^+\,\mathbf{z}(t)\right] \qquad 2\text{-}44$$

Three cases can be distinguished when the LSSE is implemented: if the number of measurements o is equal to the number of DoFs n, the statement 2-43 is determined and the solution is found by the algorithm. If o is higher than n, the mentioned statement is overdetermined. If, on the contrary, o is lower than n, the mentioned

statement is underdetermined. In the last two cases, the LSSE gives a best-fit approximation of the solution.

Unlike other virtual sensing algorithms, the LSSE does not have an observability parameter that clearly indicates whether the system is observable or not, but an equivalent can be defined using the condition number of $\mathbf{G_i}$: $cond(\mathbf{G_i})$. If $cond(\mathbf{G_i})$ is low (close to 1), a good approximation of the solution can be provided by the LSSE. If $cond(\mathbf{G_i})$ is high, the statement 2-43 is ill-conditioned and significant errors can be expected in the solution.

2.10 Kalman filter

The KF is a recursive Bayesian algorithm used to estimate the hidden states of a system. This means that, each time step, the algorithm uses a model of the system to make predictions of the states, and a limited number of measurements to correct the made predictions (see **Figure 2-10**). Commonly, the KF is implemented using a discrete-time approach, which implies that some of the matrices used by the filter must be discretized.

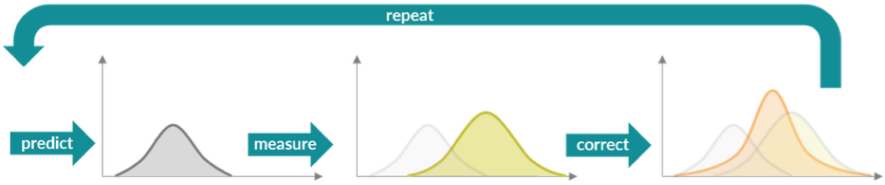

Figure 2-10 *Simplified scheme of the operation of the Kalman filter. Source:* https://www.ceva-ip.com/

The KF uses a physical model (a model composed of physical parameters that replicates the behaviour of a real system) in state-space notation. The state variables are gathered in the states vector **x** (with $1 \times 2n$ size, being n the number of DoFs of the model). The sensor data is also gathered in the measurement vector **z** (with $1 \times r$ size, being r the number of sensors). The uncertainties associated to the model and to the sensor data are gathered in the vectors **w** and **v**, with $1 \times 2n$ and $1 \times r$ size respectively. In these vectors, the uncertainties are assumed to be zero-mean white noises, incorporating the variance of each variable (w_1 to w_{2n} and v_1 to v_r).

For using the KF in a discrete-time approach, a discrete state-space model ($\mathbf{A_d}$ and $\mathbf{B_d}$) is used to obtain a prediction of the states ($\mathbf{x}(t)$) using the states of the previous time iteration ($\mathbf{x}(t-1)$) and the current external inputs ($\mathbf{u}(t)$) (see equation 2-45). The sensor data included in the measurement vector ($\mathbf{z}(t)$) is related with the predicted states through the measurement matrix **H** (also known as observation matrix) and the

input measurement matrix **J** (also known as input observation matrix), as seen in equation 2-46.

$$\mathbf{x}(t) = \mathbf{A_d}\mathbf{x}(t-1) + \mathbf{B_d}\mathbf{u}(t) + \mathbf{w} \quad \text{2-45}$$

$$\mathbf{z}(t) = \mathbf{H}\mathbf{x}(t) + \mathbf{J}\mathbf{u}(t) + \mathbf{v} \quad \text{2-46}$$

H (also known as observation matrix) is a Jacobian matrix that relates each sensor measurement with their corresponding states. **H** has $r \times 2n$ dimension. If strain and acceleration measurements are available, with the vector **z** containing a number of displacements, b number of velocities, c number of accelerations and y number of strains (being $r=a+b+c+y$), **H** is built as seen in equation 0-47. Factors α equal 1 when displacement or velocity measurements have direct correspondence with model states. The strain measurements are related to the modal states of the model using the modal strain factors, obtained from the strain matrix **G** (see equation 2-39). The acceleration measurements are related to the modal states of using the corresponding rows of the **M**, $\mathbf{C_D}$ and **K** matrices. a

$$\mathbf{H} = \begin{bmatrix} \alpha_{1,1} & \cdots & 0 & 0 & \cdots & 0 \\ \vdots & \ddots & \vdots & \vdots & \ddots & \vdots \\ 0 & \cdots & \alpha_{a,n} & 0 & \cdots & 0 \\ 0 & \cdots & 0 & \alpha_{1,1} & \cdots & 0 \\ \vdots & \ddots & \vdots & \vdots & \ddots & \vdots \\ 0 & \cdots & 0 & 0 & \cdots & \alpha_{b,n} \\ -\mathbf{M_{1,1}}^{-1}\mathbf{K_{1,1}} & \cdots & -\mathbf{M_{1,n}}^{-1}\mathbf{K_{1,n}} & -\mathbf{M_{1,1}}^{-1}\mathbf{C_{1,1}} & \cdots & -\mathbf{M_{1,n}}^{-1}\mathbf{C_{1,n}} \\ \vdots & \ddots & \vdots & \vdots & \ddots & \vdots \\ -\mathbf{M}_{c,1}^{-1}\mathbf{K}_{c,1} & \cdots & -\mathbf{M}_{c,n}^{-1}\mathbf{K}_{c,n} & -\mathbf{M}_{c,1}^{-1}\mathbf{C}_{c,1} & \cdots & -\mathbf{M}_{c,n}^{-1}\mathbf{C}_{c,n} \\ \varepsilon_{1,1} & \cdots & \varepsilon_{1,n} & 0 & \cdots & 0 \\ \vdots & \ddots & \vdots & \vdots & \ddots & \vdots \\ \varepsilon_{y,1} & \cdots & \varepsilon_{y,n} & 0 & \cdots & 0 \end{bmatrix} \quad \text{0-47}$$

If information about the external inputs is available, the input measurement matrix **J** is also present, with $r \times n$ dimension (see equation 2-48). This matrix relates the acceleration measurements with the external inputs using the mass matrix.

$$\mathbf{J} = \begin{bmatrix} 0 & \cdots & 0 \\ \vdots & \ddots & \vdots \\ 0 & \cdots & 0 \\ 0 & \cdots & 0 \\ \vdots & \ddots & \vdots \\ 0 & \cdots & 0 \\ \mathbf{M_{1,1}}^{-1} & \cdots & \mathbf{M_{1,n}}^{-1} \\ \vdots & \ddots & \vdots \\ \mathbf{M_{c,1}}^{-1} & \cdots & \mathbf{M_{c,n}}^{-1} \\ 0 & \cdots & 0 \\ \vdots & \ddots & \vdots \\ 0 & \cdots & 0 \end{bmatrix} \quad 2\text{-}48$$

The KF is a stochastic estimation algorithm, which means that it works assuming that both the model and the measurements have uncertainties associated, and also considers that the errors (the differences between the predictions and the measurements) have a Gaussian normal distribution. The uncertainties are managed using covariance matrices, which are squared matrices that incorporate on their diagonal the variance of the uncertainty associated to each variable of a vector, and in their non-diagonal positions, the correlated variances (covariances) between variables of the vector. The covariance matrix of a vector **x** with *n* variables is Σ (see equation 2-49). If it is considered that the variables of the vector are not correlated with each other, the covariance matrix can be simplified to a diagonal matrix (see equation 2-50).

$$\Sigma = \begin{bmatrix} \mathrm{Var}(\mathrm{x}_1) & \cdots & \mathrm{Cov}(\mathrm{x}_1, \mathrm{x}_\mathrm{n}) \\ \vdots & \ddots & \vdots \\ \mathrm{Cov}(\mathrm{x}_\mathrm{n}, \mathrm{x}_1) & \cdots & \mathrm{Var}(\mathrm{x}_n) \end{bmatrix} \quad 2\text{-}49$$

$$\Sigma = \mathrm{diag}(x_1, x_2, \ldots, x_n) \quad 2\text{-}50$$

In the KF, the uncertainties associated to the states of the model are managed with the matrix **Q** (with *2n*×*2n* dimension) and the uncertainties associated to the measurements are managed with the matrix **R** (with *r*×*r* dimension). It is usual to simplify **Q** and **R** to diagonal matrices, assuming that states and measurements are not correlated with each other (see equations 2-51 and 2-52). When the discrete-time approach is used, a discrete transformation must be applied to **Q** and **R**, thus obtaining the discrete versions $\mathbf{Q_d}$ and $\mathbf{R_d}$ (see equations 2-53 and 2-54). These

matrices are time-invariant. For simplicity, it is common to specify Q and R as values (being Q the diagonal values of **Q**, and R the different values of the diagonal of **R).**

$$\mathbf{Q} = \text{diag}(w_1, w_2 \dots, w_{2n}) \quad 2\text{-}51$$

$$\mathbf{R} = \text{diag}(v_1, v_2 \dots, v_r) \quad 2\text{-}52$$

$$\mathbf{Q_d} = (\mathbf{A_d Q A_d}^{\mathbf{T}})\Delta t \quad 2\text{-}53$$

$$\mathbf{R_d} = \mathbf{R}\frac{1}{\Delta t} \quad 2\text{-}54$$

The KF works in two phases: the prediction phase and the update phase. First, in the prediction phase, the algorithm uses the model to estimate the state variables (**x**(t)) using information of the previous states (**x**(t-1)) and the current inputs (in the case of structural systems, the inputs correspond to external loads **u**(t)). Then, in the update phase, the predicted state variables are corrected ($\mathbf{x}(t)^{updated}$) using the error between the measurements and their corresponding states (**z**(t) – **Hx**(t)). The algorithm is implemented in five substeps, which are executed iteratively each time step:

In the first substep (statement 2-55), a prediction of the states (**x**(t)) is made using the discretized model ($\mathbf{A_d}$ and $\mathbf{B_d}$), the current inputs (**u**(t)) and the corrected states of the previous iteration (**x**(t-1)).

$$\mathbf{x}(t) = \mathbf{A_d x}(t-1) + \mathbf{B_d u}(t) \quad 2\text{-}55$$

In the second substep (statement 2-56), a prediction of the filter covariance (**P**(t)) is made using the corrected covariance of the previous iteration (**P**(t-1)) and the covariance matrix of the model ($\mathbf{Q_d}$).

$$\mathbf{P}(t) = \mathbf{A_d P}(t-1)\mathbf{A_d}^{\mathbf{T}} + \mathbf{Q_d} \quad 2\text{-}56$$

In the third substep (statement 2-57), the gain of the filter (**K**(t)) is updated using the prediction of the filter covariance (**P**(t)), the measurement matrix (**H**) and the covariance matrix of the measurements ($\mathbf{R_d}$).

$$\mathbf{K}(t) = \mathbf{P}(t)\mathbf{H}^{\mathbf{T}}(\mathbf{H}\mathbf{P}(t)\mathbf{H}^{\mathbf{T}} + \mathbf{R_d})^{-\mathbf{1}} \quad 2\text{-}57$$

In the fourth substep (statement 2-58), the prediction of the states is updated ($\mathbf{x}(t)^{updated}$) using the error between the measurements ($\mathbf{z}(t) - \mathbf{H}\mathbf{x}(t)$) and the calculated gain ($\mathbf{K}(t)$).

$$\mathbf{x}(t)^{\mathbf{updated}} = \mathbf{x}(t) + \mathbf{K}(t)(\mathbf{z}(t) - \mathbf{H}\mathbf{x}(t)) \quad 2\text{-}58$$

In the fifth and last substep (statement 2-59), the prediction of the filter covariance is updated ($\mathbf{P}(t)^{updated}$) using the calculated gain ($\mathbf{K}(t)$).

$$\mathbf{P}(t)^{\mathbf{updated}} = \mathbf{P}(t) - \mathbf{K}(t)\mathbf{H}\mathbf{P}(t) \quad 2\text{-}59$$

If load measurements are not available, the first substep of the KF (statement 2-55) is simplified in the statement 2-60.

$$\mathbf{x}(t) = \mathbf{A_d}\mathbf{x}(t-1) \quad 2\text{-}60$$

The observability of the KF is defined as the capacity of the algorithm to obtain enough information from the real system (through the input sensors and the observation matrix) to be able to estimate all the states. To determine if a KF is observable, the observability matrix **O** is calculated using the transpose of **A** and the measurement matrix **H** (see equation 2-61). Only if the rank of **O** is equal to *2n* (the number of states of the model) is the KF fully observable. Otherwise, the KF is not observable and significant errors in the estimations can be expected.

$$\mathbf{O} = \begin{bmatrix} \mathbf{A}^{\mathbf{T}}\mathbf{H}^{\mathbf{0}} \\ \mathbf{A}^{\mathbf{T}}\mathbf{H}^{\mathbf{1}} \\ \vdots \\ \mathbf{A}^{\mathbf{T}}\mathbf{H}^{\mathbf{2n-1}} \end{bmatrix} \quad 2\text{-}61$$

2.11 Augmented Kalman filter

The AKF is the result of the combination of a KF with an augmented state-space model, which is a model state-space model in which external inputs are also considered states. Because of this, the AKF, applied to structures, can estimate the unknown external loads.

The augmented states vector **x*** (see equation 2-62), with $2n+n_f$ dimension being n_f the number of external loads, is built by combining the states vector **x** (see equation 2-4) with the inputs vector **u** (see equation 2-6). The augmented state-space model **A*** (see equation 2-63) is built by combining the model matrices **A** and **B** (see equations 2-7 and 2-8). The discretization of **A*** ($\mathbf{A_d}$*) is shown in equation 2-64.

$$\mathbf{x}^* = \begin{pmatrix} \mathbf{q} \\ \dot{\mathbf{q}} \\ \mathbf{u} \end{pmatrix} \tag{2-62}$$

$$\mathbf{A}^* = \begin{bmatrix} \mathbf{A} & \mathbf{B} \\ \mathbf{0} & \mathbf{0} \end{bmatrix} \tag{2-63}$$

$$\mathbf{A_d}^* = \begin{bmatrix} \mathbf{A_d} & \mathbf{B_d} \\ \mathbf{0} & \mathbf{I} \end{bmatrix} \tag{2-64}$$

In the AKF, the unknown inputs are modelled using a zero-mean random walk model, incorporated into the inputs covariance matrix $\mathbf{Q_u}$. The discretized augmented covariance matrix of the model ($\mathbf{Q_d}$*) is built by combining the discretized model covariance matrix and the inputs covariance matrix (see equation 2-65). For simplicity, it is common to specify Q_u as a value.

$$\mathbf{Q}^* = \begin{bmatrix} \mathbf{Q_d} & \mathbf{0} \\ \mathbf{0} & \mathbf{Q_u} \end{bmatrix} \tag{2-65}$$

In the AKF, an augmented measurement matrix **H*** (see equation 2-66) is used to relate the measured data with the augmented model states, built by combining the **H** and **J** matrices (see equations 0-47 and 2-48).

$$\mathbf{H}^* = [\mathbf{H} \quad \mathbf{J}] \tag{2-66}$$

The implementation of the AKF is similar to that of KF. In discrete-time approach, the AKF is implemented in five substeps, which are executed iteratively each time step:

In the first substep (statement 2-67), a prediction of the augmented states (**x***(t)) is made using the discretized augmented model (**Ad***), and the corrected augmented states of the previous iteration (**x***(t-1)).

$$\mathbf{x}^*(t) = \mathbf{A_d}^*\mathbf{x}^*(t-1) \qquad 2\text{-}67$$

In the second substep (statement 2-68), a prediction of the filter covariance (**P**(t)) is made using the corrected covariance of the previous iteration (**P**(t-1)) and the augmented covariance matrix of the model ($\mathbf{Q^*_d}$).

$$\mathbf{P}(t) = \mathbf{A_d}^*\mathbf{P}(t-1)\mathbf{A_d}^{*\mathbf{T}} + \mathbf{Q}^*_{\mathbf{d}} \qquad 2\text{-}68$$

In the third substep (statement 2-69), the gain of the filter (**K**(t)) is updated using the prediction of the filter covariance (**P**(t)), the augmented measurement matrix (**H***) and the covariance matrix of the measurements ($\mathbf{R_d}$).

$$\mathbf{K}(t) = \mathbf{P}(t)\mathbf{H}^{*\mathbf{T}}(\mathbf{H}^*\mathbf{P}(t)\mathbf{H}^{*\mathbf{T}} + \mathbf{R_d})^{-\mathbf{1}} \qquad 2\text{-}69$$

In the fourth substep (statement 2-70), the prediction of the augmented states is updated (**x***(t)$^{\text{updated}}$) using the error between the measurements (**z**(t) – **H*x***(t)) and the calculated gain (**K**(t)).

$$\mathbf{x}^*_{\mathbf{t}}{}^{\mathbf{updated}} = \mathbf{x}^*(t) + \mathbf{K}(t)(\mathbf{z}(t) - \mathbf{H}^*\mathbf{x}^*(t) \qquad 2\text{-}70$$

In the fifth and last substep (statement 2-71), the prediction of the filter covariance is updated (**P**(t)$^{\mathbf{updated}}$) using the calculated gain (**K**(t)).

$$\mathbf{P}(t)^{\mathbf{updated}} = \mathbf{P}(t) - \mathbf{K}(t)\mathbf{H}^*\mathbf{P}(t) \qquad 2\text{-}71$$

The observability of the AKF is defined in a similar way as in the KF. To determine if a KF is observable, the augmented observability matrix **O*** is calculated using the transpose of **A*** and the measurement matrix **H***. Only if the rank of **O*** is equal to

$2n+n_f$ (the number of states of the model), the AKF is fully observable. Otherwise, the AKF is not observable and significant errors in the estimations can be expected.

$$\mathbf{O}^* = \begin{bmatrix} \mathbf{A}^{*\mathbf{T}}\mathbf{H}^{*\mathbf{0}} \\ \mathbf{A}^{*\mathbf{T}}\mathbf{H}^{*\mathbf{1}} \\ \vdots \\ \mathbf{A}^{\mathbf{T}}\mathbf{H}^{\mathbf{2n-1}} \end{bmatrix} \qquad 2\text{-}72$$

A particularity of the AKF with respect to observability is that it must be differentiated the observability of the states from the observability of the total augmented states (including the external inputs). If the rank of **O*** is lower than $2n+n_f$ but equal to or greater than $2n$, the states of the system may be observable but external inputs not. This situation can be of interest in the case of the external inputs are unknown but the unknown variables that are of interest to estimate are others.

2.12 Static Strain Kalman filter

The Static Strain Kalman filter (SSKF) is a specific case of KF implementation proposed in this thesis, used to estimate strain using a SMR model. It is a VS stochastic model-based algorithm which allows to estimate the strain at unmeasured points, from input strain measurements.

The state vector **x** contains as many states as DoFs are considered in the model. Each DoF corresponds to a SDS of the structure. The size of **x** is *1*×*n*, being *n* the number of states of the KF (corresponding to the number of static modes considered). The model matrix **A** is created, using an identity matrix with *n*×*n* dimension (see equation 2-73). $\mathbf{A_d}$ is discretized using equation 2-12, being Δt the used time step.

$$\mathbf{A} = \mathbf{I_n} \tag{2-73}$$

The measurement matrix **H** relates the measured strains with their corresponding states, with *i*×*n* dimension, being *i* the number of input strain sensors. **H** corresponds to $\mathbf{G_i}$ matrix (see equation 2-74), the part of **G** that contains the strain measurement points corresponding to the input gauges (as explained in equation 2-42). Like the LSSE, the SSKF allows to work considering several static modes (as many as **G** includes), being able to consider different load cases.

$$\mathbf{H} = \mathbf{G_i} \tag{2-74}$$

Like the KF, the SSKF is implemented in five substeps, which are executed iteratively each time step: In the first substep (statement 2-75), a prediction of the present states (**x**(t)) is obtained using the model (**A**) and the corrected prediction of the previous iteration (**x**(t-1)).

$$\mathbf{x}(\mathrm{t}) = \mathbf{A_d}\mathbf{x}(\mathrm{t}-1) \tag{2-75}$$

In the second substep (statement 2-76), a prediction of the filter covariance (**P**(t)) is made using the corrected covariance of the previous iteration (**P**(t-1)) and the covariance matrix of the model (**Q**).

$$\mathbf{P}(t) = \mathbf{A_d}\mathbf{P}(t-1)\mathbf{A_d}^{\mathbf{T}} + \mathbf{Q} \qquad 2\text{-}76$$

In the third substep (statement 2-77), the gain of the filter (**K**(t)) is updated using the prediction of the filter covariance (**P**(t)), the measurement matrix (**H**) and the covariance matrix of the measurements (**R**).

$$\mathbf{K}(t) = \mathbf{P}(t)\mathbf{H}^{\mathbf{T}}(\mathbf{H}\mathbf{P}(t)\mathbf{H}^{\mathbf{T}} + \mathbf{R})^{-\mathbf{1}} \qquad 2\text{-}77$$

In the fourth substep (statement 2-78), the prediction of the states is updated (**x**(t)$^{\mathbf{updated}}$) using the error between the measurements (**z**(t) – **Hx**(t)) and the calculated gain (**K**(t))

$$\mathbf{x}(t)^{\mathbf{updated}} = \mathbf{x}(t) + \mathbf{K}(t)(\mathbf{z}(t) - \mathbf{H}\mathbf{x}(t)) \qquad 2\text{-}78$$

In the fifth and last substep (statement 2-79), the prediction of the filter covariance is updated (P(t)updated) using the calculated gain (K(t)).

$$\mathbf{P}(t)^{\mathbf{updated}} = \mathbf{P}(t) - \mathbf{K}(t)\mathbf{H}\mathbf{P}(t) \qquad 2\text{-}79$$

After each iteration of the SSKF, the virtual strain sensors values **y** are obtained from the states vector **x** through de outputs matrix **C**. If it is of interest to obtain all the strain values (inputs and outputs) as output values of the filter, **C** corresponds to $\mathbf{G_{VS}}$ (with $n \times g$ dimension), and **y** has $1 \times g$ dimension (statement 2-80).

$$\mathbf{y}(t) = \mathbf{C}\mathbf{x}(t) \qquad 2\text{-}80$$

2.13 Evaluation indicators

In order to evaluate the performance of the VS algorithms, different evaluation indicators are used.

In the case of time series of regular nature (such as the load cycles applied in a fatigue test), the use of three indicators are proposed for comparing virtual measurements (est) with their real counterparts (ref): the relative error of the mean in the estimated signals (e. mean), the relative error of the range in the estimated signals (e. range) and the Relative Root Mean Square Error (RRMSE). The definitions of these three indicators are seen in equation 2-81, equation 2-82 and equation 2-83, respectively.

$$\text{e. mean } [\%] = \left|\frac{\text{mean}_{\text{est}} - \text{mean}_{\text{ref}}}{\text{mean}_{\text{ref}}}\right| \times 100 \qquad 2\text{-}81$$

$$\text{e. range } [\%] = \left|\frac{\text{range}_{\text{est}} - \text{range}_{\text{ref}}}{\text{range}_{\text{ref}}}\right| \times 100 \qquad 2\text{-}82$$

$$\text{RRMSE } [\%] = \frac{\text{RMSE}(\text{ref}, \text{est})}{\text{mean}_{\text{ref}}} \times 100 \qquad 2\text{-}83$$

In the case of time series of a more variable nature (such as loads due to stochastic events to which a machine or structure may be subjected), it is proposed to add an extra indicator to the previously mentioned selection: the Pearson correlation coefficient (PCC). This indicator is a normalized measurement of the covariance between the est and ref signals. The PCC is obtained with the quotient of the cross-covariance between est and ref signals and the product of the standard deviations of est and ref signals (see equation 2-84). The rank of the PCC is from -100% to 100%. A PCC of 100% means that the est and ref signals are fully correlated. A PCC of 0% means that there is no correlation between the est and ref signals. A PCC of -100% means that the est and ref signals have an inverse correlation.

$$\text{PCC } [\%] = \frac{\text{cov}(\text{ref}, \text{est})}{\sigma_{\text{est}}\sigma_{\text{ref}}} \times 100 \qquad 2\text{-}84$$

To correctly use the PCC to compare two signals, the possible time delay that exists between them must be compensated. For this, an algorithm iteratively applies the

normalized cross-correlation between the two signals (est and ref), "moving" one relative to the other, looking for the delay where the cross-correlation is maximized.

There may be some cases where the RRMSE is not suitable for comparing signals. For example, if two signals whose mean is close to zero are compared using the RRMSE, denominator in equation 2-83 will be close to zero, causing the RRMSE values to be very high, therefore giving erroneous information in the comparison of signals. In cases where this is expected to happen, it is suggested to use an alternative indicator to replace the RRMSE: the percent error (e%) (see equation 2-85).

$$e\% = \left|1 - \frac{\sigma_{est}}{\sigma_{ref}}\right| \times 100 \qquad 2\text{-}85$$

Chapter 3

FATIGUE

3.1 Introduction

Material fatigue is the phenomenon that describes the degradation of a material subjected to cyclic loads, even when these loads are below the yield strength of the material.

The phenomenon of fatigue of materials can be explained mainly in two phases: the crack initiation and the crack propagation until the final breakage of the material. In the first phase, cracks nucleate from internal discontinuities in the material structure after a certain number of cyclic loads. These discontinuities are usually dislocations in the atomic or molecular structure, interfaces between crystals or defects already present from the manufacturing phase (such as air bubbles). Once a crack has started and has achieved a minimum size, if cyclic loading continues, the crack propagates through the material, thus occurring the crack-growth phase. When the crack has propagated enough to compromise the integrity of the material, the final failure can occur if the affected component has not been detected and replaced on time (see **Figure 3-1**) [5].

Figure 3-1 *Broken steel part due to fatigue. Source: https://commons.wikimedia.org/*

The phenomenon of fatigue was detected for the first time at the beginning of the industrial era, in the first half of the 19th century. In the 1830s, it was detected that

wagon and locomotive axles broke when subjected to loads below their design resistance limit (see **Figure 3-2**). Research on this new phenomenon grew exponentially after the fateful train accident on the Paris-Versailles line in 1842. Between 1860 and 1870, the German engineer A. Wohler studied extensively the breakage of train axles due to fatigue, developing the SN curves (also known as Wohler diagrams) [99]. These curves are still today a fundamental tool in the design of structures and machine components, to estimate their fatigue life or to make possible to achieve fatigue resistant designs.

Figure 3-2 *Train accident in England, happened in the 2000s, caused by fatigue of materials. Fatigue is still a major concern in engineering. Source: https://www.bbc.com/*

3.2 SN curves and damage calculation

SN curves are graphical representations that shows the relation between the number of load cycles (N) and the stress level (S or σ) required to produce failure in a material under cyclic loading conditions. SN curves were originally conceived as semi-log diagrams, with a logarithmic X axis (number of load cycles) and a linear Y axis (stress level).

When plotting the SN curve of specific materials, mainly two types of behaviour were observed: some materials (such as aluminium) show a SN curve with a tendency to reach a stress value of 0 after a high number of cycles, and some materials (such as steel) show a SN curve that stabilizes at an asymptote at certain number of cycles (see **Figure 3-3**). In the latter case, this stress value at which the stress limit to fatigue stabilizes is considered the endurance limit of fatigue (σ_{EL}), and below this limit, is considered that the cyclic loads do not cause fatigue damage to the material [5]. Non-metallic materials, such as polymers or composites, can show abnormal fatigue behaviours [100].

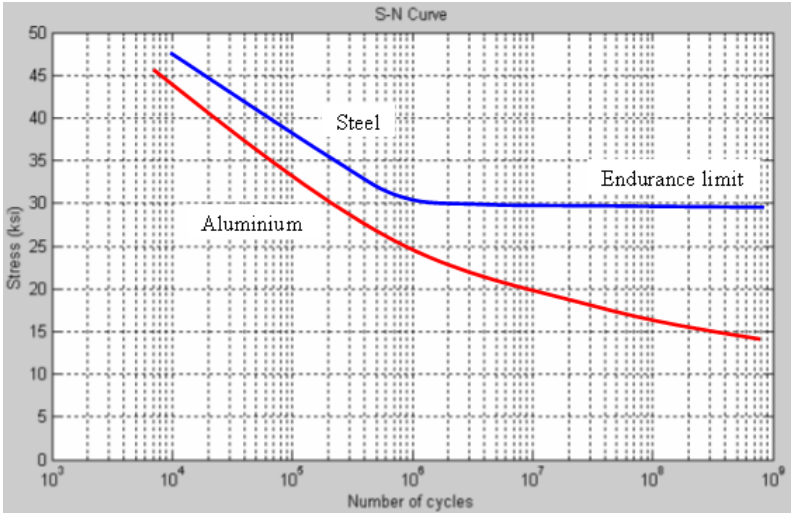

Figure 3-3 *Examples of aluminium (red) and steel (blue) SN curves, in semi-log representation. Source: https://commons.wikimedia.org/*

In 1910, the American engineer O.H. Basquin gave a new approach to the SN curves. He plotted the SN curve in a log-log diagram and simplified it into a piecewise function of straight sections, each representing a different phase of fatigue in the material [101]. SN curves of materials without endurance limit of fatigue are represented with a straight section, corresponding to the elastic deformation region (starting at the level of the yield limit stress σ_{YS} and ending at 0) The SN curves of materials with endurance limit of fatigue are represented with two straight sections: one straight section corresponding to the elastic deformation region (starting at the level of yield stress limit (σ_{YS}) and ending at the level of endurance limit (σ_{EL})) and one straight section corresponding to the infinite life region (with the constant value of σ_{EL}), in which cyclic loads are expected to not cause fatigue damage. For the elastic deformation region, Basquin proposed the following relation (see equation 3-1). For a specific range of stress cycles $\Delta\sigma$, the expected number of load cycles until the fatigue failure (N_f) is determined by the constant values *b* and C_1 (specific to each material).

$$N_f{}^b = \frac{C_1}{\Delta\sigma} \qquad 3\text{-}1$$

On most metals, a change on the fatigue behaviour can be observed around $N=10^4$. Above that number of cycles, the level of stress is below σ_{YS} and only elastic deformations occur in the material. This type of fatigue is known as high-cycle fatigue (HCF) Below that number of cycles, the level of stress is between the ultimate tensile strength (σ_{UTS}) and σ_{YS}, and permanent plastic deformations occur in the material. This type of fatigue is known as low-cycle fatigue (LCF) [102]

In the 1950s, the engineers S.S Manson and L.F Coffin proposed a new approach for the LCF, based on strain instead of stress (see equation 3-2). For the LCF case, they proposed the εN curve (strain-cycles) as a more appropriate alternative to the SN curve. In a log-log diagram, the Coffin-Manson law relates the expected number of load cycles until the fatigue failure N_f and the plastic strain range $\Delta\varepsilon_p$, through the constant values *c* and C_2, specific to each material (see **Figure 3-4**) [103].

$$N_f{}^{c} = \frac{C_2}{\Delta\varepsilon_p} \qquad 3\text{-}2$$

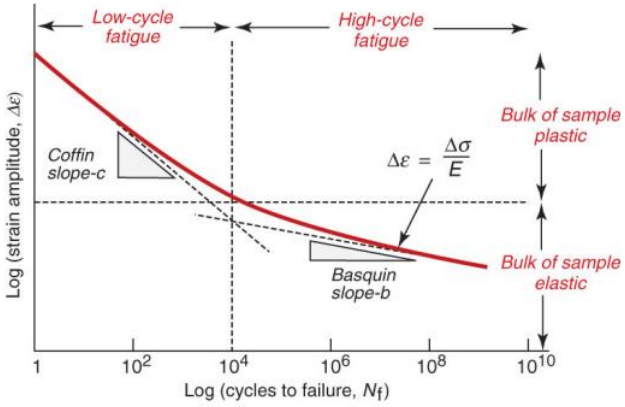

Figure 3-4 *Combination of the Coffin-Manson approach (for low-cycle fatigue) and Basquin approach (for high-cycle fatigue) in a log-log strain-cycles diagram. The transition between LCF and HCF occurs around 10^4 cycles. Source: https://ocw.tudelft.nl/*

In 1924, the German engineer A. Palmgren applied for first time the concept of accumulated fatigue damage in the study of ball bearings [104]. The concept was later generalized by the American M.A. Miner in 1945 [105], giving rise to the well-known Palmgren-Miner rule of cumulative damage (see equation 3-3). Being *k* the number of stress cycles, n_i the number of cycles at stress level *i* and N_i the fatigue life expected for the stress level *i*, D is the accumulated fatigue damage. When D reaches 1, it is estimated that the crack-initiation phase has ended, and a crack may appear in the critical areas of the structure or component.

$$D = \sum_{i=1}^{k} \frac{n_i}{N_i} \qquad 3\text{-}3$$

The characteristics of the load cycles suffered by the material have effects on its fatigue life. Stress cycles can be characterized according two main parameters: the stress range $\Delta\sigma$ (see equation 3-4) and the stress mean σ_m (see equation 3-5). The stress amplitude (σ_a) corresponds to one half of $\Delta\sigma$. The stress ratio R is another

parameter that tells information about the type of load cycles applied from the traction/compression approach (see equation 3-6). Fatigue tests are commonly performed with R=-1 (fully reversed condition, where $\sigma_{min} = -\sigma_{max}$) or with R=0 (pulsating condition, where $\sigma_{min}=0$ and σ_{max} is positive).

$$\Delta\sigma = \sigma_{max} - \sigma_{min} \quad 3\text{-}4$$

$$\sigma_m = \frac{\sigma_{max} + \sigma_{min}}{2} \quad 3\text{-}5$$

$$R = \frac{\sigma_{min}}{\sigma_{max}} \quad 3\text{-}6$$

While in compressive stress cycles it is not considered that there are detrimental effects due to medium and variable stress, in tensile stress cycles some changes in the behavior of fatigue are observed (see **Figure 3-5**). Three main models have been proposed to represent the mean stress effects and obtain a safety factor *FoS*: the Goodman line (see equation 3-7), the Soderberg line (see equation 3-8) and the Gerber parabola (see equation 3-9) [106].

$$\frac{1}{FoS} = \frac{\sigma_m}{\sigma_{UTS}} + \frac{\sigma_a}{\sigma_{EL}} \quad 3\text{-}7$$

$$\frac{1}{FoS} = \frac{\sigma_m}{\sigma_{YS}} + \frac{\sigma_a}{\sigma_{EL}} \quad 3\text{-}8$$

$$1 = \left(\frac{FoS\ \sigma_m}{\sigma_{UTS}}\right)^2 + \frac{FoS\ \sigma_a}{\sigma_{EL}} \quad 3\text{-}9$$

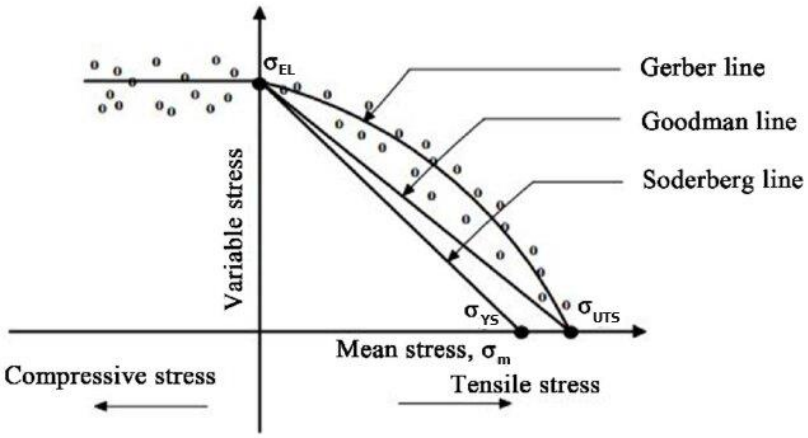

Figure 3-5 *Graphical representation of the Gerber, Goodman and Soderberg models for mean stress effects on fatigue* [107].

Frequently, a material is subjected to cyclic loads of varying amplitude over time. To calculate the accumulated fatigue damage in these cases, T. Endo and M. Matsuishi presented in 1968 the Rainflow-counting algorithm [108]. This algorithm identifies all load cycles in a strain or stress time-series, classifies them according to their range, and count how many cycles of each range there are in the analysed time-series. Different counting methods can be used, being the pagoda-roof counting the most popular (see **Figure 3-6**). The algorithm allows to identify and count both complete cycles and residual half-cycles. The Palmgren-Miner rule is applied to the final cycle count to obtain the accumulated fatigue damage.

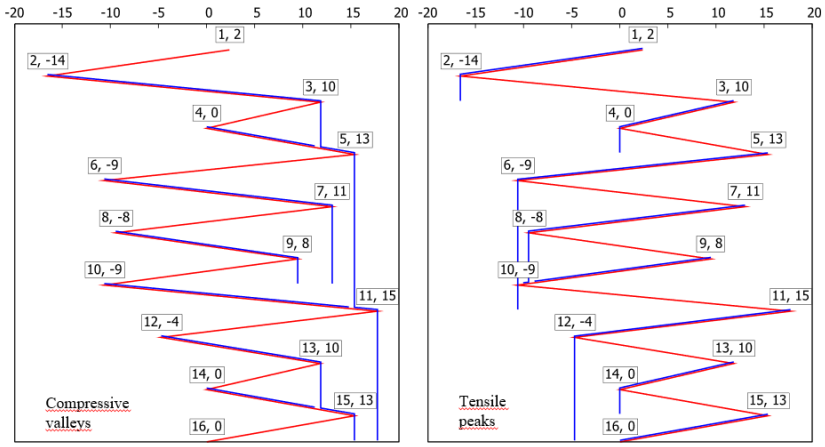

Stress (MPa)	Complete cycles	Half cycles
10	2	0
13	0	1
16	1	1
17	0	1
19	0	1
20	1	0
22	1	0
29	0	1

Figure 3-6 *Example of application of the Rainflow algorithm (using pagoda roof counting) to a time series of cyclic loads with varying amplitude. Source: https://commons.wikimedia.org/*

3.3 Crack propagation

Once a crack appears in the material, due to accumulated fatigue damage, the crack-growth phase begins, in which other type of equations must be used to calculate the remaining useful life of the material. It is considered that the useful life of the material ends when the crack reaches a critical size that compromises the security of the component or structure.

In the 1960s, P.C. Paris and F. Erdogan presented the today known as Paris law, an equation that gives the rate of growth of a fatigue crack, under cyclic loads, being *a* the crack length (see equation 3-10). ΔK is the range of stress intensity, being *Y* a factor depending on the geometry of the crack (see equation 3-11). *C* and *m* are coefficients obtained experimentally.

$$\frac{da}{dN} = C(\Delta K)^m \qquad 3\text{-}10$$

$$\Delta K = Y\Delta\sigma\sqrt{\pi a} \qquad 3\text{-}11$$

The Paris law is only effective for certain range of ΔK (see Regime B in **Figure 3-7**), between the threshold range of stress and the critical range of stress. In the following years, other generalized crack-growth equations have been proposed, such as the Walker equation and the NASGRO equation [109].

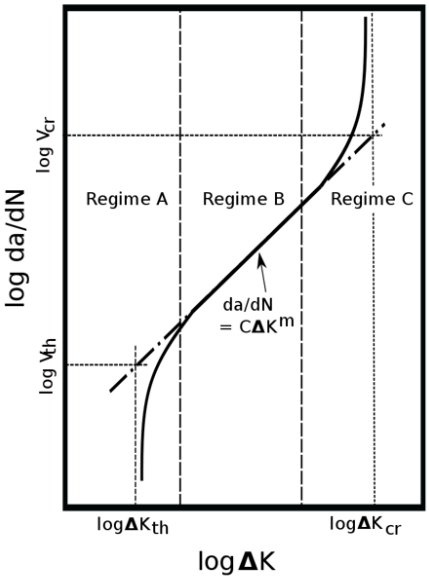

Figure 3-7 *Graphical representation of the Paris law and its range of application (corresponding to the Regime B). Source: https://commons.wikimedia.org/*

3.4 Probabilistic fatigue

It is impossible to estimate the exact number of cycles in which a material will suffer fatigue failure, due to the uncertainty associated with the fatigue phenomenon. For this reason, material fatigue is usually studied with a probabilistic approach.

The SN curves are obtained experimentally, from a set of fatigue tests. Usually, the tests are carried out in groups, at different stress levels. For each level of stress tested, the number of cycles to failure of each of the samples show a Gaussian distribution [110]. From this, mainly two statistical parameters are of interest to plot the SN curves from the experimental data: the survival probability P_R and the confidence level [111].

The P_R corresponds to a SN curve according to which the specified percentage of sample failures lie above it. For example, the SN curve of a P_R=95% is the one is the one in which 95% of fatigue failure samples remain above it (see **Figure 3-8**). After experimentally testing a specific material or component, different SN curves with different P_R are usually plotted (for example, 95, 50 and 5%). The P_R is obtained from the Gaussian tolerance interval (ρ, 1-α), which includes a proportion ρ of a sampled population with a 1-α confidence level [112].

The confidence level 1-α, sometimes given as ɣ, is a statistical parameter that indicates the percentage of certainty that the mean values of given fatigue failure samples are within a confidence interval of a Gaussian distribution (see **Figure 3-9**).

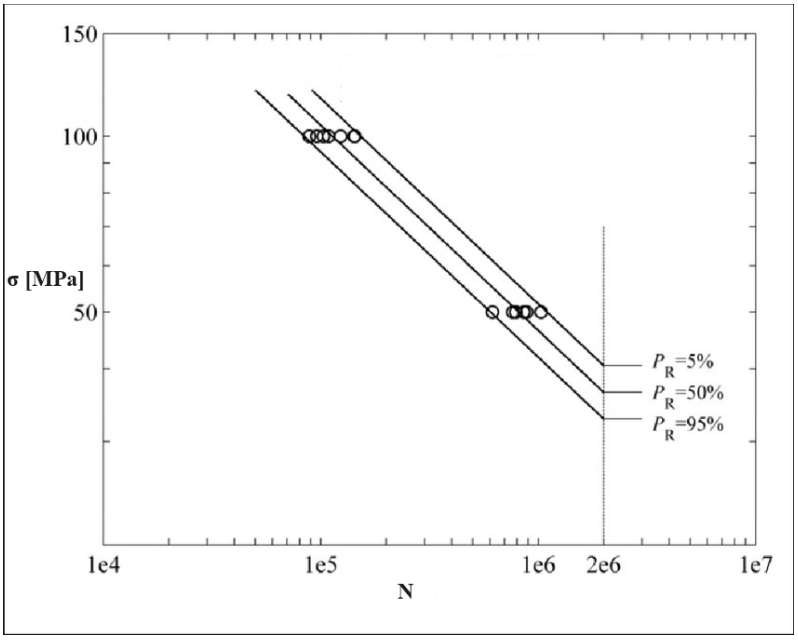

Figure 3-8 *Definition of different SN log-log curves (with different P_R) from a set of fatigue tests experimental data performed at two stress levels* [110]

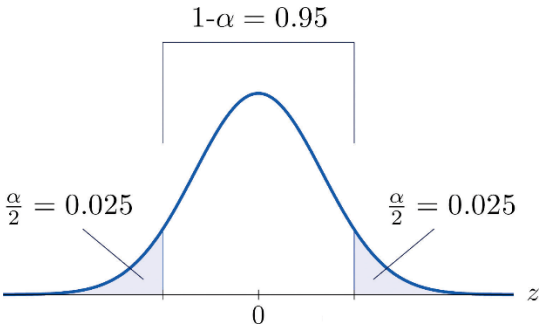

Figure 3-9 *Example of a confidence level of 95% (α = 0.05) in a Gaussian distribution. Source: https://saylordotorg.github.io/*

To study the effect of fatigue on welded components, special considerations must be taken into account. In this thesis, the recommendations for fatigue design of welded joints and components offered by the International Institute of Welding (IIW) [113] are followed.

Different approaches have been proposed to calculate the stress in welded joints. The nominal stress approach consists of the calculation of the stress in the sectional area under study, discarding local effects due to the weld geometry. The Hot Spot Stress approach (HSS) is an extrapolation of the stress in the weld toes, from stress measurements at specific distances from the toes. The HSS is especially indicated when the welded joints coincide with the critical fatigue points, and can be applied from real strain gauge measurements. The Effective Notch Stress approach (ENS) consists of the estimation of the stress directly in the root and toes of a welded joints, assuming geometric simplifications using specific notch radius. The ENS requires a FEM model where the welds are represented in detail and cannot be applied from real measurements. Different parts of a welded joint can be seen in **Figure 3-10**.

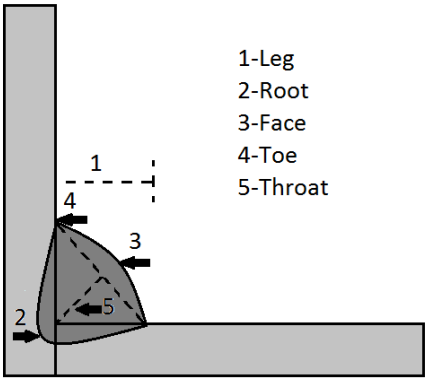

Figure 3-10 *Parts of a filled welded joint. Source: https://commons.wikimedia.org/*

In the case of the HSS method, two types of hot spots are proposed (see **Figure 3-11**).

Type A hot spots are transverse to the weld toe, located on plate surfaces. Its extrapolation is dependent on the thickness of the plate (*t*). The linear extrapolation for fine-meshed type A hot spots is shown in equation 3-12, being $\sigma_{0.4t}$ and $\sigma_{1.0t}$ the corresponding measured stress at these distances from the weld toe.

Type B hot spots are also transverse to the weld toe but located on plate edges. Its extrapolation is independent on the thickness of the plate. The quadratic extrapolation for fine-meshed type B hot spots is shown in equation 3-13, being σ_{4mm}, σ_{8mm} and σ_{12mm} the corresponding measured stress at these distances from the weld toe.

For non-finely meshed models, the hot spot extrapolations vary, depending on the size of the finite elements.

$$\sigma_{\text{HS type a}} = 1.67\sigma_{0.4t} - 0.67\sigma_{1.0t} \quad \text{3-12}$$

$$\sigma_{\text{HS type b}} = 3\sigma_{4mm} - 3\sigma_{8mm} + \sigma_{12mm} \quad \text{3-13}$$

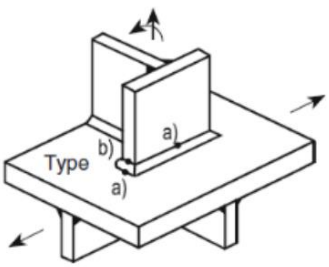

Figure 3-11 *Examples of locations of type A and type B hot spots* [113]

For fatigue in welded joints, special SN curves are provided by the IIW, called Fatigue Assessment Curves (FAT) (see **Figure 3-12**). These curves are especially indicated to work in combination with HSS. Each curve, plotted in a log-log representation, is identified according to their characteristic fatigue strength at N=2E6 (in MPa). Below N=1E7, FAT curves have a slope of m=3 (except for the FAT160 curve, with a slope of m=5). No other FAT curve can surpass the FAT160. Above

N=1E7, is assumed that FAT curves have a slope of m=22, because no endurance limit is considered for welded joints.

To estimate the fatigue life of a welded joint (using HSS), equation 3-14 can be used, being the *FAT* value the strength associated to the corresponding curve at N=2E6. FAT curves have a P_R=95%, with a confidence level of 75%. The FAT value can be modified by different factors. Two of the main factors to take into account are the thickness effect factor *f(t)* and the stress ratio effect factor *f(R)*.

$$N = 2E6 \left(\frac{FAT}{\sigma_{HS}}\right)^{m} \qquad 3\text{-}14$$

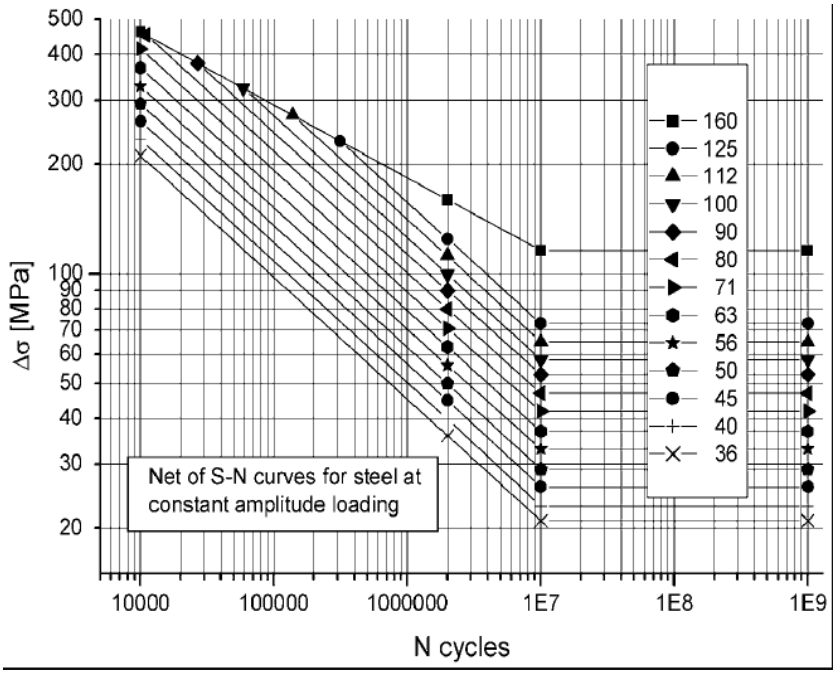

Figure 3-12 *FAT curves for steel, normal stress, standard applications* [113]

SECTION 2

Experiments performed

Chapter 4
STUDY CASE 1

4.1 Prototype description

The study case 1 consists of a scaled prototype of an offshore wind turbine (OWT). An OWT is a wind turbine specially designed for installation on the sea surface. OWTs are generally installed in groups, known as offshore wind farms (see **Figure 4-1**). Because the wind speed at sea is usually greater than on land, and that the environmental impact of wind turbines is also lower than on land, the interest in offshore wind power has grown enormously since the 2000s, even though the cost of power generation is significantly higher than with onshore wind power [114].

Figure 4-1 *Offshore wind farm beyond the horizon. Source: https://www.dailymail.co.uk/news/article-10146201*

The operation and maintenance costs of OWTs are especially significant, due both to the harsh maritime conditions to which they are subjected, and to the fact that maintenance must be carried out using specialized vessels and personnel with very specific training. Due to this, a lot of research has been conducted on this topic, with the aim of minimizing the operation and maintenance costs of OWTs and thus helping to reduce the costs of this energy source [9], [115].

Different technologies have been developed for fixing the OWTs on the seabed (see **Figure 4-2**). For shallow waters (with depth below 25m), the monopile foundation is the most used solution, and for medium depth waters (up to 50m), tripod and jacket structural supports are commonly used [114]. For depth waters, foundations fixed to the seabed are unfeasible, so floating wind turbines anchored to the seabed have been developed recently [116].

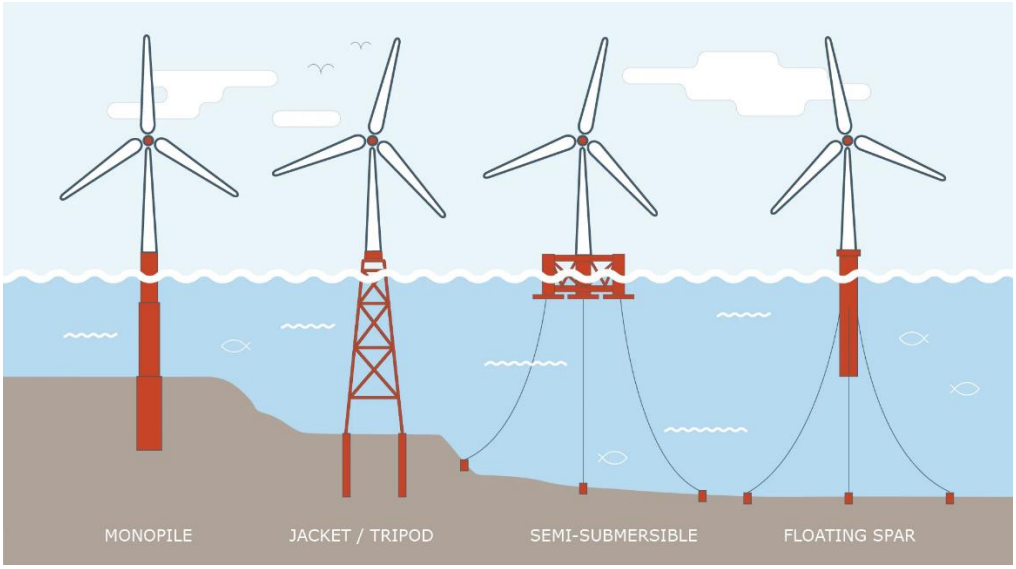

Figure 4-2 *Types of OWT foundations developed. Source: https://www.cowi.com/insights/oceans-unlocked-a-floating-wind-future*

The scaled prototype of OWT used in this study case is a simplification of an offshore wind turbine with jacket support foundation (see **Figure 4-3**). The prototype, located in a laboratory of Ikerlan, includes the jacket structure, the tower, and the nacelle, but the rotor and blades are not included. An inertial shaker is installed on the top of the prototype, with the aim of generating variable external forces on the prototype. The prototype can be seen in **Figure 4-4**.

The tower of the scaled OWT prototype is made of three segments screwed together using circular plates. The tower is screwed to the jacket-structure also using a circular plate. The nacelle consists of a square metal tube, screwed to the top of the tower

using a plate. Two square plates are welded to the upper part of the nacelle, being the shaker attached to one of them.

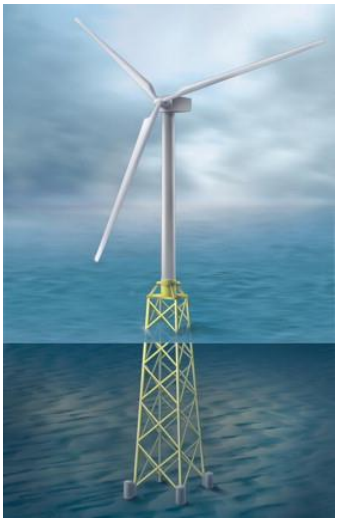

Figure 4-3 *Artwork of a jacket-supported OWT* [117]

Figure 4-4 *Scaled prototype of an OWT used in study case 1.*

The main characteristics of the scaled prototype are shown in **Table 4-1**. The characteristics of the shaker used in the prototype are shown in **Table 4-2**.

Characteristic	Value
Tower + nacelle weight	42 kg
Jacket weight	13.5 kg
Shaker + support weight	27 kg
Total weight	82.5 kg
Tower height	1790 mm
Jacket height	1300 mm
Total height	3090 mm
Material	Steel

Table 4-1 *Main characteristics of the scaled prototype of an OWT.*

Characteristic	Value
Shaker model	Data Physics IV47
Type of shaker	Inertial shaker
Inertial mass	14.5 kg
Max sinus force (peak)	250 N
Total shaker mass	21 kg
Shaker main mode freq.	20 Hz

Table 4-2 *Main characteristics of the shaker.*

Initially, the prototype was simply supported on the ground by four rubber pads, which caused a certain degree of uncertainty and non-linearity in the dynamic behavior of the prototype (see **Figure 4-5**). Moreover, the shaker was fixedly

installed using a steel coupling screwed onto the nacelle, which meant that the direction of the applied forces could not be varied (see **Figure 4-6**).

Figure 4-5 *Rubber pads on which the OWT prototype rested.*

Figure 4-6 *Shaker was fixed to the OWT prototype using a screwed steel coupling.*

Some improvements have been implemented in the prototype. The four rubber pads that supported the prototype have been replaced by four fixed supports to a concrete block of large dimensions, to reduce uncertainties associated with boundary conditions (see **Figure 4-7**). The screwed steel coupling that joined the shaker with the prototype has been replaced by a rotating platform to which the shaker is screwed.

The platform, attached with a car bearing to the upper part of the prototype, allows to vary the direction of application of the forces (see **Figure 4-8**).

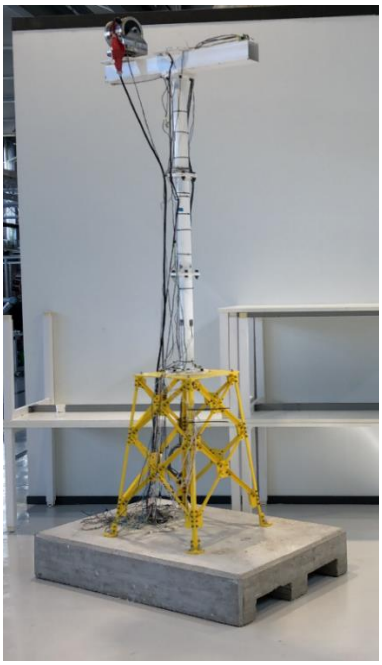

Figure 4-7 *OWT prototype fixed to a concrete block.*

Figure 4-8 *Rotating platform to which the shaker is currently screwed.*

4.2 *Prototype modelling*

A 3D CAD model of the scaled OWT prototype is created (see **Figure 4-9**). The model includes the jacket support structure, the tower, and the nacelle. The concrete block is not included in the CAD model. The assembly consisting of the shaker and the rotating base are simplified to a point mass, which has the same mass and mass center as the real assembly.

Figure 4-9 *CAD model of the scaled OWT prototype.*

A FEM model is generated from the CAD model (see **Figure 4-10**). A mesh of shell elements with quadratic order is used, with variable size depending on the part of the prototype. The tower is the part where the finest mesh is used, with an element size of 8mm. The main characteristics of the FEM model are collected in **Table 4-3**.

Feature	Value
Number of elements	11,400
Element type	Shell
Element order	Quadratic
Element size	Variable, 8mm in the tower
Contacts between parts	Bonded
Boundary conditions	4 fixed supports

Table 4-3 *Main characteristics of the generated FEM model.*

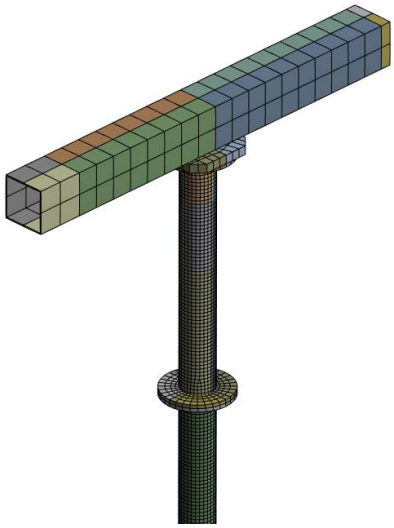

Figure 4-10 *Detailed view of the mesh.*

4.3 Sensors

To carry out the experiments performed with the study case 1, a set of strain gauges and accelerometers is installed in the OWT prototype to be used as input sensors for the later implemented VS algorithms, and as means of validation of the VS algorithms. The location of the sensors is chosen using the Modal Kinetic Energy (MKE) method [118], which helps to select the sensor positions based on the dynamics of the main modes. With the MKE, the sensors are placed where high signal amplitudes are expected, based on the modes excited during the operation of the monitored system.

In the tower, 10 strain gauges are installed in pairs at 5 different heights. At each height, a gauge aligned with X axis and a gauge aligned with Y axis are placed (see axes in **Figure 4-9**). All gauges are installed to measure normal strain in Z axis. The gauges are identified according to their alignment (X or Y), the height at which they are located (1, 2, 3…), and their orientation respect the plane XY (90º in all cases). The gauges at heights 1, 3, 4 and 5 are connected in quarter bridge configuration, while the gauges at height 2 are connected in Half Bridge (HB) configuration.

At one end of the nacelle (the opposite end to which the shaker is located), an accelerometer is installed. It is a MEMS triaxial accelerometer, capable of measuring both the static and dynamic response of the prototype in X, Y and Z directions. Moreover, on the rotating base that connects the shaker with the prototype, a potentiometer is installed for orientation measurement.

No sensor to measure the applied force has been installed in the OWT prototype. For this reason, only VS algorithms that do not require the use of signals from external forces as input will be implemented in this case study.

The position of the sensors on the OWT prototype can be seen in **Figure 4-11**. The number and specifications of the installed sensors are collected in **Table 4-4**. The height at which the different sensors are located is specified in **Table 4-5**.

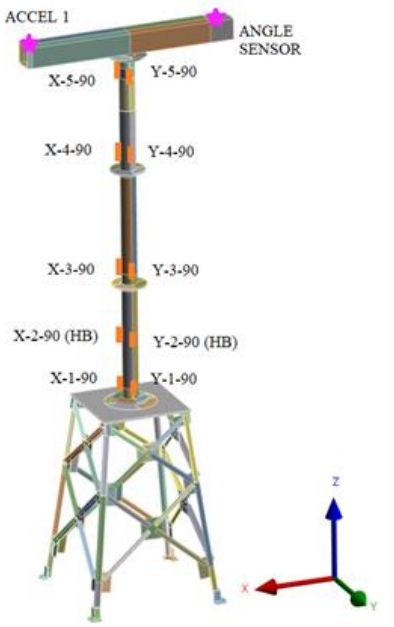

Figure 4-11 *Sensor location on the OWT prototype.*

Sensor	Number	Description
Strain gauges: quarter bridge	8	120 Ω, gauge factor = 2
Strain gauges: half bridge	2	120 Ω, gauge factor = 2 *
Accelerometer	1 (3 channels)	MEMS type (ADXL335)
Angle sensor	1	Potentiometer. 0-180º

**Each individual gauge.*

Table 4-4 *Number and specifications of the installed sensors*

Sensor	Height from top of the jacket	Height from ground
Gauges 1	58 mm	1358 mm
Gauges 2	308 mm	1608 mm
Gauges 3	620 mm	1920 mm
Gauges 4	1150 mm	2450 mm
Gauges 5	1610 mm	2910 mm
Accel. 1	1790 mm	3090 mm

Table 4-5 *Height of the installed sensors*

The data acquisition system used is made up of the software LabView of National Instruments (NI) and the hardware NI CompactDAQ-9189 (see **Figure 4-12**). Four modules NI-9235 have been used for reading the quarter bridge gauges, one NI-9237 for the half bridge gauges, one NI-9234 for the accelerometer and one NI-9201 for the angle sensor.

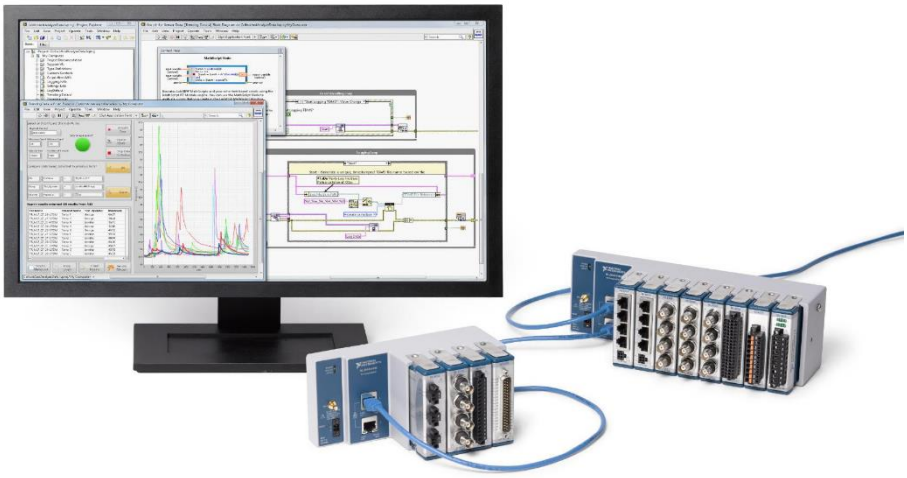

Figure 4-12 *PC with LabView installed next to two connected CompactDAQs. Source: https://www.ni.com*

4.4 Model checking.

In the experiments performed in this study case, dynamic loads are applied to the OWT prototype using the shaker attached to it. The frequencies of the applied loads are in the range of 2-25Hz. Due to this, before applying any VS approach, it is of interest to compare the behavior of the created FEM model with the behavior of the real prototype, both static and dynamic, in order to correlate the model.

For checking the static behavior of the model, the following procedure is followed: Two different static loads are applied to the nacelle of the OWT prototype, a 100N force along X axis, and a -100N force along Y axis (see **Figure 4-13**). These loads are applied manually, using a strap attached to the prototype and a spring dynamometer. The same loads are applied to the FEM model. The measurements obtained in the gauges of the real prototype are compared with the measurements obtained in the FEM model (see **Table 4-6**).

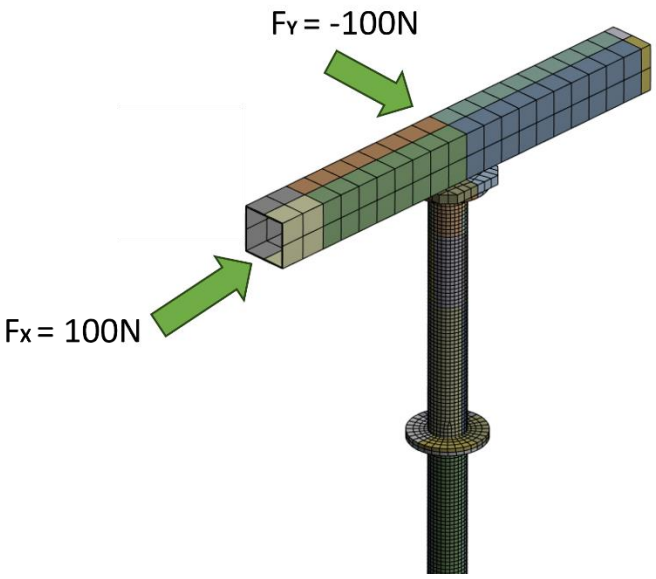

Figure 4-13 *Static loads applied to perform the checking of the static behavior of the model.*

Gauge	Force X: 100N		Force Y: -100N	
	Model	Real	Model	Real
X-1-90	101	92	-	-
Y-1-90	-	-	-101	-120
X-2-90 (HB)	172	160	-	-
Y-2-90 (HB)	-	-	-172	-168
X-3-90	70	72	-	-
Y-3-90	-	-	-70	-95
X-4-90	40	47	-	-
Y-4-90	-	-	-40	-55
X-5-90	16	11	-	-
Y-5-90	-	-	-16	-16

Table 4-6 *Comparison between measured strain in the FEM model and in the real prototype, with static loads applied.*

A certain deviation can be observed between the strain values obtained with the FEM model and the strains measured in the real prototype. These deviations can be partly explained by the uncertainty associated with the way in which the loads have been applied.

For checking the dynamic behavior of the model, an Operational Modal Analysis (OMA) is performed with the OWT prototype, using two B&K 4501A piezoelectric accelerometers installed for the occasion and the data-acquisition software PULSE. With the shaker off, the OWT prototype is excited by impacts in X and Y directions made manually using a special hammer.

In the performed OMA, the first 4 modes of the prototype are identified (those 4 that are within the working frequency range: 0 to 25Hz). Later, a modal analysis is

performed with the FEM model, and the first 4 modes of the model are compared with the 4 first modes identified in the real prototype. The modes are compared both in frequency and using MAC correlation, the results of this comparison can be seen in **Table 4-7**. The first 4 modal shapes obtained with the modal analysis performed with the model can be seen in **Figure 4-14**.

From the OMA performed to the OWT prototype, the damping ratios associated with each mode are also obtained (which can be seen in **Table 4-7**).

Mode	Mode description	Freq. (FEM model)	Freq. (real prototype)	MAC	Damping ratio
1	1st in X. Bending	3.1 Hz	3.1 Hz	85 %	0.5 %
2	1st in Y. Bending	3.1 Hz	3.1 Hz	93 %	0.7 %
3	2nd in X. Bending	17.0 Hz	16.2 Hz	86 %	4.1 %
4	1st in Z. Torsion	19.2 Hz	17.4 Hz	99 %	2.7 %

Table 4-7 *Modal comparison between the FEM model and the real prototype.*

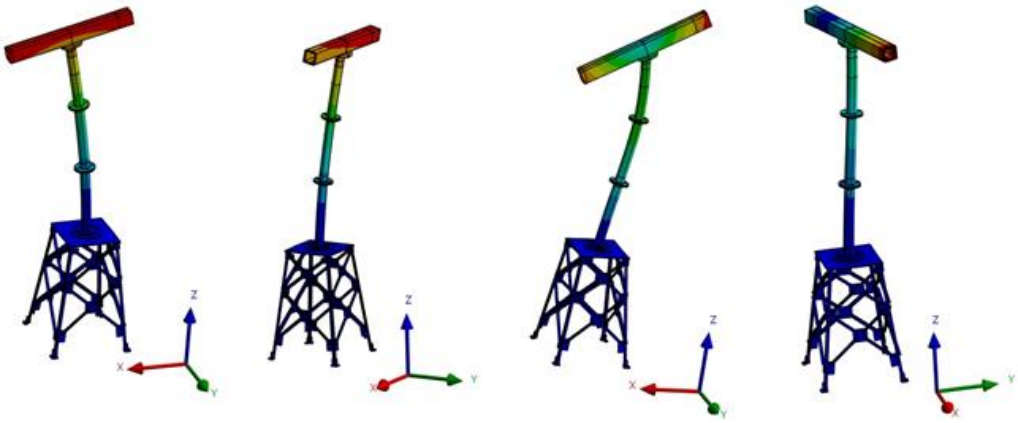

Figure 4-14 *First 4 modal shapes of the OWT prototype (from left to right).*

In the comparison between the modal behavior of the FEM model and the results of the performed OMA to the real prototype, it is verified that the first 4 modes detected in the prototype coincide with the first 4 modes of the model. The 4 detected modes have good MAC correlation values with the modes of the model, in all cases above 85%. The frequencies of these modes also coincide, with a maximum relative error of 10%.

4.4 Expected uncertainties

In the experiment carried out on this study case, different uncertainties are expected, that are listed and commented in this subchapter.

In first place, the uncertainties due to the characteristics of the structure may cause certain behavior differences between the real prototype and the FEM model. Probably, the major source of uncertainty are the joints between the different parts of the prototype, mainly the screwed plates between tower segments and the bearing that joins the shaker to the nacelle (see **Figure 4-8**), because they affect the overall stiffness of the prototype.

Boundary conditions are generally an important source of uncertainty in this type of experiments. In this case, due to the incorporation of a fixed support on a large concrete base (see **Figure 4-7**), it is considered that this source of uncertainty is significantly reduced.

Possible errors in the installation of the strain gauges and accelerometers, both in the exact position of the sensors and in their orientation, can also imply certain degree of uncertainty in the obtained strain measurements.

The uncertainty associated with each sensor is characterized by its intrinsic noise level, representing the undesired signal present even in the absence of a measured signal. This level of uncertainty has been measured as 0.3 μm/m in the case of the strain gauges, and in 0.01 m/s^2 in the case of the accelerometer.

4.5 Implemented VS algorithms and sensor configurations

In the study case 1, three VS algorithms are implemented: the KF, the AKF and the LSSE.

A total of 10 gauges (grouped in pairs) and a triaxial accelerometer (with 3 channels) are the available sensors installed on the OWT prototype. There is no sensor to measure the external loads applied to the prototype, so only VS algorithms in which knowing the loads on the system is not required are implemented.

In the experiments carried out in this study case, the objective of the virtual sensing is to estimate strain measurements at non-sensorized points. For this purpose, some points are selected in the OWT prototype, in which the virtual strain sensors are implemented. In these selected points there are real strain gauges installed, but their purpose is not to feed the VS algorithms with real data, but to provide reference real data to compare with the virtual strain estimations. With this method, it is possible to evaluate the performance of the implemented VS algorithms.

For the implementation of the selected VS algorithms, first a reduced model is extracted from the FEM model using modal truncation. To carry out this reduction method, the criteria mentioned in *subchapter 2.4* is applied. The reduced model includes the first 4 modes of the OWT prototype (see **Table 4-7**), which are all the modes found in the frequency range of the performed experiments (0 to 25Hz) and equate more than 90% of the modal mass.

From a modal analysis performed with the FEM model, a **G** strain matrix is also obtained (see equation 2-39). This matrix relates the strain at the points of the prototype sensorized with gauges, with the modal displacements of each mode kept in the reduced model.

In order to find the most efficient sensor configurations (i.e., those sensor configurations that, using the minimum number of input sensors, are capable of

providing reliable virtual measurements at points of interest), different sensor configurations are tested in each of the selected VS algorithms. All configurations include strain gauges (which are always incorporated in "X and Y" pairs), being optional the incorporation of acceleration measurements. It is intended to maintain the observability (or equivalent condition) of the VS algorithms in each proposed sensor configuration. 12 different sensor configurations are tested in total, which can be seen in **Table 4-8**.

In all tested configurations, the virtual strain sensors are located at the points where the 1-X-90 and 1-Y-90 gauges are located. These points have been chosen to be monitored because, being at the base of the tower, it is where the greatest stresses are expected. Furthermore, in a real offshore wind turbine application, that would be the point closest to the sea surface (see **Figure 4-15**), and therefore, the points most exposed to harsh marine conditions (where it would be more unfeasible to install real sensors).

Figure 4-15 *Close view of the jacket support structure of an OWT* [119]

Algorithms	Config. number	Ac X	Ac Y	Ac Z	G2	G3	G4	G5
KF, AKF, LSSE	1				x	x	x	x
KF, AKF, LSSE	2				x	x	x	
KF, AKF, LSSE	3					x	x	x
KF, AKF, LSSE	4				x	x		
KF, AKF, LSSE	5						x	x
KF, AKF	6	x	x	x	x	x	x	x
KF, AKF	7	x	x	x	x	x	x	
KF, AKF	8	x	x	x		x	x	x
KF, AKF	9	x	x	x	x	x		
KF, AKF	10	x	x	x			x	x
KF, AKF	11	x	x	x	x			
KF, AKF	12	x	x	x				x

Table 4-8 *Sensor configurations tested. The "G" columns indicate the pairs of strain gauges (for example, G2 stands for the X-2-90 and Y-2-90 gauges). The "Ac" columns indicate the different channels of the accelerometer used (X, Y and Z).*

In the case of the KF, as load measurements are not available, the formulation without matrix **B** is used (see equation 2-60). The value of Q is adjusted for each sensor configuration through an iterative process, discussed later.

In the case of the AKF, external load measurements are not a necessary input, so it is not necessary to alter the original formulation of the filter. But, since there are no load measurements to use as reference data, in this thesis the AKF is not used to estimate unmeasured loads. As in the KF, the value of parameters Q and Q_u are adjusted for each sensor configuration through an iterative process.

Study case 1

In the case of the LSSE, only sensor configurations that contain strain gauges are used, because this algorithm only accepts this type of input data. This algorithm does not have adjustment parameters.

Before being introduced into the VS algorithms, sensor data is filtered using a low-pass Butterworth filter at 26 Hz, with the aim of avoiding introducing undesired disturbances. This value is chosen because the highest frequency present in the applied input loads is 25 Hz.

4.5 Performed experiments

In this study case, different dynamical external forces are applied to the OWT prototype, with the aim of testing the VS selected algorithms under different circumstances. Thanks to the shaker installed on the top of the prototype using a rotating base, it is possible to apply dynamic forces of different types and frequencies, also varying their direction. A rubber hammer is also used to apply certain types of excitations (impacts) to the prototype. All dynamic forces generated with the shaker are applied in X direction, Y direction, XY direction (45º respect X axis) and VAR (variable, where the shaker is rotated randomly during the experiment). Hammer impacts are applied in X and Y directions. All applied forces are explained in **Table 4-9**.

Input Force Type	Frequency [Hz]	Directions
0 mean sinusoidal	2	X, Y, XY
0 mean sinusoidal	5	X, Y, XY, VAR
0 mean sinusoidal	10	X, Y, XY
0 mean sinusoidal	15	X, Y, XY, VAR
0 mean white noise	5-25	X, Y, XY
Hammer impacts	-	X, Y

Table 4-9 *External forces applied in the performed tests.*

4.6 Kalman filters adjustment

Kalman filters and their variants, as explained in Chapter 2, contain adjustment parameters that affect its operation. These parameters are the values of Q and R, corresponding to the diagonal values of the covariance matrices **Q** (see equation 2-51) and **R** (see equation 2-52). In the case of the AKF, the parameter Q_u must also be taken into account, corresponding to the zero-mean random walk model, with which the unmeasured external forces are estimated.

R values are set based on the uncertainty attributed to each type of sensor (the values can be seen in **Table 4-10**). R values, determined by analyzing the variance of the background noise of the signal sensors, are kept constant for all sensor configurations tested.

Sensor	R value
Gauges	1×10^{-8}
Accelerometers	1×10^{-3}

Table 4-10 *R values for the used sensors*

Q values are adjusted for each sensor configuration using the following strategy. Virtual strain measurements are obtained at points of the OWT prototype where input strain gauges are located (in each sensor configuration). An iterative process is performed for each sensor configuration, in which KF and AKF algorithms are tested with different values of Q in a range from $Q=10^{-20}$ to $Q=10^{0}$ (in logarithmic steps of 10^{-1}), looking for the Q values that minimize the error between the estimates and the real measurements at measured points. For this strategy, the white noise applied in XY direction is used as applied external force (see **Table 4-9**). In the case of the AKF, the Q_u value is fixed in 1×10^{3}.

This strategy can be useful to allow the Kalman filters to self-adjust to their optimal configuration in final applications, where equivalent real measurements are not available in the virtual sensing points (in order to check its performance).

In **Table 4-11** the optimal values of Q for the KF found through the iterative process described are shown. The convergence to a minimum of the percent errors of the virtual strain estimations (obtained at the points where input sensors are installed) is used for this purpose. **Figure 4-16** and **Figure 4-17** show two examples (with only strain gauges as input sensors) where the optimal value of Q converges to 1. **Figure 4-18** and **Figure 4-19** show two examples (with strain gauges and accelerometers as input sensors) where the optimal value of Q converges between 1×10^{-12} and 1×10^{-14}.

Algorithm	Config. number	Optimal Q value according to…				Optimal Q value
		G2	G3	G4	G5	
KF	1	1×10^{0}	1×10^{0}	1×10^{0}	1×10^{-1}	1×10^{0}
KF	2	1×10^{0}	1×10^{0}	1×10^{0}	-	1×10^{0}
KF	3	-	1×10^{-2}	1×10^{0}	1×10^{-2}	1×10^{-2}
KF	4	1×10^{0}	1×10^{0}	-	-	1×10^{0}
KF	5	-	-	1×10^{0}	1×10^{0}	1×10^{0}
KF	6	1×10^{-14}	1×10^{-13}	1×10^{-12}	1×10^{-13}	1×10^{-13}
KF	7	1×10^{-14}	1×10^{-13}	1×10^{-12}	-	1×10^{-13}
KF	8	-	1×10^{-13}	1×10^{-12}	1×10^{-13}	1×10^{-13}
KF	9	1×10^{-14}	1×10^{-13}	-	-	1×10^{-13}
KF	10	-	-	1×10^{-12}	1×10^{-13}	1×10^{-13}
KF	11	1×10^{-14}	-	-	-	1×10^{-14}
KF	12	-	-	-	1×10^{-14}	1×10^{-14}

Table 4-11 *Optimal Q values for each sensor configuration defined in the KF. The optimal Q value is shown according to each input gauge of the configuration, and the optimal Q value finally selected for that configuration. The "G" columns indicate the pairs of strain gauges (for example, G2 stands for the 2-X-90 and 2-Y-90 gauges).*

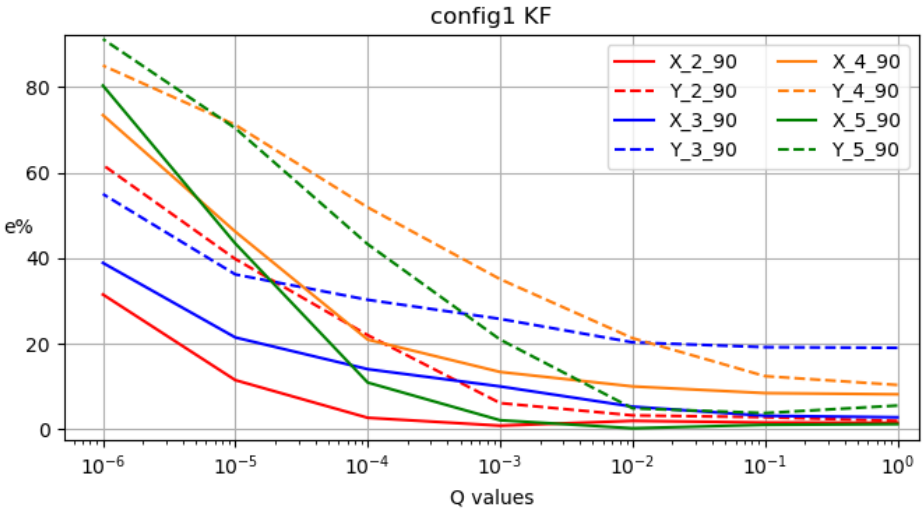

Figure 4-16 *Plot showing the optimal Q value for sensor configuration 1 using the KF. The convergence to a minimum of the percent errors is shown, using virtual strain estimations obtained at the points where input sensors are installed.*

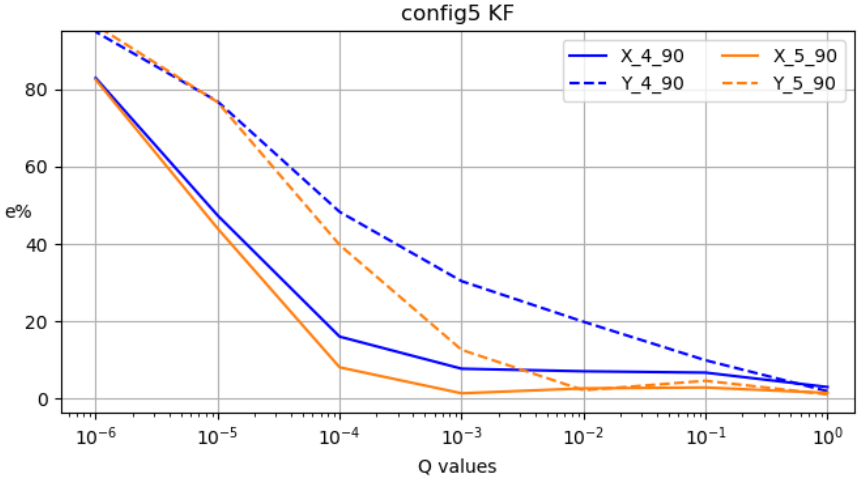

Figure 4-17 *Plot showing the optimal Q for sensor configuration 5 using the KF. The convergence to a minimum of the percent error is shown, using virtual strain estimations obtained at the points where input sensors are installed.*

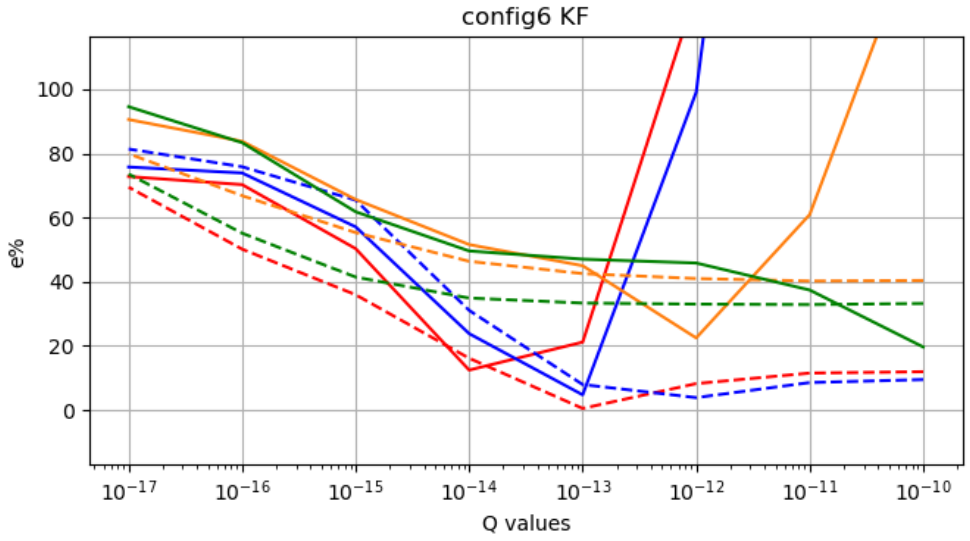

Figure 4-18 *Plot showing the optimal Q for sensor configuration 6 using the KF. The convergence to a minimum of the percent error is shown, using virtual strain estimations obtained at the points where input sensors are installed.*

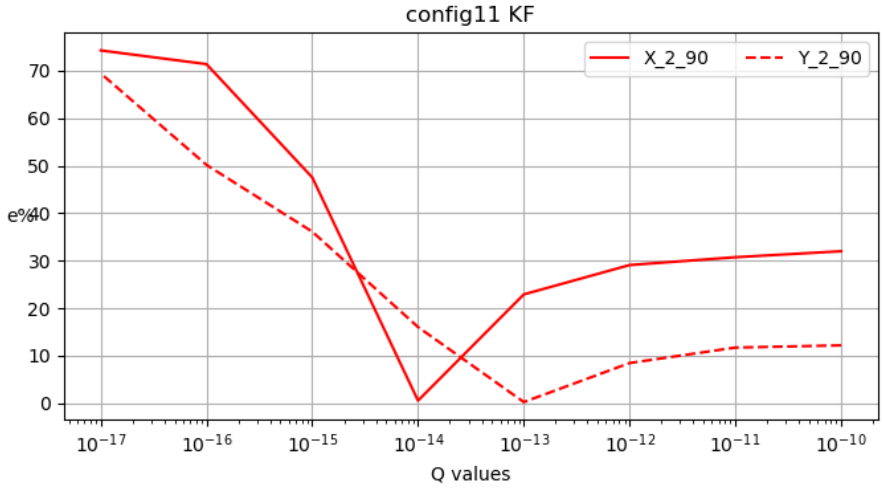

Figure 4-19 *Plot showing the optimal Q for sensor configuration 11 using the KF. The convergence to a minimum of the percent error is shown, using virtual strain estimations obtained at the points where input sensors are installed.*

In **Table 4-12** the optimal values of Q for the AKF found through the iterative process described are shown. **Figure 4-20** and **Figure 4-21** show two examples (with only strain gauges as input sensors) in which the optimal value of Q converges to 1. **Figure 4-22** shows an example (with strain gauges and accelerometers as input sensors) in which the optimal value of Q converges between 1×10^{-12} and 1×10^{-14}. **Figure 4-23** shows an example (also with strain gauges and accelerometers as input sensors) in which no clear convergence is observed.

Algorithm	Config. number	Q_u	Optimal Q value according to…				Optimal Q value
			G2	G3	G4	G5	
AKF	1	1×10^{3}	1×10^{0}	1×10^{0}	1×10^{0}	1×10^{-2}	1×10^{0}
AKF	2	1×10^{3}	1×10^{0}	1×10^{0}	1×10^{0}	-	1×10^{0}
AKF	3	1×10^{3}	-	1×10^{-2}	1×10^{0}	1×10^{-2}	1×10^{-2}
AKF	4	1×10^{3}	1×10^{0}	1×10^{0}	-	-	1×10^{0}
AKF	5	1×10^{3}	-	-	1×10^{0}	1×10^{0}	1×10^{0}
AKF	6	1×10^{3}	1×10^{0}	1×10^{0}	1×10^{0}	1×10^{0}	1×10^{0}
AKF	7	1×10^{3}	1×10^{0}	1×10^{0}	1×10^{0}	-	1×10^{0}
AKF	8	1×10^{3}	-	1×10^{-1}	1×10^{0}	1×10^{-2}	1×10^{-1}
AKF	9	1×10^{3}	1×10^{0}	1×10^{0}	-	-	1×10^{0}
AKF	10	1×10^{3}	-	-	1×10^{0}	1×10^{0}	1×10^{0}
AKF	11	1×10^{3}	1×10^{-1}	-	-	-	1×10^{-1}
AKF	12	1×10^{3}	-	-	-	1×10^{0}	1×10^{0}

Table 4-12 *Optimal Q values for each sensor configuration defined in the AKF. Is shown the optimal Q value according to each input gauge of the configuration, and the optimal Q value finally selected for that configuration. The "G" columns indicate the pairs of strain gauges (for example, G2 stands for the 2-X-90 and 2-Y-90 gauges).*

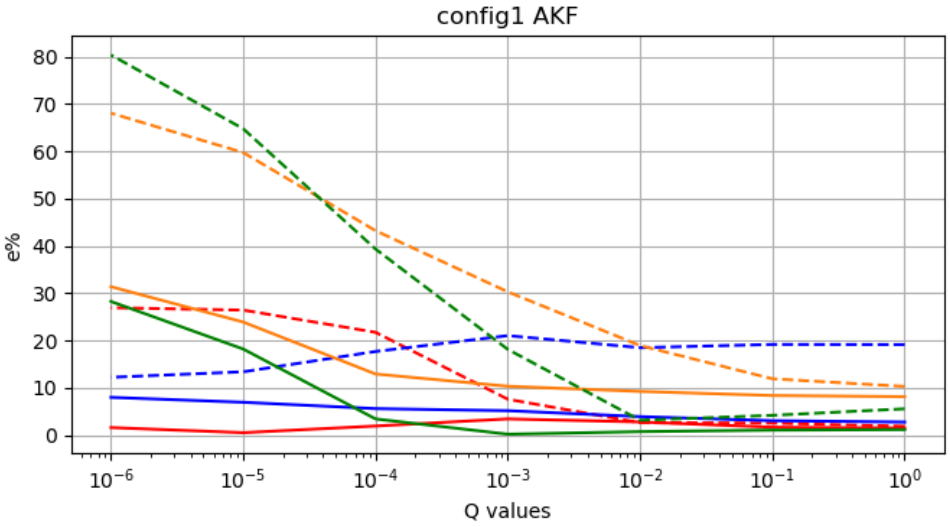

Figure 4-20 *Plot showing the optimal Q for sensor configuration 1 using the AKF. The convergence to a minimum of the percent error is shown, using virtual strain estimations obtained at the points where input sensors are installed.*

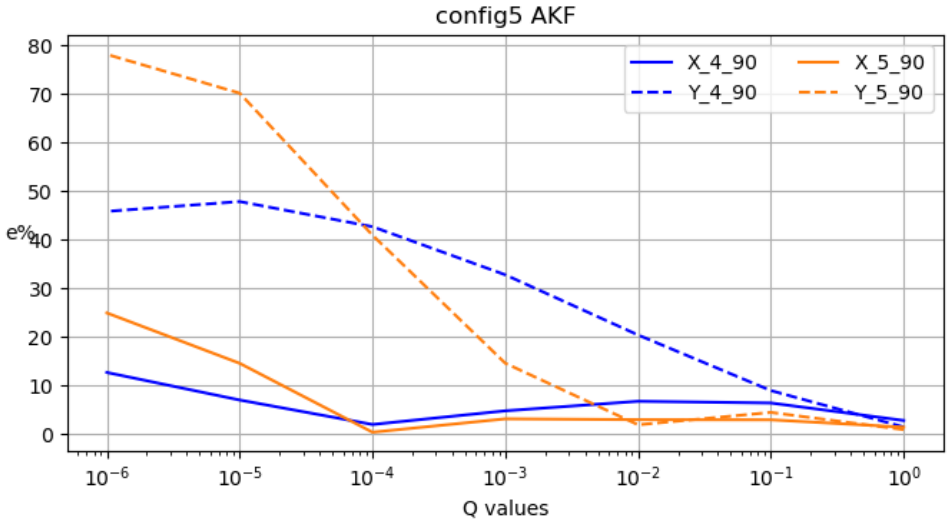

Figure 4-21 *Plot showing the optimal Q for sensor configuration 5 using the AKF. The convergence to a minimum of the percent error is shown, using virtual strain estimations obtained at the points where input sensors are installed.*

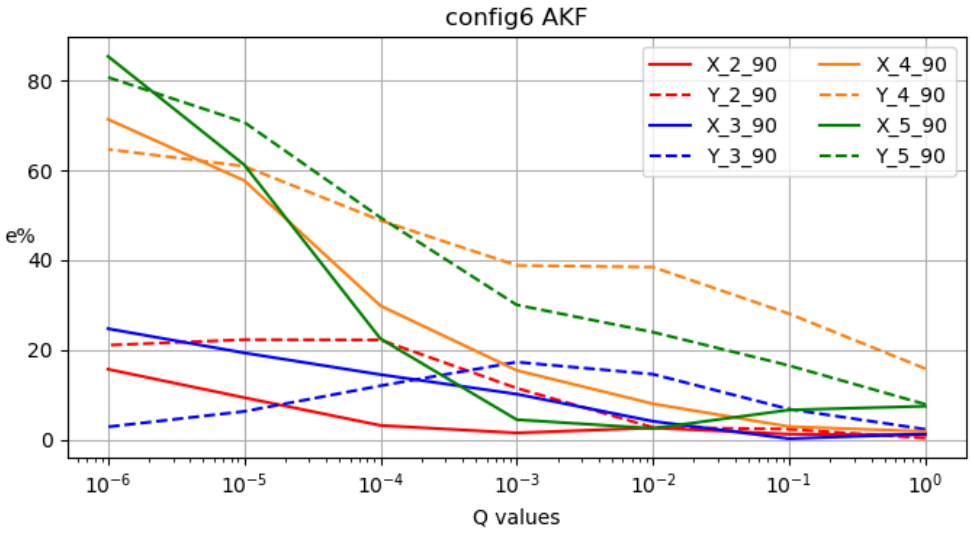

Figure 4-22 *Plot showing the optimal Q for sensor configuration 6 using the AKF. The convergence to a minimum of the percent error is shown, using virtual strain estimations obtained at the points where input sensors are installed.*

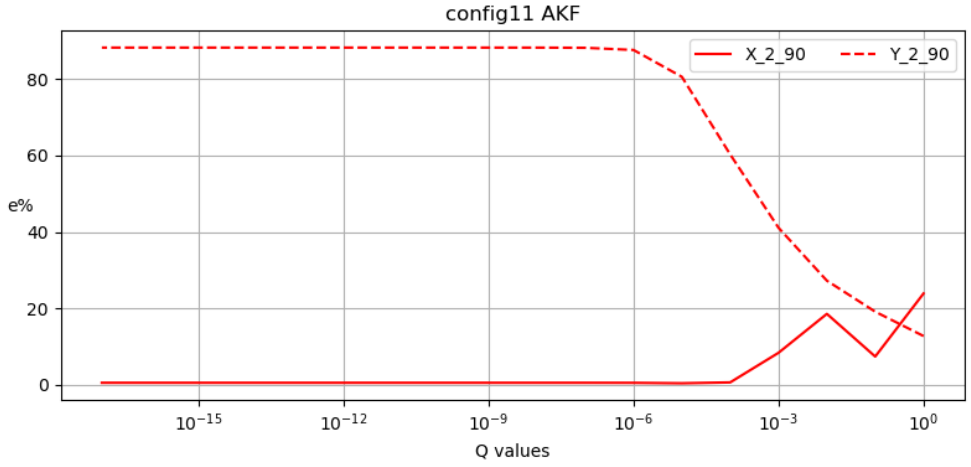

Figure 4-23 *Plot showing the optimal Q for sensor configuration 11 using the AKF. The convergence to a minimum of the percent error is shown, using virtual strain estimations obtained at the points where input sensors are installed.*

4.7 Results

In this subchapter the virtual sensing results obtained with the different VS algorithms tested (KF, AKF and LSSE) are shown, using the described sensor configurations (see **Table 4-8**) and applying the described external forces (see **Table 4-9**). The results are evaluated using several indicators proposed in *2.13* Evaluation indicators.

In the tested sensor configurations, the virtual sensors are implemented in the positions of the strain gauges X-1-90 and Y-1-90 (measurement data obtained from them being used as reference data). Virtual strain measurements at X-1-90 are evaluated when forces in X direction are applied, and virtual strain measurements at Y-1-90 are evaluated when forces in Y direction are applied. Both measurements at X-1-90 and Y-1-90 are evaluated when external forces affecting both directions are applied. For the evaluation of the obtained results, the percent error (see equation 2-85) and the PCC (see equation 2-84) are used. For each sensor configuration, the results obtained with each input force applied are first individually evaluated and then summarized using the mean. In the evaluation of the obtained virtual measurements, a percent error below 20% and a PCC over 0.9 is considered satisfactory.

Due to the large amount of data obtained from the different experiments carried out, the results are organized into two sections, each containing multiple tables and images.

In the first section, the results obtained with the KF, AKF and LSSE using sensor configurations 1 to 5 (which only use strain gauges as input sensors) are shown in **Table 4-13**, **Table 4-14**, **Table 4-15** and **Table 4-16**, respectively.

In the second section, the results obtained with the KF and AKF using sensor configurations 6 to 12 (which use strain gauges and accelerometers as input sensors) are shown in **Table 4-17**, **Table 4-18**, **Table 4-19**, **Table 4-20**.

In both sections is shown a plot repertoire of some of the results obtained.

VS algorithm:			KF		AKF		LSSE	
Sensor config.	**External force**	**Virtual sensor**	**e%**	**PCC**	**e%**	**PCC**	**e%**	**PCC**
1	X dir. Noise	X-1-90	8.78	0.99	8.75	0.99	8.83	0.99
1	X dir. Sin 10Hz	X-1-90	10.26	0.99	10.15	0.99	10.30	0.99
1	X dir. Sin 15Hz	X-1-90	15.19	1.00	15.08	1.00	15.13	1.00
1	X dir. Sin 2Hz	X-1-90	9.48	1.00	9.65	1.00	9.51	1.00
1	X dir. Sin 5Hz	X-1-90	11.58	1.00	11.45	1.00	11.58	1.00
1	**Summary**		**11.06**	**1.00**	**11.01**	**1.00**	**11.07**	**0.99**
2	X dir. Noise	X-1-90	4.36	0.98	4.32	0.98	4.40	0.98
2	X dir. Sin 10Hz	X-1-90	8.99	0.99	8.91	0.99	9.02	0.99
2	X dir. Sin 15Hz	X-1-90	12.34	1.00	12.26	1.00	12.30	1.00
2	X dir. Sin 2Hz	X-1-90	13.58	1.00	13.52	1.00	13.81	1.00
2	X dir. Sin 5Hz	X-1-90	14.90	1.00	14.78	1.00	14.92	1.00
2	**Summary**		**10.83**	**0.99**	**10.76**	**0.99**	**10.89**	**0.99**
3	X dir. Noise	X-1-90	10.28	0.88	8.32	0.89	9.60	0.99
3	X dir. Sin 10Hz	X-1-90	12.56	0.82	1.03	0.86	4.60	1.00
3	X dir. Sin 15Hz	X-1-90	43.53	0.98	34.36	0.97	13.94	1.00
3	X dir. Sin 2Hz	X-1-90	9.55	0.98	2.24	0.99	8.61	1.00
3	X dir. Sin 5Hz	X-1-90	0.03	0.96	20.27	0.97	4.12	1.00
3	**Summary**		**15.19**	**0.92**	**13.24**	**0.94**	**8.18**	**1.00**
4	X dir. Noise	X-1-90	11.19	0.98	11.16	0.98	11.29	0.98
4	X dir. Sin 10Hz	X-1-90	14.34	0.99	14.38	0.99	14.33	0.99
4	X dir. Sin 15Hz	X-1-90	18.01	1.00	18.07	1.00	18.07	1.00

VS algorithm:			KF		AKF		LSSE	
Sensor config.	**External force**	**Virtual sensor**	**e%**	**PCC**	**e%**	**PCC**	**e%**	**PCC**
4	X dir. Sin 2Hz	X-1-90	14.90	0.99	14.28	0.99	16.67	1.00
4	X dir. Sin 5Hz	X-1-90	17.80	1.00	17.74	1.00	18.10	1.00
4	**Summary**		**15.25**	**0.99**	**15.12**	**0.99**	**15.69**	**0.99**
5	X dir. Noise	X-1-90	33.68	0.59	31.38	0.57	35.49	0.43
5	X dir. Sin 10Hz	X-1-90	13.08	0.85	10.63	0.84	13.72	0.81
5	X dir. Sin 15Hz	X-1-90	63.38	0.99	63.10	0.99	63.57	0.98
5	X dir. Sin 2Hz	X-1-90	41.89	0.99	37.91	0.99	42.21	0.99
5	X dir. Sin 5Hz	X-1-90	26.03	0.99	28.61	0.99	26.90	0.99
5	**Summary**		**35.61**	**0.88**	**34.33**	**0.88**	**36.38**	**0.84**

Table 4-13 *Results obtained with sensor configurations 1 to 5 (only strain gauges are used as input sensors). External forces applied in X direction.*

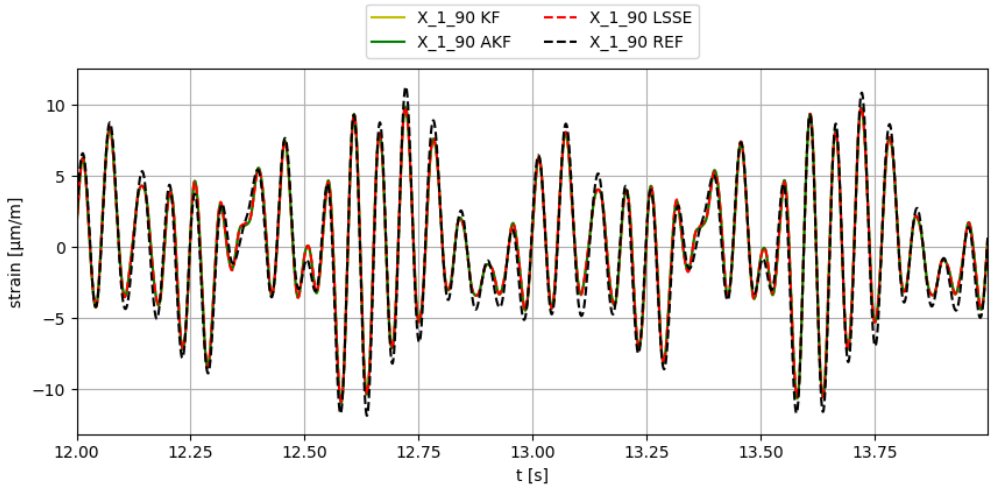

Figure 4-24 *Plot of results obtained at gauge X-1-90 using sensor config. 1, applying white noise force in X direction.*

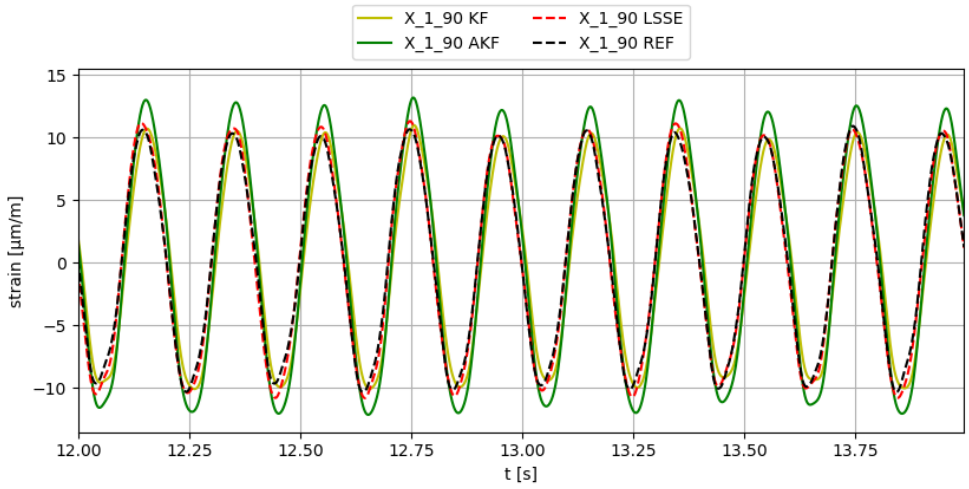

Figure 4-25 *Plot of results obtained at gauge X-1-90 using sensor config. 3, applying sin 5Hz force in X direction.*

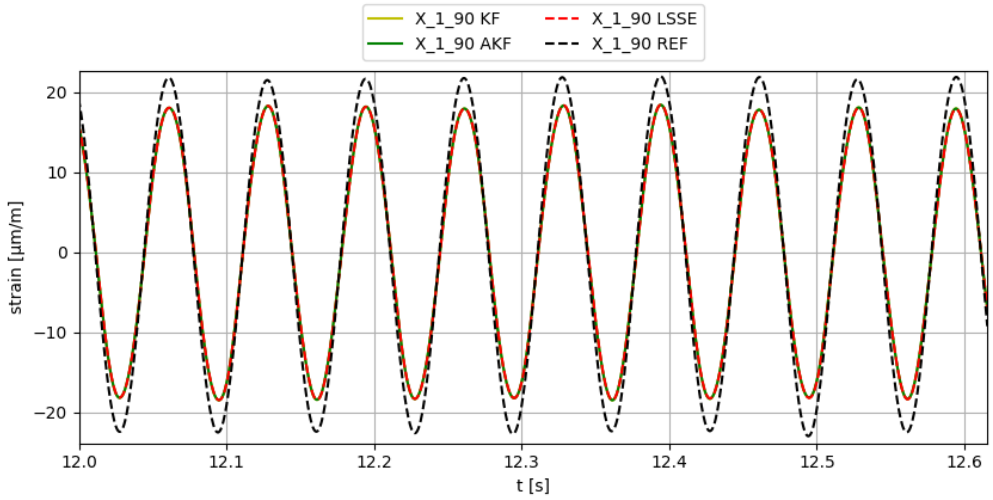

Figure 4-26 *Plot of results obtained at gauge X-1-90 using sensor config. 4, applying sin 15Hz force in X direction.*

Study case 1

VS algorithm:			KF		AKF		LSSE	
Sensor config.	**External force**	**Virtual sensor**	**e%**	**PCC**	**e%**	**PCC**	**e%**	**PCC**
1	Y dir. Noise	Y-1-90	18.39	1.00	18.39	1.00	18.34	1.00
1	Y dir. Sin 10Hz	Y-1-90	19.04	1.00	19.03	1.00	18.98	1.00
1	Y dir. Sin 15Hz	Y-1-90	17.97	1.00	17.97	1.00	17.92	1.00
1	Y dir. Sin 2Hz	Y-1-90	22.71	1.00	22.75	1.00	23.69	1.00
1	Y dir. Sin 5Hz	Y-1-90	21.58	1.00	21.57	1.00	21.65	1.00
1	**Summary**		**19.94**	**1.00**	**19.94**	**1.00**	**20.12**	**1.00**
2	Y dir. Noise	Y-1-90	17.01	1.00	17.02	1.00	16.96	1.00
2	Y dir. Sin 10Hz	Y-1-90	20.87	1.00	20.92	1.00	20.82	1.00
2	Y dir. Sin 15Hz	Y-1-90	15.73	1.00	15.73	1.00	15.63	1.00
2	Y dir. Sin 2Hz	Y-1-90	25.64	1.00	25.44	1.00	28.45	1.00
2	Y dir. Sin 5Hz	Y-1-90	25.49	1.00	25.53	1.00	25.87	1.00
2	**Summary**		**20.95**	**1.00**	**20.93**	**1.00**	**21.54**	**1.00**
3	Y dir. Noise	Y-1-90	17.73	0.99	15.42	0.99	4.30	0.99
3	Y dir. Sin 10Hz	Y-1-90	40.40	0.99	29.47	1.00	4.16	1.00
3	Y dir. Sin 15Hz	Y-1-90	12.38	1.00	10.84	1.00	6.91	1.00
3	Y dir. Sin 2Hz	Y-1-90	8.91	0.99	4.10	1.00	5.37	1.00
3	Y dir. Sin 5Hz	Y-1-90	6.47	0.98	9.65	0.99	6.85	1.00
3	**Summary**		**17.18**	**0.99**	**13.90**	**0.99**	**5.52**	**1.00**
4	Y dir. Noise	Y-1-90	24.28	1.00	24.38	1.00	24.51	1.00
4	Y dir. Sin 10Hz	Y-1-90	30.09	1.00	30.42	1.00	30.54	1.00
4	Y dir. Sin 15Hz	Y-1-90	22.88	1.00	22.94	1.00	22.75	1.00

VS algorithm:			KF		AKF		LSSE	
Sensor config.	**External force**	**Virtual sensor**	**e%**	**PCC**	**e%**	**PCC**	**e%**	**PCC**
4	Y dir. Sin 2Hz	Y-1-90	27.43	0.99	26.91	0.99	38.45	0.99
4	Y dir. Sin 5Hz	Y-1-90	32.60	1.00	32.89	1.00	36.36	1.00
4	**Summary**		**27.46**	**1.00**	**27.51**	**1.00**	**30.52**	**1.00**
5	Y dir. Noise	Y-1-90	25.96	0.94	25.78	0.94	29.84	0.90
5	Y dir. Sin 10Hz	Y-1-90	3.05	0.99	0.92	0.99	0.57	0.99
5	Y dir. Sin 15Hz	Y-1-90	36.58	1.00	37.00	0.99	45.57	1.00
5	Y dir. Sin 2Hz	Y-1-90	29.41	0.99	23.83	0.99	30.30	0.98
5	Y dir. Sin 5Hz	Y-1-90	20.41	0.99	23.54	0.99	23.66	0.99
5	**Summary**		**23.08**	**0.98**	**22.21**	**0.98**	**25.99**	**0.97**

Table 4-14 *Results obtained with sensor configurations 1 to 5 (only strain gauges are used as input sensors). External forces applied in Y direction.*

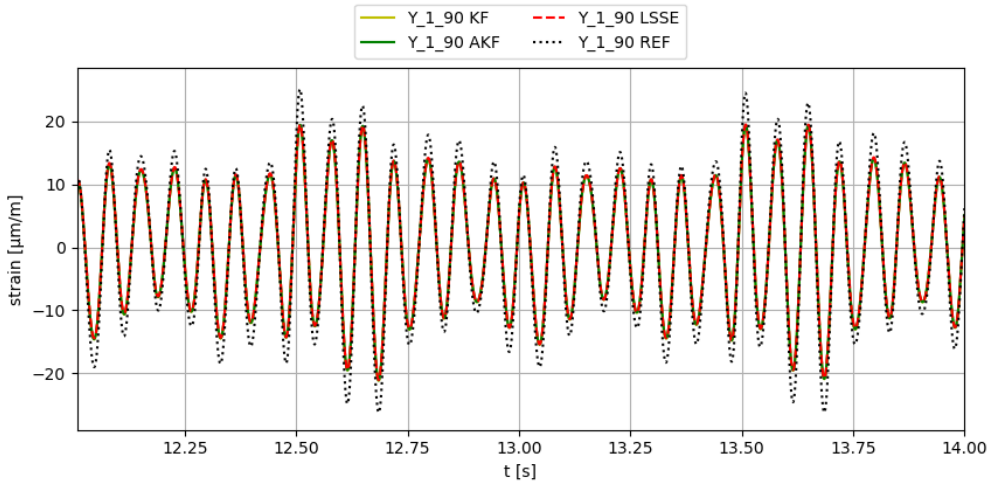

Figure 4-27 *Plot of results obtained at gauge Y-1-90 using sensor config. 1, applying white noise force in Y direction.*

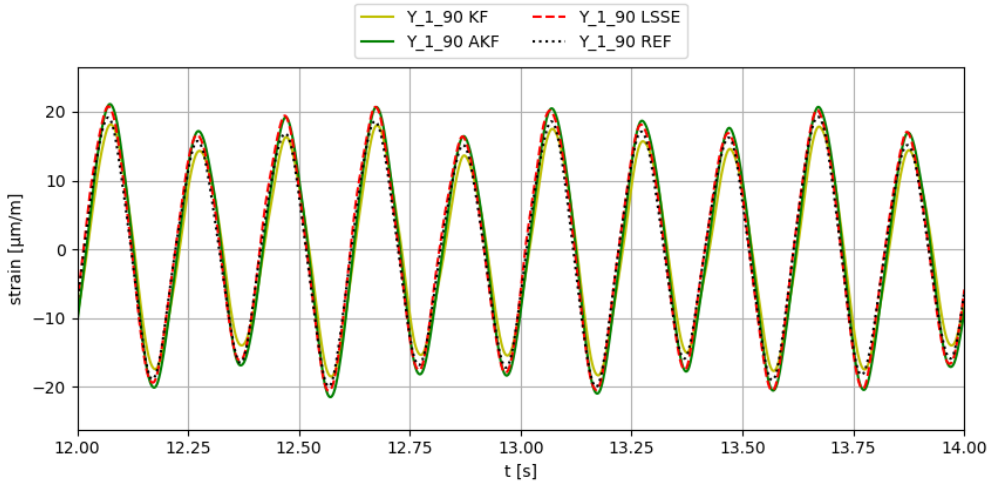

Figure 4-28 *Plot of results obtained at gauge Y-1-90 using sensor config. 3, applying sin 5Hz force in Y direction.*

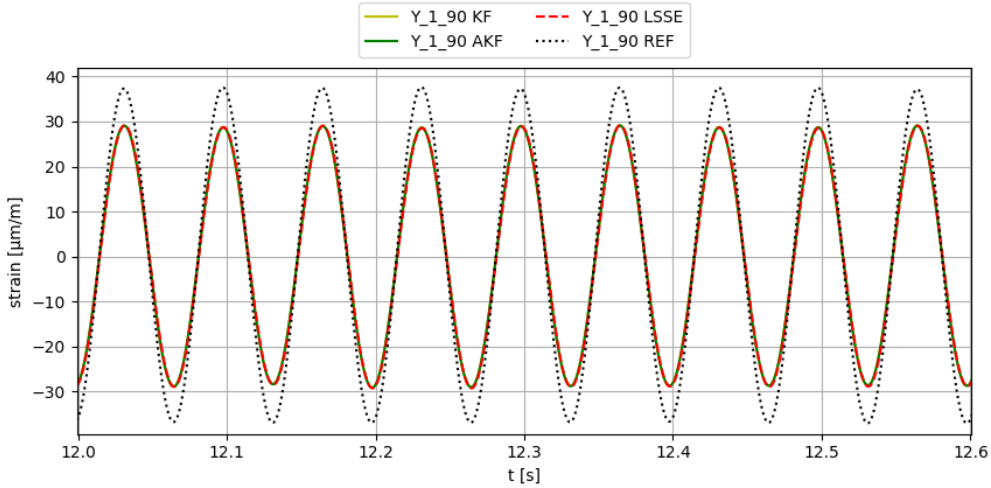

Figure 4-29 *Plot of results obtained at gauge Y-1-90 using sensor config. 4, applying white sin15Hz force in Y direction.*

VS algorithm:			KF		AKF		LSSE	
Sensor config.	**External force**	**Virtual sensor**	**e%**	**PCC**	**e%**	**PCC**	**e%**	**PCC**
1	XY dir. Noise	X-1-90	0.18	0.99	0.19	0.99	0.16	0.99
1	XY dir. Noise	Y-1-90	26.54	0.99	26.54	0.99	26.60	0.99
1	XY dir. Sin 10Hz	X-1-90	4.93	1.00	5.09	1.00	4.92	1.00
1	XY dir. Sin 10Hz	Y-1-90	26.59	1.00	26.58	1.00	26.55	1.00
1	XY dir. Sin 15Hz	X-1-90	15.12	1.00	15.30	1.00	15.30	1.00
1	XY dir. Sin 15Hz	Y-1-90	21.52	1.00	21.52	1.00	21.47	1.00
1	XY dir. Sin 2Hz	X-1-90	2.77	1.00	2.70	1.00	2.74	1.00
1	XY dir. Sin 2Hz	Y-1-90	37.76	1.00	37.77	1.00	38.48	1.00
1	XY dir. Sin 5Hz	X-1-90	5.67	1.00	5.82	1.00	5.68	1.00
1	XY dir. Sin 5Hz	Y-1-90	32.90	1.00	32.89	1.00	33.01	1.00
1	**Summary**		**17.40**	**1.00**	**17.44**	**1.00**	**17.49**	**1.00**
2	XY dir. Noise	X-1-90	0.92	0.98	0.84	0.98	1.02	0.98
2	XY dir. Noise	Y-1-90	24.98	0.99	24.95	0.99	25.18	0.99
2	XY dir. Sin 10Hz	X-1-90	9.18	0.99	9.28	0.99	9.17	0.99
2	XY dir. Sin 10Hz	Y-1-90	28.06	0.99	28.10	0.99	28.01	0.99
2	XY dir. Sin 15Hz	X-1-90	40.90	1.00	41.02	1.00	41.02	1.00
2	XY dir. Sin 15Hz	Y-1-90	18.55	1.00	18.55	1.00	18.45	1.00
2	XY dir. Sin 2Hz	X-1-90	2.22	1.00	2.13	1.00	2.43	1.00
2	XY dir. Sin 2Hz	Y-1-90	42.21	0.99	42.04	0.99	44.51	0.99
2	XY dir. Sin 5Hz	X-1-90	1.74	1.00	1.88	1.00	1.72	1.00
2	XY dir. Sin 5Hz	Y-1-90	37.49	1.00	37.53	1.00	37.92	1.00

Study case 1

VS algorithm:			KF		AKF		LSSE	
Sensor config.	**External force**	**Virtual sensor**	**e%**	**PCC**	**e%**	**PCC**	**e%**	**PCC**
2	**Summary**		**20.62**	**1.00**	**20.63**	**1.00**	**20.95**	**0.99**
3	XY dir. Noise	X-1-90	18.19	0.96	18.82	0.96	18.16	0.97
3	XY dir. Noise	Y-1-90	10.98	0.99	10.98	0.99	15.88	0.99
3	XY dir. Sin 10Hz	X-1-90	14.70	0.83	1.61	0.87	2.34	1.00
3	XY dir. Sin 10Hz	Y-1-90	46.23	0.99	37.17	0.99	7.66	1.00
3	XY dir. Sin 15Hz	X-1-90	71.79	0.95	69.55	0.95	65.23	0.96
3	XY dir. Sin 15Hz	Y-1-90	15.19	1.00	14.09	1.00	13.62	1.00
3	XY dir. Sin 2Hz	X-1-90	23.19	0.99	19.68	1.00	23.37	1.00
3	XY dir. Sin 2Hz	Y-1-90	8.19	0.99	10.48	0.99	11.25	0.99
3	XY dir. Sin 5Hz	X-1-90	17.38	0.96	40.88	0.97	23.19	1.00
3	XY dir. Sin 5Hz	Y-1-90	19.05	0.97	4.72	0.99	7.16	0.99
3	**Summary**		**24.49**	**0.99**	**22.80**	**0.99**	**18.79**	**0.99**
4	XY dir. Noise	X-1-90	4.98	0.97	4.78	0.97	5.73	0.97
4	XY dir. Noise	Y-1-90	29.42	0.99	29.37	0.99	30.41	0.98
4	XY dir. Sin 10Hz	X-1-90	6.33	0.99	6.23	0.99	6.31	0.99
4	XY dir. Sin 10Hz	Y-1-90	36.42	1.00	36.73	1.00	36.73	0.99
4	XY dir. Sin 15Hz	X-1-90	44.05	1.00	43.97	1.00	44.02	1.00
4	XY dir. Sin 15Hz	Y-1-90	25.24	1.00	25.28	1.00	25.03	1.00
4	XY dir. Sin 2Hz	X-1-90	3.50	1.00	3.07	1.00	5.14	1.00
4	XY dir. Sin 2Hz	Y-1-90	44.52	0.99	44.16	0.99	54.71	0.99
4	XY dir. Sin 5Hz	X-1-90	0.68	1.00	0.68	1.00	1.14	1.00

VS algorithm:			KF		AKF		LSSE	
Sensor config.	**External force**	**Virtual sensor**	**e%**	**PCC**	**e%**	**PCC**	**e%**	**PCC**
4	XY dir. Sin 5Hz	Y-1-90	43.97	0.99	44.24	0.99	47.50	0.99
4	**Summary**		**23.91**	**0.99**	**23.85**	**0.99**	**25.67**	**0.99**
5	XY dir. Noise	X-1-90	59.16	0.82	60.13	0.82	56.58	0.78
5	XY dir. Noise	Y-1-90	21.17	0.86	21.54	0.86	24.80	0.75
5	XY dir. Sin 10Hz	X-1-90	29.79	0.74	27.66	0.73	31.40	0.68
5	XY dir. Sin 10Hz	Y-1-90	8.47	0.96	6.93	0.96	5.06	0.94
5	XY dir. Sin 15Hz	X-1-90	105.34	0.99	111.27	0.99	118.44	0.97
5	XY dir. Sin 15Hz	Y-1-90	44.56	0.99	45.16	0.99	54.66	0.99
5	XY dir. Sin 2Hz	X-1-90	66.14	0.99	64.55	0.99	66.68	0.99
5	XY dir. Sin 2Hz	Y-1-90	18.17	0.98	16.31	0.98	20.91	0.97
5	XY dir. Sin 5Hz	X-1-90	53.26	0.98	56.45	0.98	54.58	0.98
5	XY dir. Sin 5Hz	Y-1-90	14.97	0.97	18.19	0.97	18.82	0.95
5	**Summary**		**42.10**	**0.98**	**42.82**	**0.98**	**45.19**	**0.90**

Table 4-15 *Results obtained with sensor configurations 1 to 5 (only strain gauges are used as input sensors). External forces applied in XY direction.*

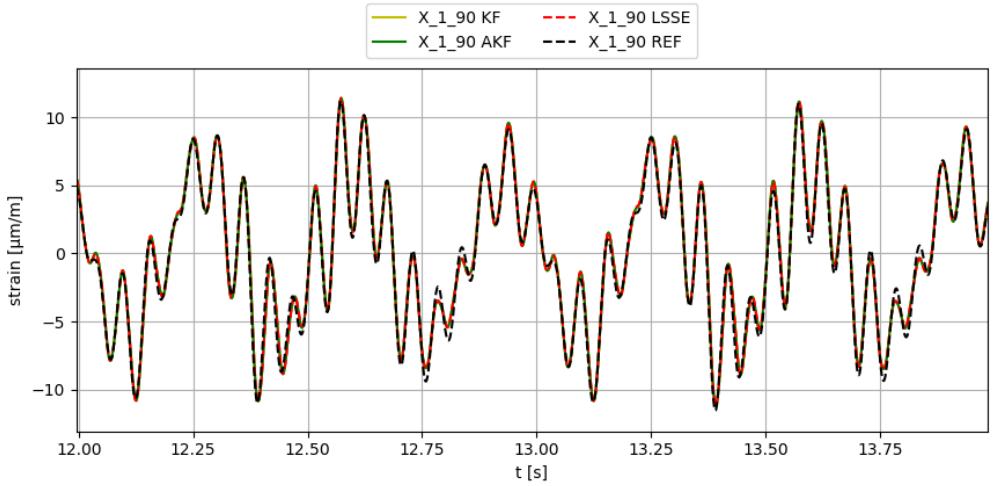

Figure 4-30 *Plot of results obtained at gauge X-1-90 using sensor config. 1, applying white noise force in XY 45º direction.*

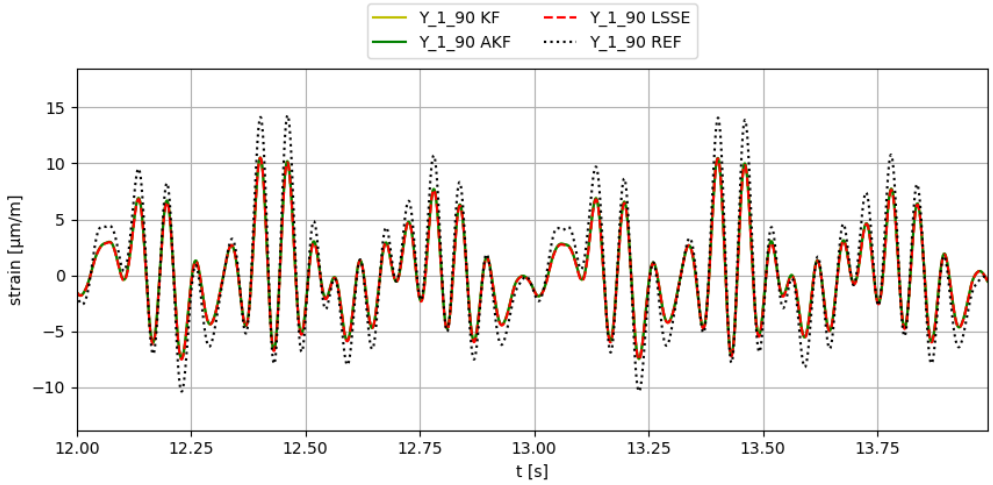

Figure 4-31 *Plot of results obtained at gauge Y-1-90 using sensor config. 1, applying white noise force in XY 45º direction.*

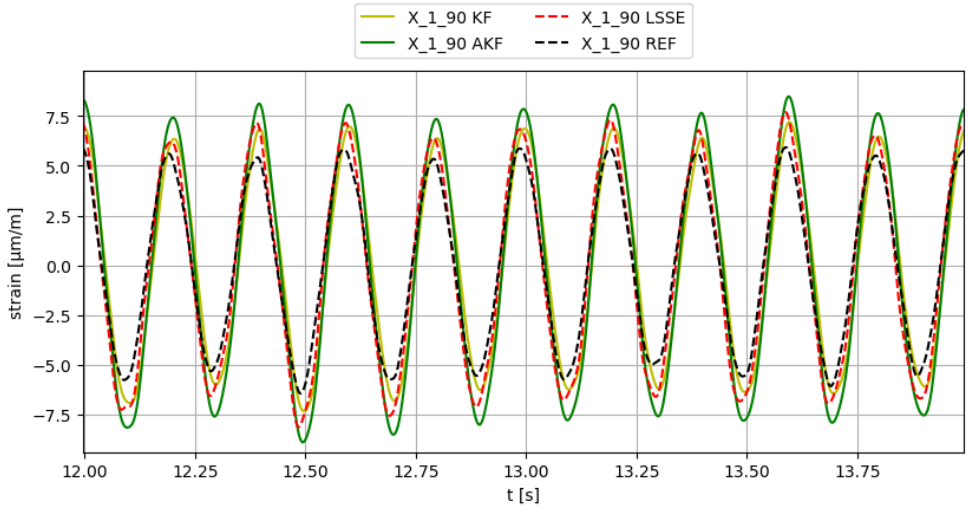

Figure 4-32 *Plot of results obtained at gauge X-1-90 using sensor config. 3, applying sin 5Hz force in XY 45º direction.*

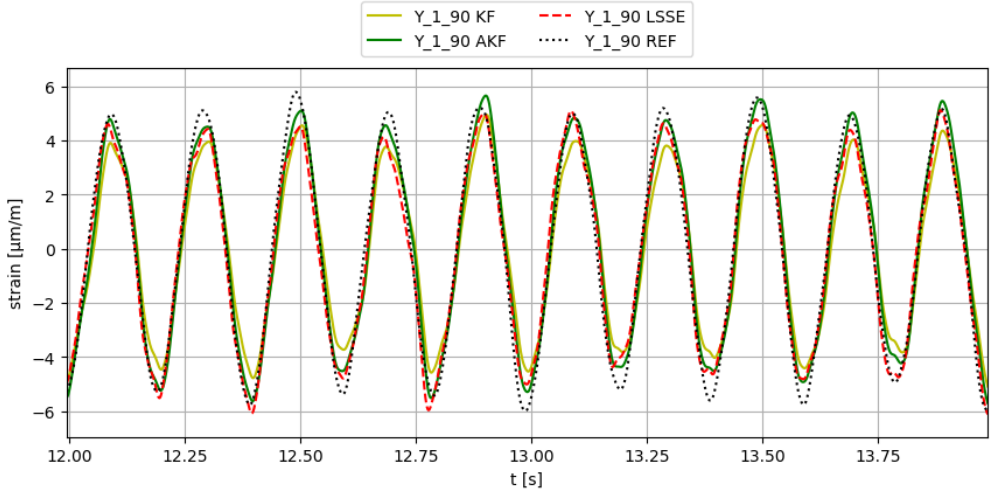

Figure 4-33 *Plot of results obtained at gauge Y-1-90 using sensor config. 3, applying sin 5Hz force in XY 45º direction.*

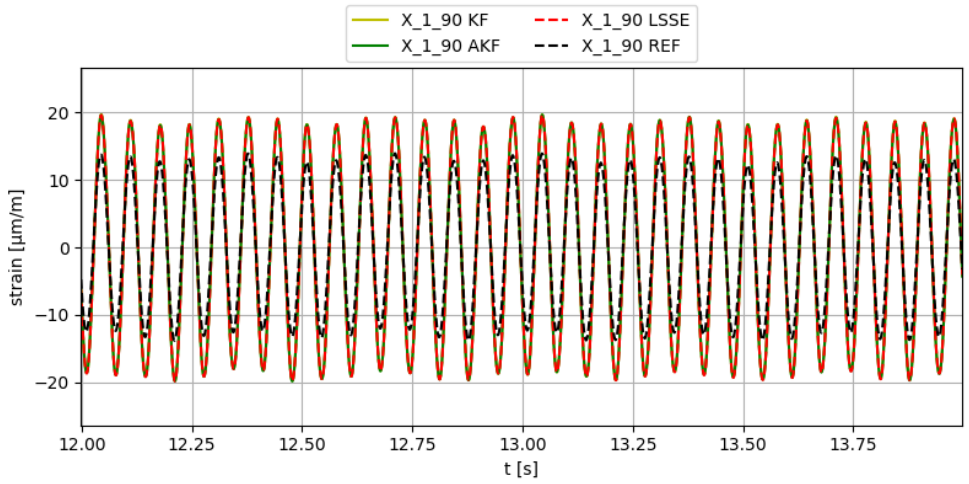

Figure 4-34 *Plot of results obtained at gauge X-1-90 using sensor config. 4, applying sin 15Hz force in XY 45º direction.*

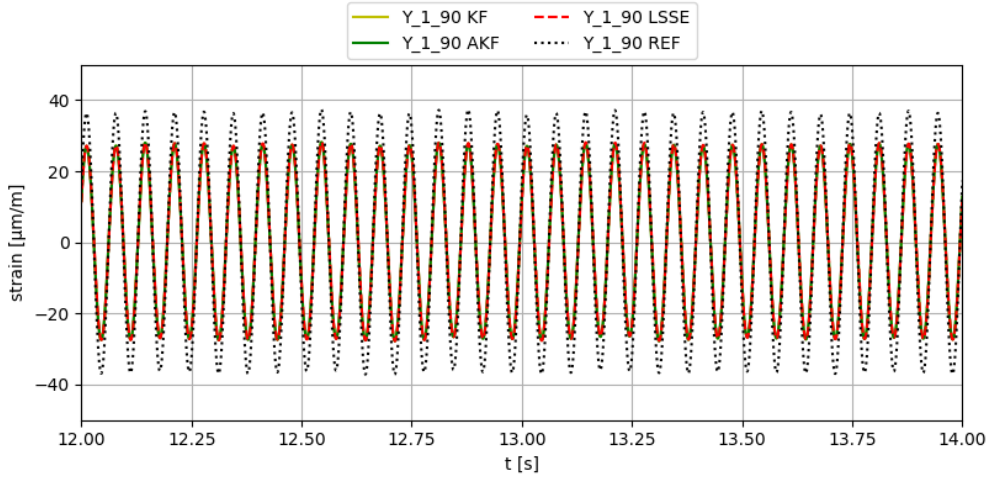

Figure 4-35 *Plot of results obtained at gauge Y-1-90 using sensor config. 4, applying sin 15Hz force in XY 45º direction.*

VS algorithm:			KF		AKF		LSSE	
Sensor config.	**External force**	**Virtual sensor**	**e%**	**PCC**	**e%**	**PCC**	**e%**	**PCC**
1	VAR dir. Sin 15Hz	X-1-90	28.19	1.00	27.65	0.99	27.70	0.99
1	VAR dir. Sin 15Hz	Y-1-90	15.92	1.00	15.89	1.00	15.86	1.00
1	VAR dir. Sin 5Hz	X-1-90	0.35	0.99	0.07	0.99	0.18	0.99
1	VAR dir. Sin 5Hz	Y-1-90	30.76	0.99	30.75	0.99	30.97	0.99
1	X dir. impacts	X-1-90	6.73	1.00	6.73	1.00	6.74	0.99
1	X dir. impacts	Y-1-90	29.47	0.91	29.47	0.91	30.20	0.91
2	VAR dir. Sin 15Hz	X-1-90	35.95	0.99	35.66	0.99	35.72	0.99
2	VAR dir. Sin 15Hz	Y-1-90	14.58	1.00	14.61	1.00	14.58	1.00
2	VAR dir. Sin 5Hz	X-1-90	3.93	0.99	3.92	0.99	4.16	0.99
2	VAR dir. Sin 5Hz	Y-1-90	35.05	0.99	35.08	0.99	35.68	0.99
2	X dir. impacts	X-1-90	10.99	0.99	10.88	0.99	11.10	0.99
2	X dir. impacts	Y-1-90	31.89	0.88	31.87	0.88	34.32	0.89
3	VAR dir. Sin 15Hz	X-1-90	23.69	0.95	10.67	0.96	15.01	1.00
3	VAR dir. Sin 15Hz	Y-1-90	9.25	0.99	7.11	1.00	1.61	1.00
3	VAR dir. Sin 5Hz	X-1-90	6.27	0.86	29.30	0.97	16.78	0.99
3	VAR dir. Sin 5Hz	Y-1-90	17.03	0.97	2.52	0.98	4.10	0.99
3	X dir. impacts	X-1-90	11.92	0.99	11.67	1.00	11.62	1.00
3	X dir. impacts	Y-1-90	3.03	0.94	1.70	0.94	3.16	0.92
4	VAR dir. Sin 15Hz	X-1-90	44.60	0.97	45.53	0.98	45.67	0.98
4	VAR dir. Sin 15Hz	Y-1-90	21.25	1.00	21.64	1.00	21.60	1.00
4	VAR dir. Sin 5Hz	X-1-90	5.15	0.99	6.09	0.99	6.89	0.99

4	VAR dir. Sin 5Hz	Y-1-90	41.31	0.98	41.63	0.98	45.87	0.98
4	X dir. impacts	X-1-90	12.89	0.99	12.56	0.99	14.08	0.99
4	X dir. impacts	Y-1-90	33.67	0.85	33.80	0.85	43.06	0.85
5	VAR dir. Sin 15Hz	X-1-90	53.42	0.96	57.15	0.96	63.73	0.98
5	VAR dir. Sin 15Hz	Y-1-90	28.21	0.98	27.86	0.99	34.02	0.98
5	VAR dir. Sin 5Hz	X-1-90	46.09	0.93	48.56	0.98	48.01	0.99
5	VAR dir. Sin 5Hz	Y-1-90	15.33	0.98	17.91	0.98	18.52	0.97
5	X dir. impacts	X-1-90	44.69	0.99	44.55	0.99	45.21	0.99
5	X dir. impacts	Y-1-90	17.48	0.95	17.75	0.95	21.56	0.91

Table 4-16 *Results obtained with sensor configurations 1 to 5 (only strain gauges are used as input sensors). Stochastic events.*

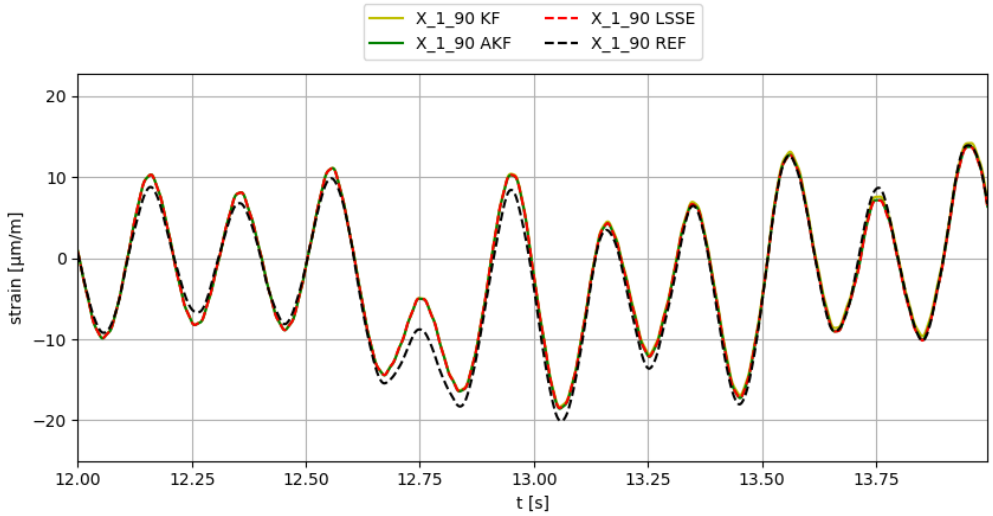

Figure 4-36 *Plot of results obtained at gauge X-1-90 using sensor config. 1, applying sin 5Hz force in variable direction.*

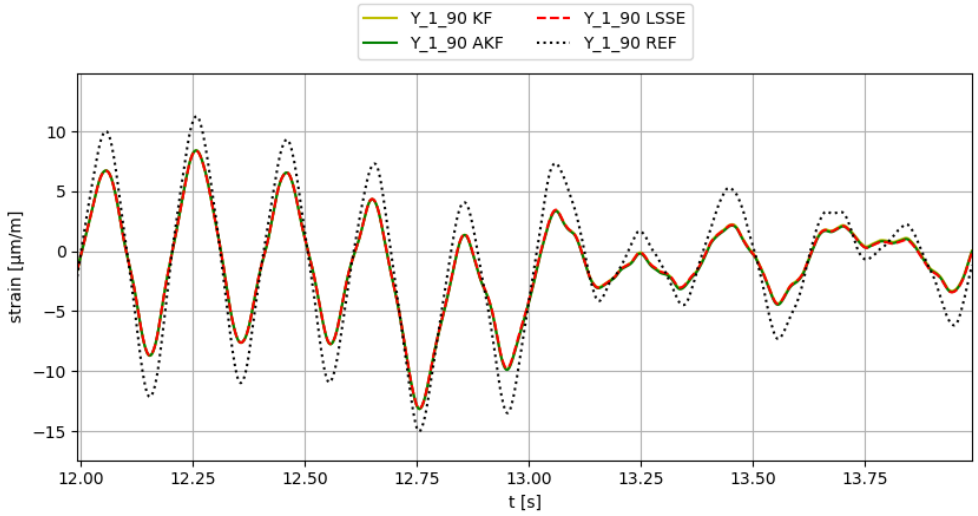

Figure 4-37 *Plot of results obtained at gauge Y-1-90 using sensor config. 1, applying sin 5Hz force in variable direction.*

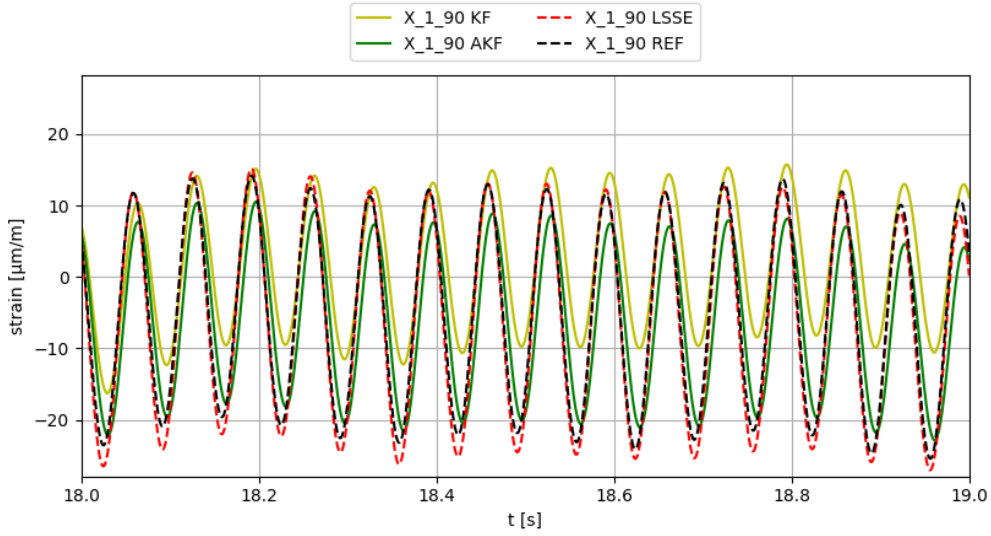

Figure 4-38 *Plot of results obtained at gauge X-1-90 using sensor config. 3, applying sin 15Hz force in variable direction.*

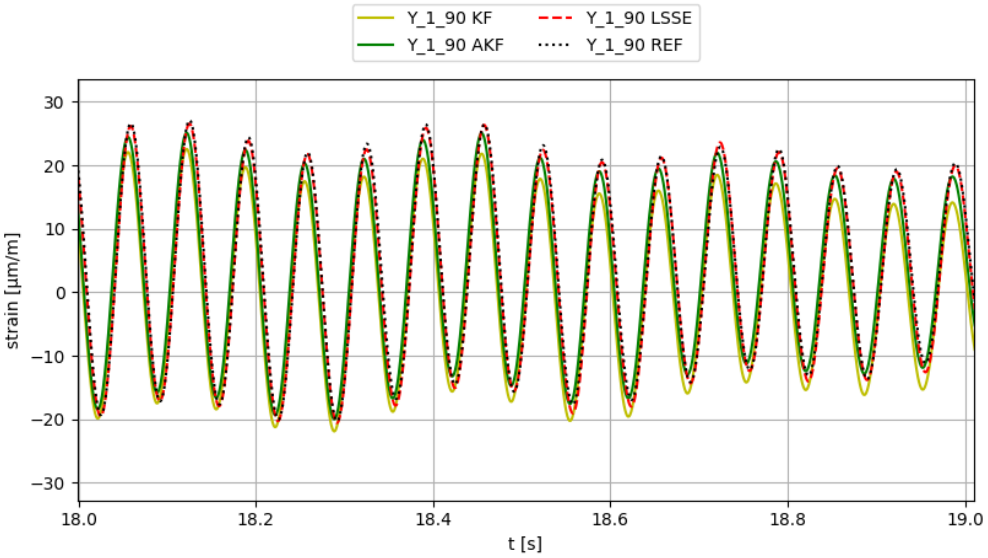

Figure 4-39 *Plot of results obtained at gauge Y-1-90 using sensor config. 3, applying sin 15Hz force in variable direction.*

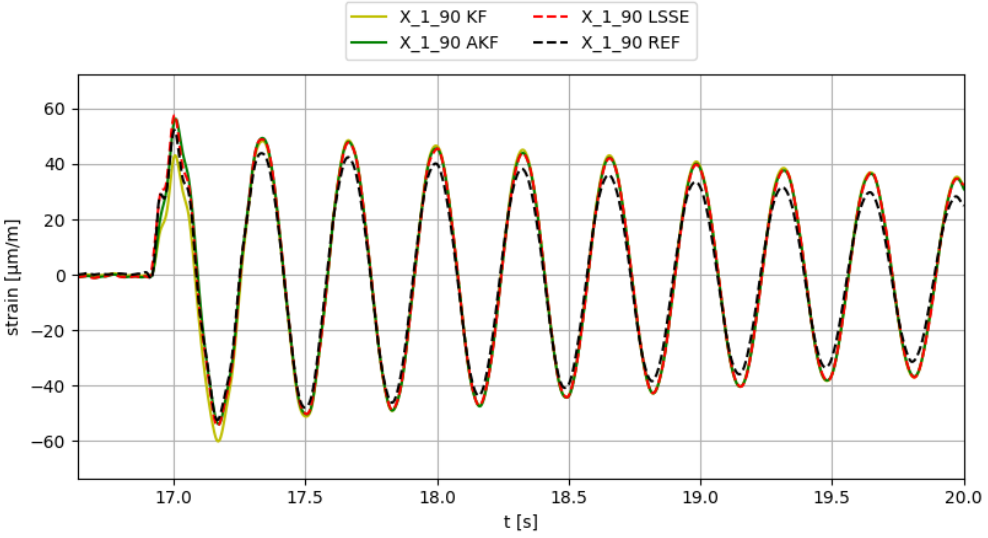

Figure 4-40 *Plot of results obtained at gauge X-1-90 using sensor config. 3, applying an impact in X direction.*

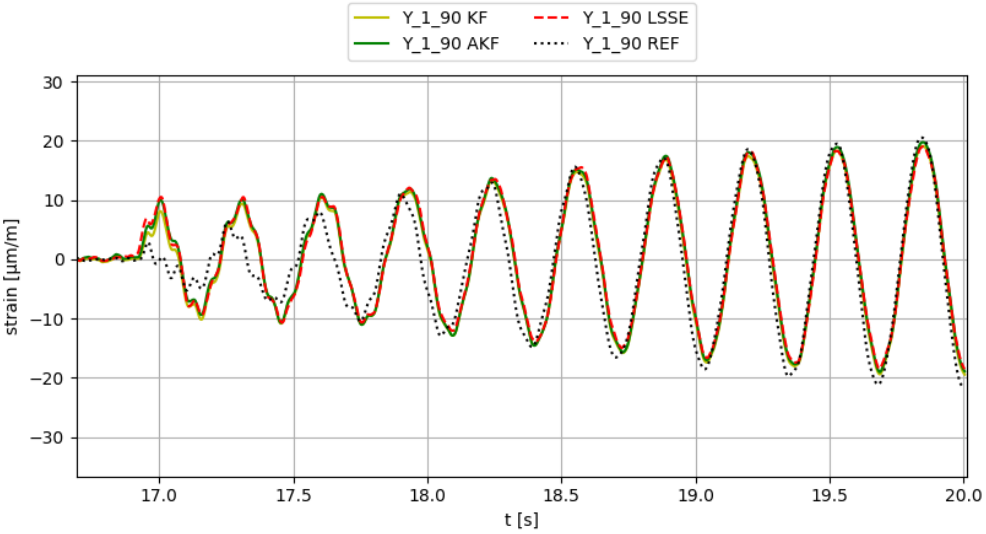

Figure 4-41 *Plot of results obtained at gauge Y-1-90 using sensor config. 3, applying an impact in X direction.*

Study case 1

VS algorithm:			KF		AKF	
Sensor config.	**External force**	**Virtual sensor**	**e%**	**PCC**	**e%**	**PCC**
6	X dir. Noise	X-1-90	12.63	0.84	3.20	0.98
6	X dir. Sin 10Hz	X-1-90	11.88	0.77	8.76	0.98
6	X dir. Sin 15Hz	X-1-90	22.44	0.98	11.20	1.00
6	X dir. Sin 2Hz	X-1-90	37.08	0.78	13.79	1.00
6	X dir. Sin 5Hz	X-1-90	6.84	0.96	14.89	1.00
6	**Summary**		**18.18**	**0.86**	**10.37**	**0.99**
7	X dir. Noise	X-1-90	12.63	0.84	12.47	0.98
7	X dir. Sin 10Hz	X-1-90	11.88	0.77	15.07	0.98
7	X dir. Sin 15Hz	X-1-90	22.44	0.98	18.23	1.00
7	X dir. Sin 2Hz	X-1-90	37.08	0.78	16.47	1.00
7	X dir. Sin 5Hz	X-1-90	6.84	0.96	17.92	1.00
7	**Summary**		**18.18**	**0.86**	**16.03**	**0.99**
8	X dir. Noise	X-1-90	12.63	0.84	11.83	0.95
8	X dir. Sin 10Hz	X-1-90	11.88	0.77	2.62	0.95
8	X dir. Sin 15Hz	X-1-90	22.44	0.98	1.83	0.98
8	X dir. Sin 2Hz	X-1-90	37.08	0.78	1.10	1.00
8	X dir. Sin 5Hz	X-1-90	6.84	0.96	4.94	0.99
8	**Summary**		**18.18**	**0.86**	**4.46**	**0.97**
9	X dir. Noise	X-1-90	12.63	0.84	22.95	0.99
9	X dir. Sin 10Hz	X-1-90	11.88	0.77	18.02	0.99
9	X dir. Sin 15Hz	X-1-90	22.44	0.98	23.28	1.00

VS algorithm:			KF		AKF	
Sensor config.	**External force**	**Virtual sensor**	**e%**	**PCC**	**e%**	**PCC**
9	X dir. Sin 2Hz	X-1-90	37.08	0.78	9.35	1.00
9	X dir. Sin 5Hz	X-1-90	6.84	0.96	11.73	1.00
9	**Summary**		**18.18**	**0.86**	**17.06**	**1.00**
10	X dir. Noise	X-1-90	12.63	0.84	18.47	0.43
10	X dir. Sin 10Hz	X-1-90	11.88	0.77	13.42	0.65
10	X dir. Sin 15Hz	X-1-90	22.44	0.98	20.59	0.97
10	X dir. Sin 2Hz	X-1-90	37.08	0.78	46.58	0.97
10	X dir. Sin 5Hz	X-1-90	6.84	0.96	3.03	0.91
10	**Summary**		**18.18**	**0.86**	**20.42**	**0.78**
11	X dir. Noise	X-1-90	53.93	0.83	42.33	0.87
11	X dir. Sin 10Hz	X-1-90	88.09	0.61	64.30	0.70
11	X dir. Sin 15Hz	X-1-90	40.68	1.00	62.87	0.97
11	X dir. Sin 2Hz	X-1-90	35.48	0.74	37.06	0.70
11	X dir. Sin 5Hz	X-1-90	74.42	0.84	76.27	0.89
11	**Summary**		**58.52**	**0.80**	**56.57**	**0.83**
12	X dir. Sin 10Hz	X-1-90	88.09	0.61	3.85	0.83
12	X dir. Sin 15Hz	X-1-90	40.68	1.00	23.37	0.98
12	X dir. Sin 2Hz	X-1-90	35.48	0.74	36.02	0.76
12	X dir. Sin 5Hz	X-1-90	74.42	0.84	27.35	0.96
12	**Summary**		**58.52**	**0.80**	**21.06**	**0.88**

Table 4-17 *Results obtained with sensor configurations 6 to 12 (strain gauges and accelerometer used as input sensors). External forces applied in X direction.*

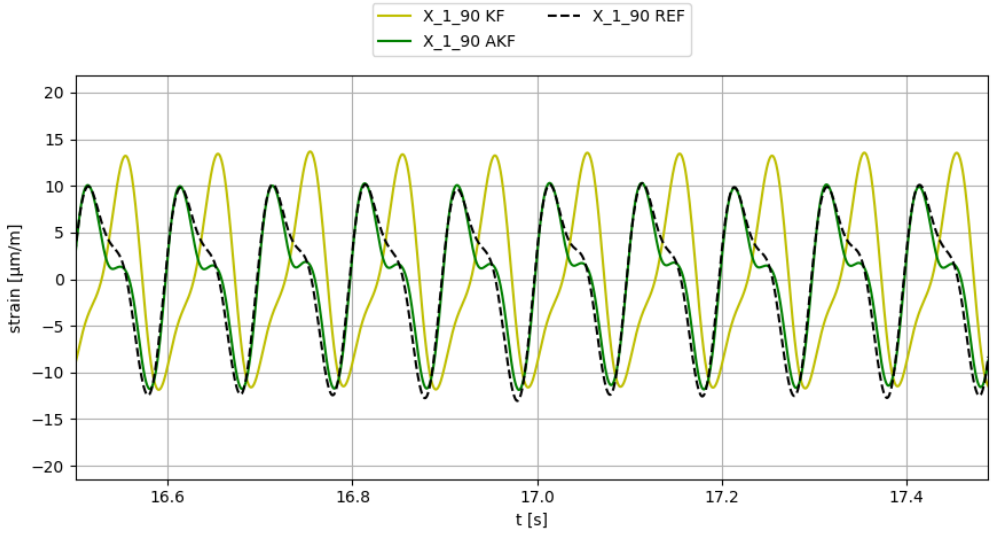

Figure 4-42 *Plot of results obtained at gauge X-1-90 using sensor config. 6, applying sin10Hz force in X direction.*

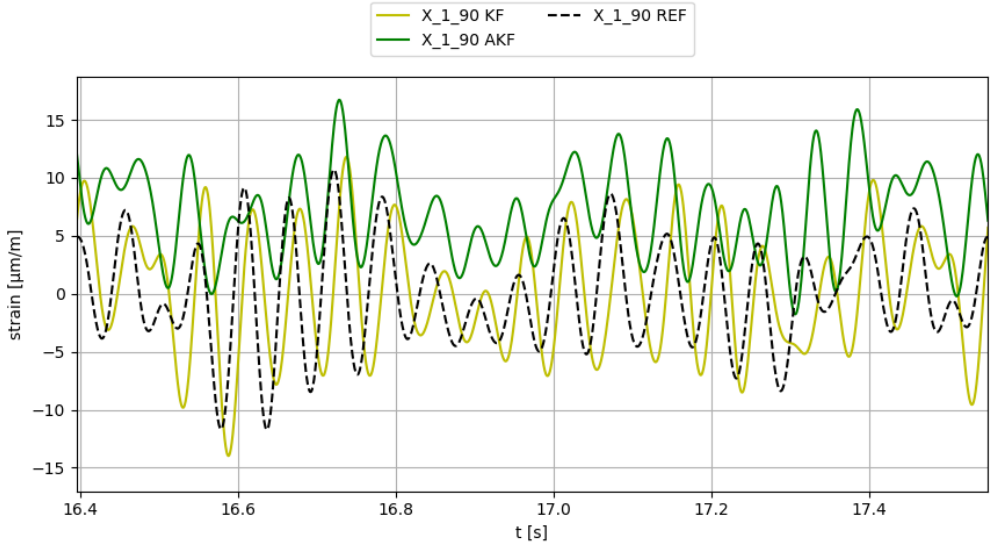

Figure 4-43 *Plot of results obtained at gauge X-1-90 using sensor config. 10, applying white noise force in X direction.*

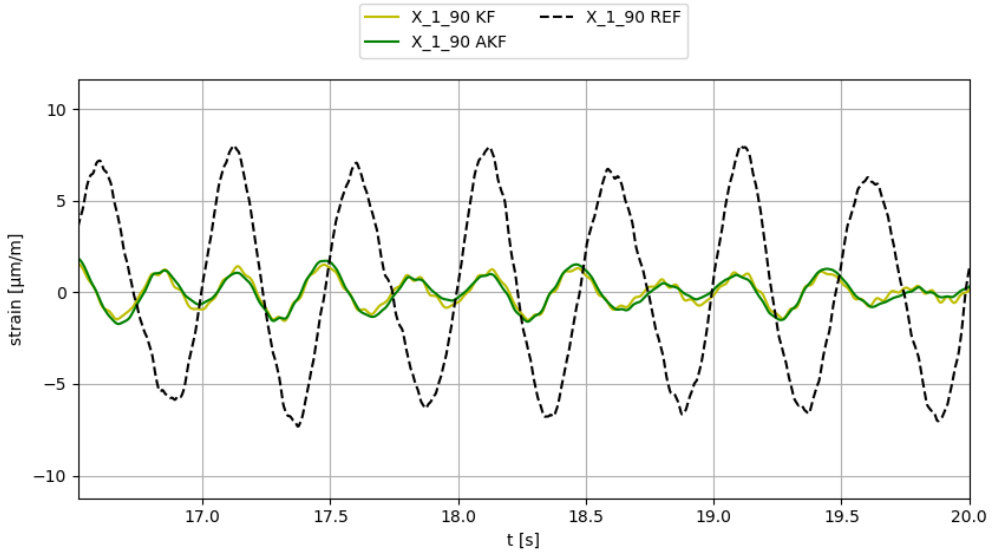

Figure 4-44 *Plot of results obtained at gauge X-1-90 using sensor config. 11, applying sin 2Hz force in X direction.*

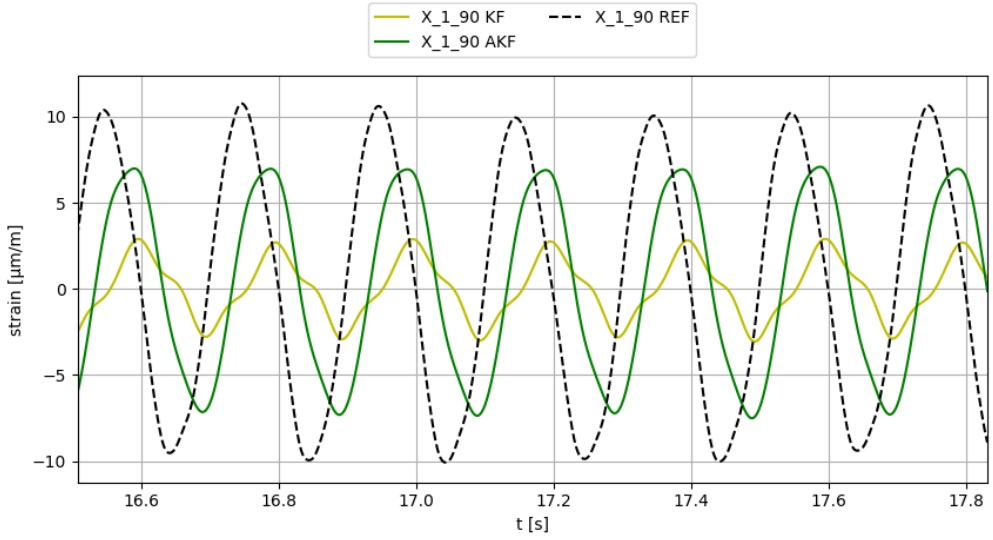

Figure 4-45 *Plot of results obtained at gauge X-1-90 using sensor config. 12, applying white noise force in X direction.*

Study case 1

VS algorithm:			KF		AKF	
Sensor config.	**External force**	**Virtual sensor**	**e%**	**PCC**	**e%**	**PCC**
6	Y dir. Noise	Y-1-90	36.80	0.47	27.61	0.98
6	Y dir. Sin 10Hz	Y-1-90	88.82	0.58	29.31	1.00
6	Y dir. Sin 15Hz	Y-1-90	65.16	0.97	27.61	0.99
6	Y dir. Sin 2Hz	Y-1-90	50.84	0.69	34.84	1.00
6	Y dir. Sin 5Hz	Y-1-90	72.72	0.84	33.73	1.00
6	**Summary**		**62.87**	**0.71**	**30.62**	**0.99**
7	Y dir. Noise	Y-1-90	36.80	0.47	28.71	0.99
7	Y dir. Sin 10Hz	Y-1-90	88.82	0.58	26.85	1.00
7	Y dir. Sin 15Hz	Y-1-90	65.16	0.97	29.57	1.00
7	Y dir. Sin 2Hz	Y-1-90	50.84	0.69	21.18	1.00
7	Y dir. Sin 5Hz	Y-1-90	72.72	0.84	22.81	1.00
7	**Summary**		**62.87**	**0.71**	**25.82**	**1.00**
8	Y dir. Noise	Y-1-90	36.80	0.47	30.16	0.95
8	Y dir. Sin 10Hz	Y-1-90	88.82	0.58	20.15	0.99
8	Y dir. Sin 15Hz	Y-1-90	65.16	0.97	36.85	0.98
8	Y dir. Sin 2Hz	Y-1-90	50.84	0.69	4.64	1.00
8	Y dir. Sin 5Hz	Y-1-90	72.72	0.84	0.26	1.00
8	**Summary**		**62.87**	**0.71**	**18.41**	**0.98**
9	Y dir. Noise	Y-1-90	36.80	0.47	50.39	0.79
9	Y dir. Sin 10Hz	Y-1-90	88.82	0.58	79.86	0.87
9	Y dir. Sin 15Hz	Y-1-90	36.80	0.47	56.05	0.97

VS algorithm:			KF		AKF	
Sensor config.	**External force**	**Virtual sensor**	**e%**	**PCC**	**e%**	**PCC**
9	Y dir. Sin 2Hz	Y-1-90	50.84	0.69	54.49	0.75
9	Y dir. Sin 5Hz	Y-1-90	72.72	0.84	72.12	0.83
9	**Summary**		**62.87**	**0.71**	**62.58**	**0.84**
10	Y dir. Noise	Y-1-90	36.80	0.47	48.75	0.67
10	Y dir. Sin 10Hz	Y-1-90	88.82	0.58	85.70	0.72
10	Y dir. Sin 15Hz	Y-1-90	65.16	0.97	60.69	0.97
10	Y dir. Sin 2Hz	Y-1-90	50.84	0.69	44.60	0.67
10	Y dir. Sin 5Hz	Y-1-90	72.72	0.84	79.27	0.66
10	**Summary**		**62.87**	**0.71**	**63.80**	**0.74**
11	Y dir. Noise	Y-1-90	50.34	0.49	52.57	0.84
11	Y dir. Sin 10Hz	Y-1-90	90.89	0.40	82.21	0.91
11	Y dir. Sin 15Hz	Y-1-90	69.43	0.97	53.89	0.98
11	Y dir. Sin 2Hz	Y-1-90	50.53	0.67	58.08	0.66
11	Y dir. Sin 5Hz	Y-1-90	79.80	0.73	86.22	0.49
11	**Summary**		**68.20**	**0.65**	**66.59**	**0.78**
12	Y dir. Sin 10Hz	Y-1-90	90.89	0.40	87.55	0.72
12	Y dir. Sin 15Hz	Y-1-90	69.43	0.97	62.10	0.97
12	Y dir. Sin 2Hz	Y-1-90	50.53	0.67	50.87	0.65
12	Y dir. Sin 5Hz	Y-1-90	79.80	0.73	81.47	0.71
12	**Summary**		**68.20**	**0.65**	**66.34**	**0.73**

Table 4-18 *Results obtained with sensor configurations 6 to 12 (strain gauges and accelerometer used as input sensors). External forces applied in Y direction.*

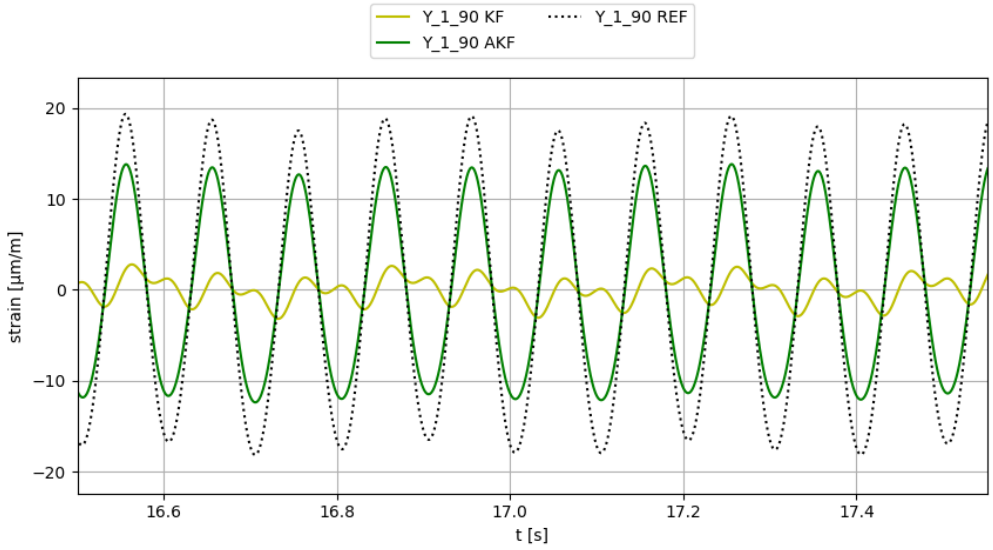

Figure 4-46 *Plot of results obtained at gauge Y-1-90 using sensor config. 6, applying sin10Hz force in Y direction.*

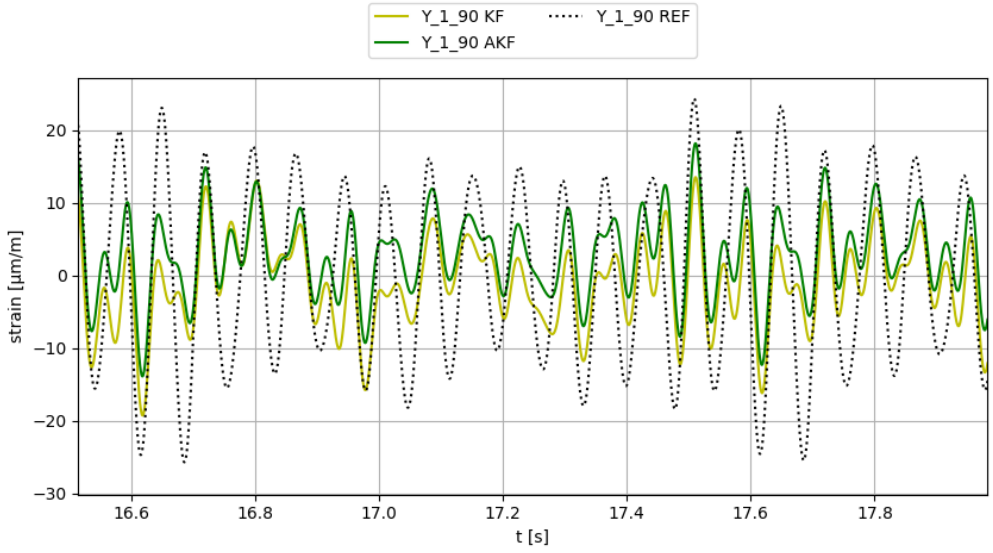

Figure 4-47 *Plot of results obtained at gauge Y-1-90 using sensor config. 10, applying white noise force in Y direction.*

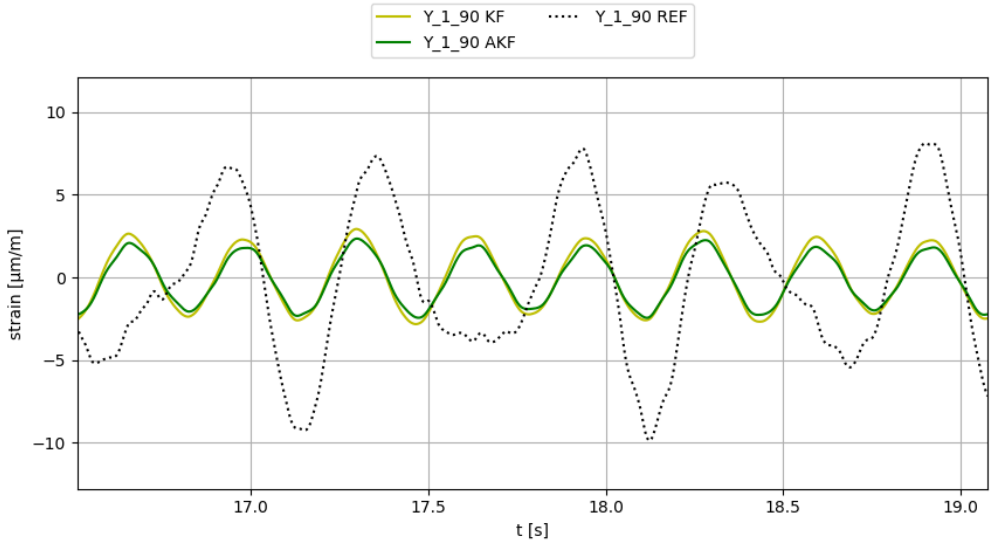

Figure 4-48 *Plot of results obtained at gauge Y-1-90 using sensor config. 11, applying sin2Hz force in Y direction.*

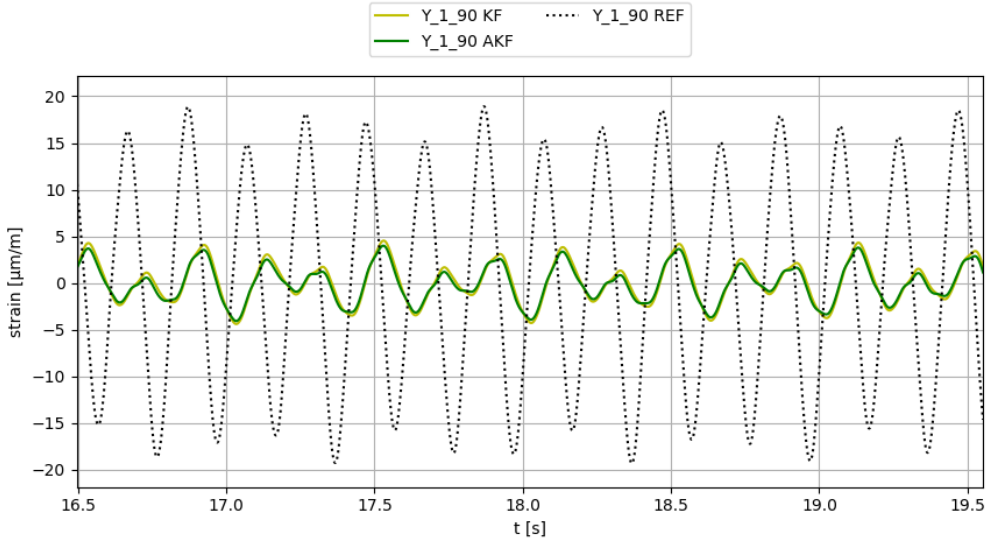

Figure 4-49 *Plot of results obtained at gauge Y-1-90 using sensor config. 12, applying sin5Hz force in Y direction.*

Study case 1

VS algorithm:			KF		AKF	
Sensor config.	**External force**	**Virtual sensor**	**e%**	**PCC**	**e%**	**PCC**
6	XY dir. Noise	X-1-90	11.76	0.91	1.02	0.98
6	XY dir. Noise	Y-1-90	32.03	0.85	33.75	0.98
6	XY dir. Sin 10Hz	X-1-90	20.33	0.80	9.21	0.99
6	XY dir. Sin 10Hz	Y-1-90	85.46	0.51	35.15	0.99
6	XY dir. Sin 15Hz	X-1-90	34.02	0.97	40.88	0.99
6	XY dir. Sin 15Hz	Y-1-90	63.97	0.97	29.82	0.99
6	XY dir. Sin 2Hz	X-1-90	2.45	0.93	2.44	1.00
6	XY dir. Sin 2Hz	Y-1-90	20.82	0.84	50.32	0.99
6	XY dir. Sin 5Hz	X-1-90	1.63	0.95	1.73	1.00
6	XY dir. Sin 5Hz	Y-1-90	72.38	0.87	44.24	0.99
6	**Summary**		**34.49**	**0.91**	**24.85**	**0.99**
7	XY dir. Noise	X-1-90	11.76	0.91	7.32	0.97
7	XY dir. Noise	Y-1-90	32.03	0.85	32.86	0.99
7	XY dir. Sin 10Hz	X-1-90	20.33	0.80	5.15	0.99
7	XY dir. Sin 10Hz	Y-1-90	85.46	0.51	34.05	0.99
7	XY dir. Sin 15Hz	X-1-90	34.02	0.97	37.99	0.98
7	XY dir. Sin 15Hz	Y-1-90	63.97	0.97	32.46	0.99
7	XY dir. Sin 2Hz	X-1-90	2.45	0.93	5.16	1.00
7	XY dir. Sin 2Hz	Y-1-90	20.82	0.84	38.03	1.00
7	XY dir. Sin 5Hz	X-1-90	1.63	0.95	1.10	1.00
7	XY dir. Sin 5Hz	Y-1-90	72.38	0.87	35.09	1.00

VS algorithm:			**KF**		**AKF**	
Sensor config.	**External force**	**Virtual sensor**	**e%**	**PCC**	**e%**	**PCC**
7	**Summary**		**34.49**	**0.91**	**22.92**	**1.00**
8	XY dir. Noise	X-1-90	11.76	0.91	14.67	0.98
8	XY dir. Noise	Y-1-90	32.03	0.85	30.48	0.96
8	XY dir. Sin 10Hz	X-1-90	20.33	0.80	12.33	0.96
8	XY dir. Sin 10Hz	Y-1-90	85.46	0.51	29.34	0.98
8	XY dir. Sin 15Hz	X-1-90	34.02	0.97	19.71	0.97
8	XY dir. Sin 15Hz	Y-1-90	63.97	0.97	40.72	0.99
8	XY dir. Sin 2Hz	X-1-90	2.45	0.93	9.30	1.00
8	XY dir. Sin 2Hz	Y-1-90	20.82	0.84	11.51	0.99
8	XY dir. Sin 5Hz	X-1-90	1.63	0.95	10.89	0.99
8	XY dir. Sin 5Hz	Y-1-90	72.38	0.87	13.82	0.99
8	**Summary**		**34.49**	**0.91**	**19.28**	**0.99**
9	XY dir. Noise	X-1-90	11.76	0.91	7.22	0.97
9	XY dir. Noise	Y-1-90	32.03	0.85	38.49	0.92
9	XY dir. Sin 10Hz	X-1-90	20.33	0.80	1.07	0.99
9	XY dir. Sin 10Hz	Y-1-90	85.46	0.51	77.33	0.84
9	XY dir. Sin 15Hz	X-1-90	34.02	0.97	18.16	1.00
9	XY dir. Sin 15Hz	Y-1-90	63.97	0.97	55.03	0.98
9	XY dir. Sin 2Hz	X-1-90	2.45	0.93	2.01	1.00
9	XY dir. Sin 2Hz	Y-1-90	20.82	0.84	42.39	0.80
9	XY dir. Sin 5Hz	X-1-90	1.63	0.95	5.09	1.00

Study case 1

VS algorithm:			KF		AKF	
Sensor config.	**External force**	**Virtual sensor**	**e%**	**PCC**	**e%**	**PCC**
9	XY dir. Sin 5Hz	Y-1-90	72.38	0.87	76.64	0.90
9	**Summary**		**34.49**	**0.91**	**32.34**	**0.93**
10	XY dir. Noise	X-1-90	11.76	0.91	22.44	0.78
10	XY dir. Noise	Y-1-90	32.03	0.85	32.27	0.80
10	XY dir. Sin 10Hz	X-1-90	20.33	0.80	13.66	0.71
10	XY dir. Sin 10Hz	Y-1-90	85.46	0.51	64.54	0.34
10	XY dir. Sin 15Hz	X-1-90	34.02	0.97	34.20	0.84
10	XY dir. Sin 15Hz	Y-1-90	63.97	0.97	57.51	0.95
10	XY dir. Sin 2Hz	X-1-90	2.45	0.93	52.01	0.97
10	XY dir. Sin 2Hz	Y-1-90	20.82	0.84	32.90	0.77
10	XY dir. Sin 5Hz	X-1-90	1.63	0.95	9.98	0.92
10	XY dir. Sin 5Hz	Y-1-90	72.38	0.87	77.04	0.55
10	**Summary**		**34.49**	**0.91**	**39.65**	**0.83**
11	XY dir. Noise	X-1-90	13.30	0.85	10.25	0.88
11	XY dir. Noise	Y-1-90	41.05	0.85	42.45	0.89
11	XY dir. Sin 10Hz	X-1-90	84.35	0.59	65.24	0.71
11	XY dir. Sin 10Hz	Y-1-90	89.05	0.23	79.37	0.86
11	XY dir. Sin 15Hz	X-1-90	52.27	1.00	62.11	0.95
11	XY dir. Sin 15Hz	Y-1-90	63.65	0.99	52.74	0.98
11	XY dir. Sin 2Hz	X-1-90	6.09	0.89	2.03	0.87
11	XY dir. Sin 2Hz	Y-1-90	33.93	0.77	58.67	0.76

VS algorithm:			KF		AKF	
Sensor config.	**External force**	**Virtual sensor**	**e%**	**PCC**	**e%**	**PCC**
11	XY dir. Sin 5Hz	X-1-90	73.82	0.76	74.63	0.90
11	XY dir. Sin 5Hz	Y-1-90	81.59	0.77	91.67	0.55
11	**Summary**		**53.91**	**0.84**	**53.92**	**0.81**
12	XY dir. Noise	X-1-90	13.30	0.85	15.08	0.94
12	XY dir. Noise	Y-1-90	41.05	0.85	40.88	0.85
12	XY dir. Sin 10Hz	X-1-90	84.35	0.59	3.42	0.85
12	XY dir. Sin 10Hz	Y-1-90	89.05	0.23	84.45	0.63
12	XY dir. Sin 15Hz	X-1-90	52.27	1.00	33.54	0.97
12	XY dir. Sin 15Hz	Y-1-90	63.65	0.99	61.43	0.97
12	XY dir. Sin 2Hz	X-1-90	6.09	0.89	0.22	0.91
12	XY dir. Sin 2Hz	Y-1-90	33.93	0.77	39.69	0.69
12	XY dir. Sin 5Hz	X-1-90	73.82	0.76	23.39	0.95
12	XY dir. Sin 5Hz	Y-1-90	81.59	0.77	83.64	0.82
12	**Summary**		**53.91**	**0.84**	**38.58**	**0.87**

Table 4-19 *Results obtained with sensor configurations 6 to 12 (strain gauges and accelerometer used as input sensors). External forces applied in XY direction.*

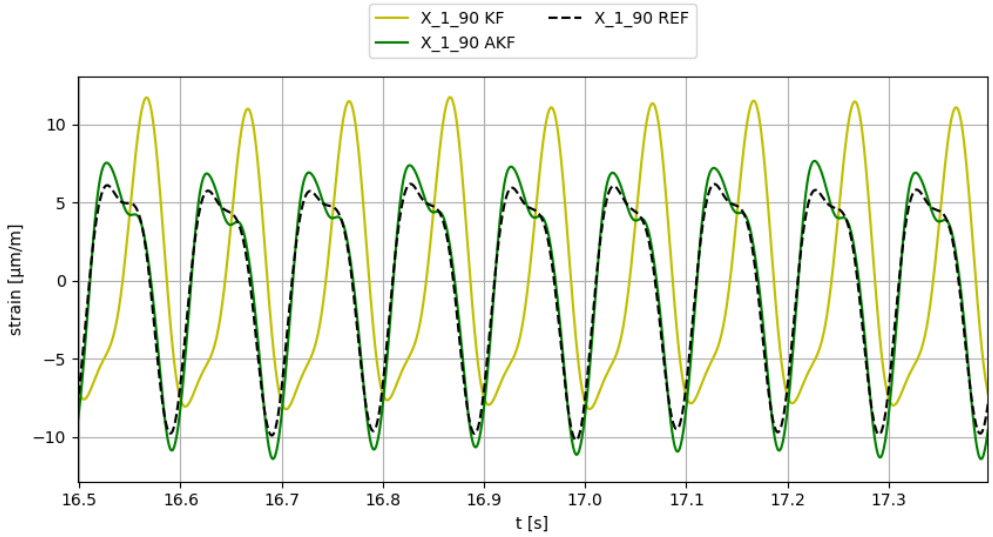

Figure 4-50 *Plot of results obtained at gauge X-1-90 using sensor config. 6, applying sin 10Hz force in XY 45º direction.*

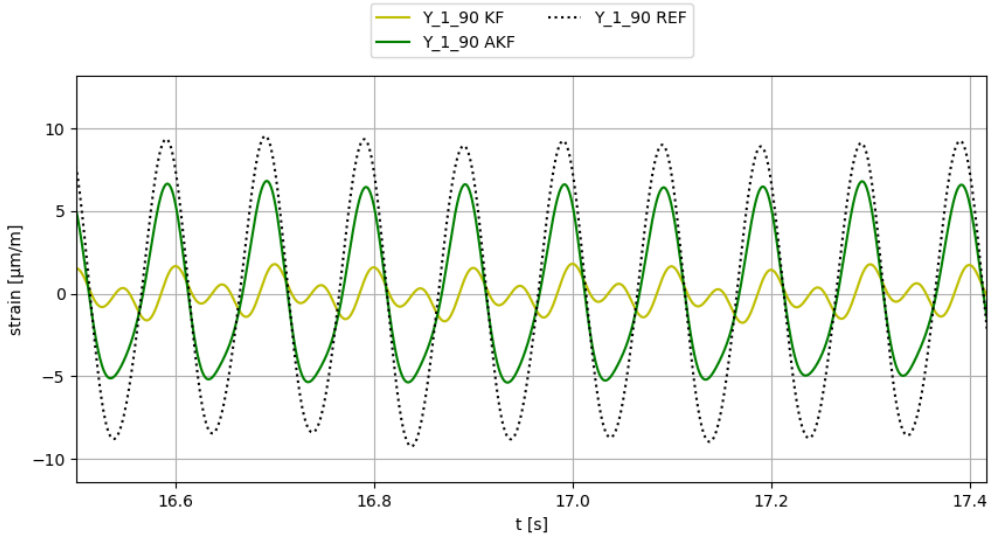

Figure 4-51 *Plot of results obtained at gauge Y-1-90 using sensor config. 6, applying sin 10Hz force in XY 45º direction.*

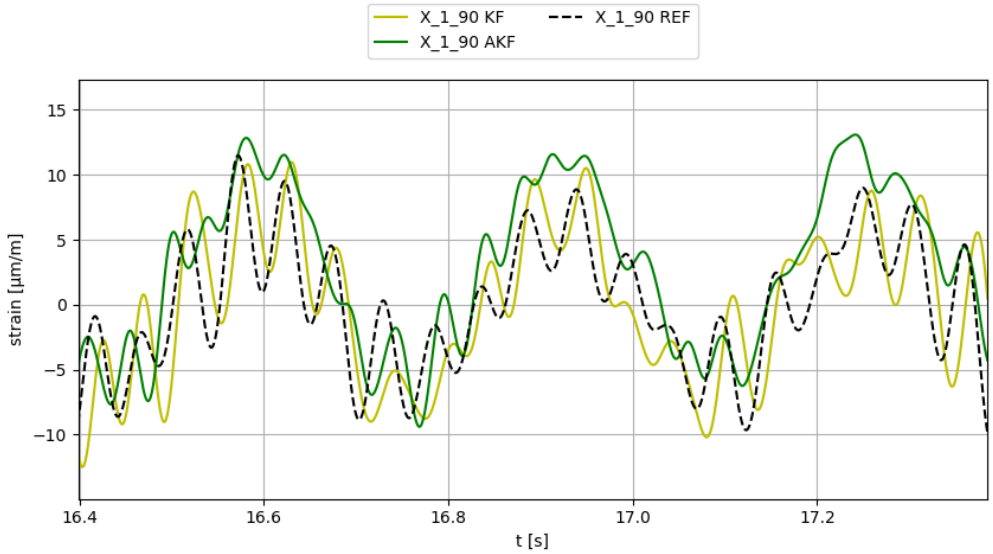

Figure 4-52 *Plot of results obtained at gauge X-1-90 using sensor config. 10, applying white noise force in XY 45º direction.*

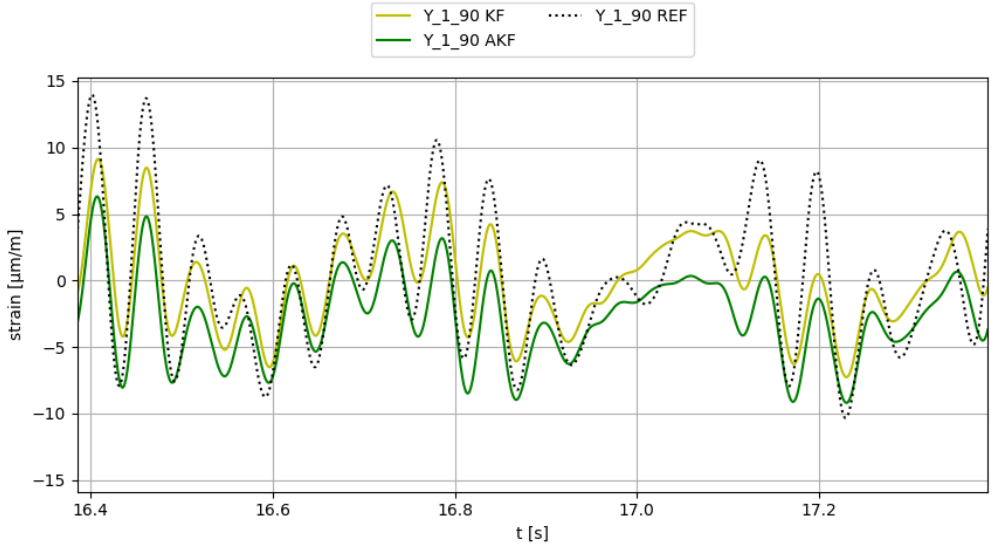

Figure 4-53 *Plot of results obtained at gauge Y-1-90 using sensor config. 10, applying white noise force in XY 45º direction.*

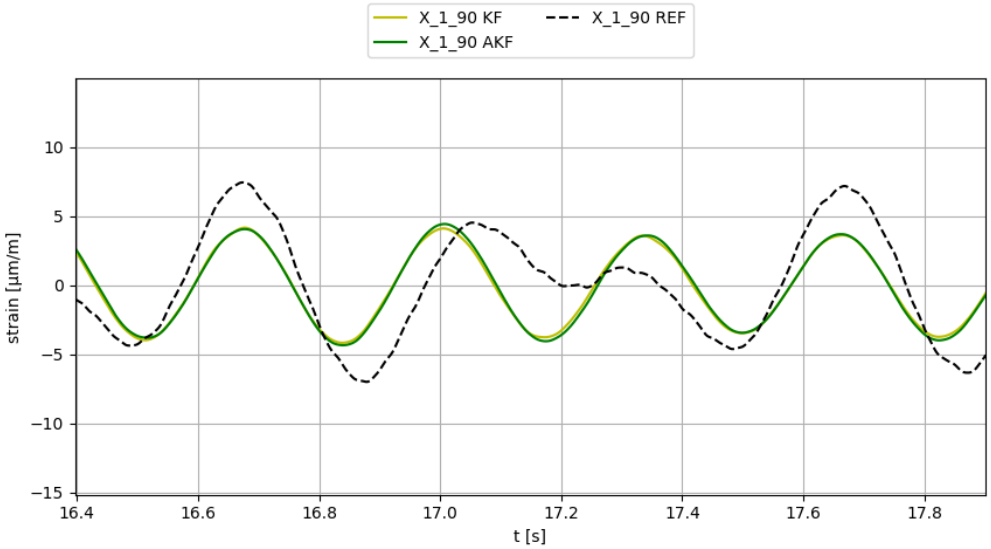

Figure 4-54 *Plot of results obtained at gauge X-1-90 using sensor config. 11, applying sin 2Hz force in XY 45º direction.*

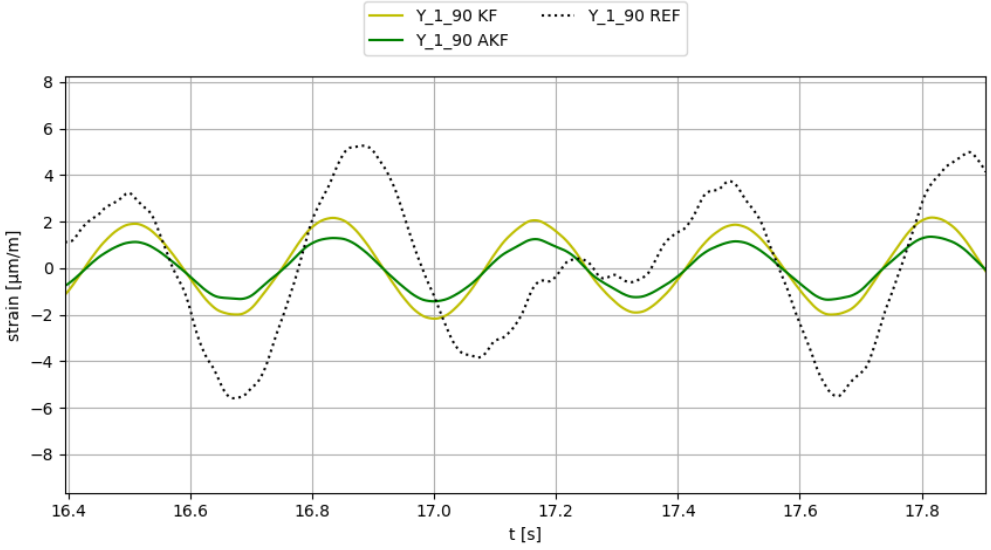

Figure 4-55 *Plot of results obtained at gauge Y-1-90 using sensor config. 11, applying sin 2Hz force in XY 45º direction.*

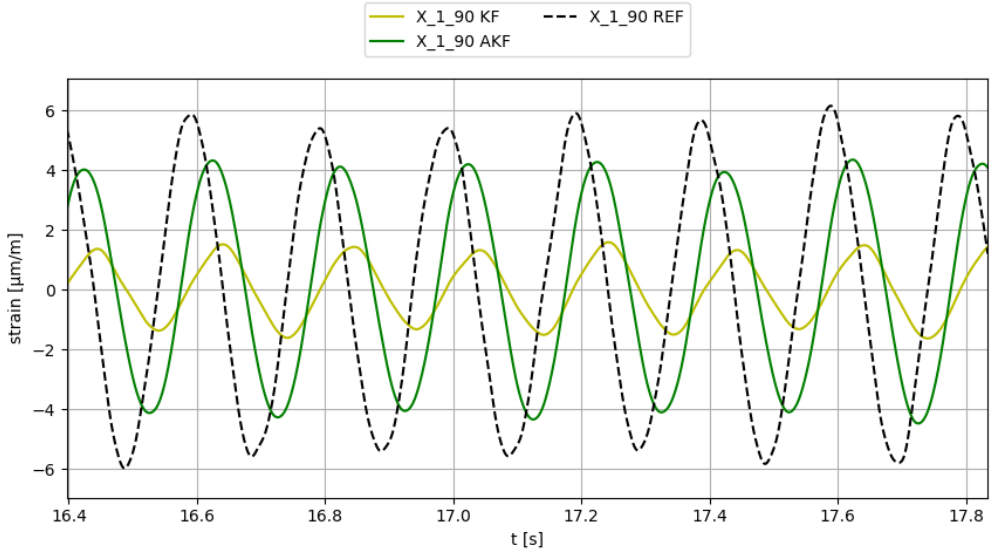

Figure 4-56 *Plot of results obtained at gauge X-1-90 using sensor config. 12, applying sin 5Hz force in XY 45º direction.*

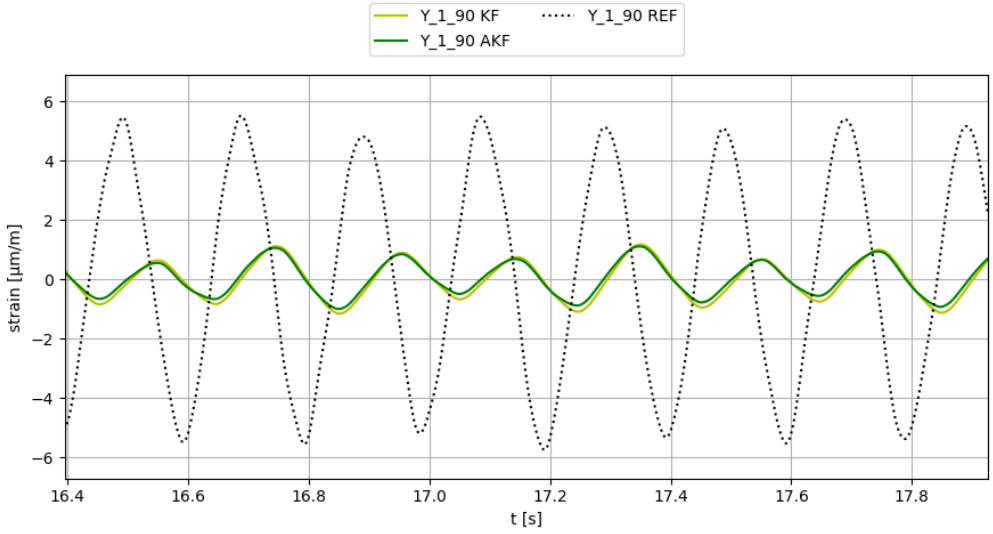

Figure 4-57 *Plot of results obtained at gauge Y-1-90 using sensor config. 12, applying sin 5Hz force in XY 45º direction.*

Study case 1

VS algorithm:			KF		AKF	
Sensor config.	**External force**	**Virtual sensor**	**e%**	**PCC**	**e%**	**PCC**
6	VAR dir. Sin 15Hz	X-1-90	16.46	0.96	34.77	0.99
6	VAR dir. Sin 15Hz	Y-1-90	64.35	0.94	26.65	0.99
6	VAR dir. Sin 5Hz	X-1-90	10.50	0.83	4.29	0.99
6	VAR dir. Sin 5Hz	Y-1-90	65.49	0.83	42.64	0.99
6	X dir. impacts	X-1-90	4.39	0.89	11.14	1.00
6	X dir. impacts	Y-1-90	6.52	0.85	41.62	0.89
7	VAR dir. Sin 15Hz	X-1-90	16.46	0.96	44.07	0.98
7	VAR dir. Sin 15Hz	Y-1-90	64.35	0.94	27.79	1.00
7	VAR dir. Sin 5Hz	X-1-90	10.50	0.83	6.86	0.99
7	VAR dir. Sin 5Hz	Y-1-90	65.49	0.83	32.68	0.99
7	X dir. impacts	X-1-90	4.39	0.89	14.07	0.99
7	X dir. impacts	Y-1-90	6.52	0.85	29.42	0.90
8	VAR dir. Sin 15Hz	X-1-90	16.46	0.96	9.39	0.94
8	VAR dir. Sin 15Hz	Y-1-90	64.35	0.94	33.89	0.98
8	VAR dir. Sin 5Hz	X-1-90	10.50	0.83	3.15	0.88
8	VAR dir. Sin 5Hz	Y-1-90	65.49	0.83	10.48	0.99
8	X dir. impacts	X-1-90	4.39	0.89	0.23	1.00
8	X dir. impacts	Y-1-90	6.52	0.85	4.38	0.93
9	VAR dir. Sin 15Hz	X-1-90	16.46	0.96	41.33	0.98
9	VAR dir. Sin 15Hz	Y-1-90	64.35	0.94	28.84	0.77
9	VAR dir. Sin 5Hz	X-1-90	10.50	0.83	0.17	0.99

9	VAR dir. Sin 5Hz	Y-1-90	65.49	0.83	60.95	0.21
9	X dir. impacts	X-1-90	4.39	0.89	7.22	0.99
9	X dir. impacts	Y-1-90	6.52	0.85	26.23	0.85
10	VAR dir. Sin 15Hz	X-1-90	16.46	0.96	111.59	0.33
10	VAR dir. Sin 15Hz	Y-1-90	64.35	0.94	9.17	0.47
10	VAR dir. Sin 5Hz	X-1-90	10.50	0.83	181.63	0.52
10	VAR dir. Sin 5Hz	Y-1-90	65.49	0.83	46.50	0.02
10	X dir. impacts	X-1-90	4.39	0.89	35.36	0.97
10	X dir. impacts	Y-1-90	6.52	0.85	21.33	0.83
11	VAR dir. Sin 15Hz	X-1-90	37.96	0.99	64.20	0.95
11	VAR dir. Sin 15Hz	Y-1-90	74.06	0.94	53.03	0.97
11	VAR dir. Sin 5Hz	X-1-90	64.99	0.70	64.82	0.69
11	VAR dir. Sin 5Hz	Y-1-90	74.89	0.75	82.55	0.43
11	X dir. impacts	X-1-90	21.84	0.89	20.23	0.90
11	X dir. impacts	Y-1-90	21.22	0.93	56.09	0.94
12	VAR dir. Sin 15Hz	X-1-90	37.96	0.99	18.45	0.96
12	VAR dir. Sin 15Hz	Y-1-90	74.06	0.94	61.02	0.95
12	VAR dir. Sin 5Hz	X-1-90	64.99	0.70	27.02	0.81
12	VAR dir. Sin 5Hz	Y-1-90	74.89	0.75	77.22	0.71
12	X dir. impacts	X-1-90	21.84	0.89	1.78	0.91
12	X dir. impacts	Y-1-90	21.22	0.93	30.29	0.95

Table 4-20 R*esults obtained with sensor configurations 6 to 12 (strain gauges and accelerometer used as input sensors). Stochastic events.*

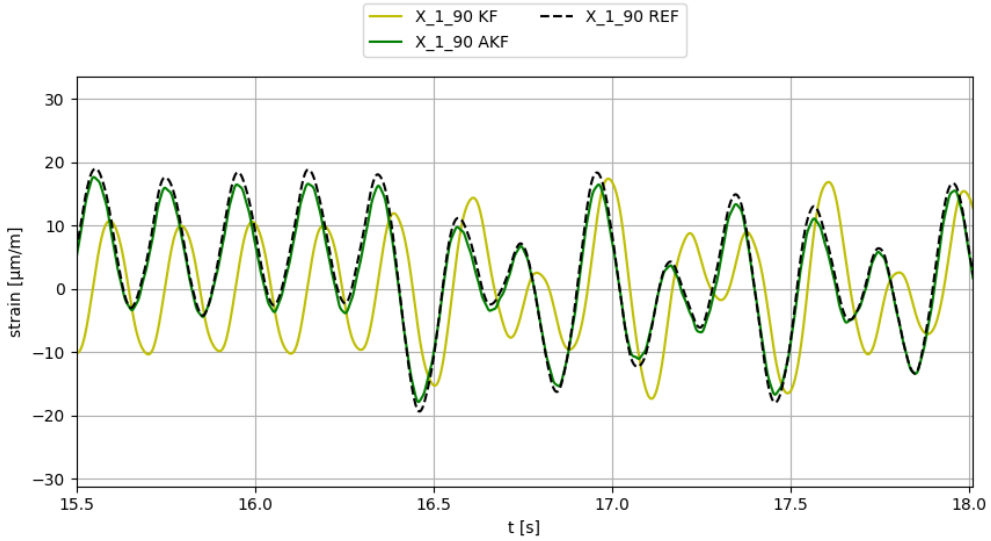

Figure 4-58 *Plot of results obtained at gauge X-1-90 using sensor config. 6, applying sin 5Hz force in variable direction.*

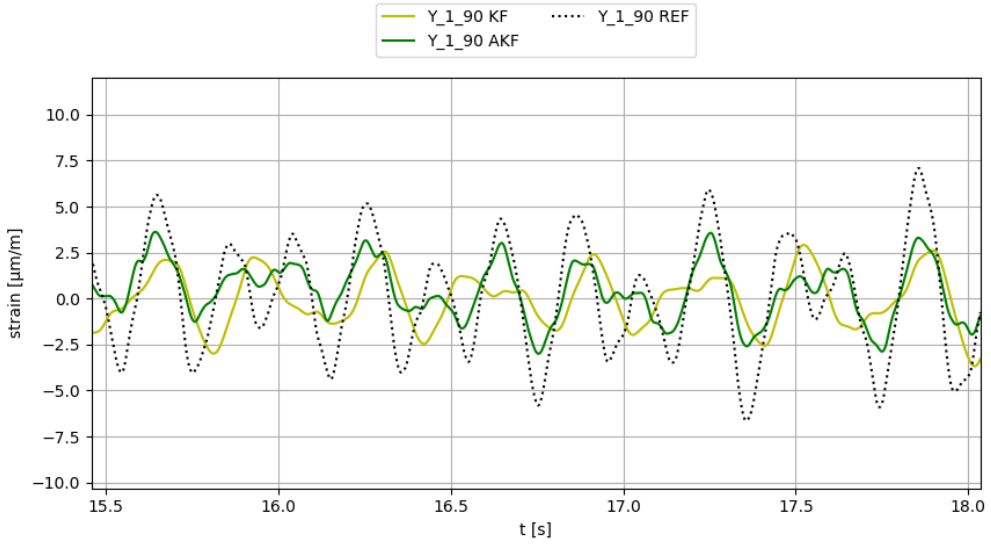

Figure 4-59 *Plot of results obtained at gauge Y-1-90 using sensor config. 6, applying sin 5Hz force in variable direction.*

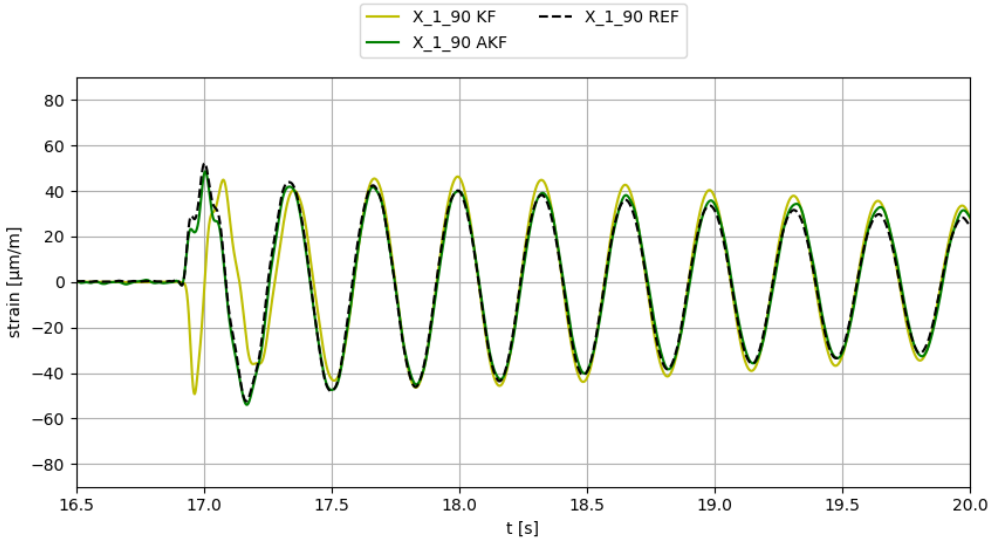

Figure 4-60 *Plot of results obtained at gauge X-1-90 using sensor config. 8, applying an impact in X direction.*

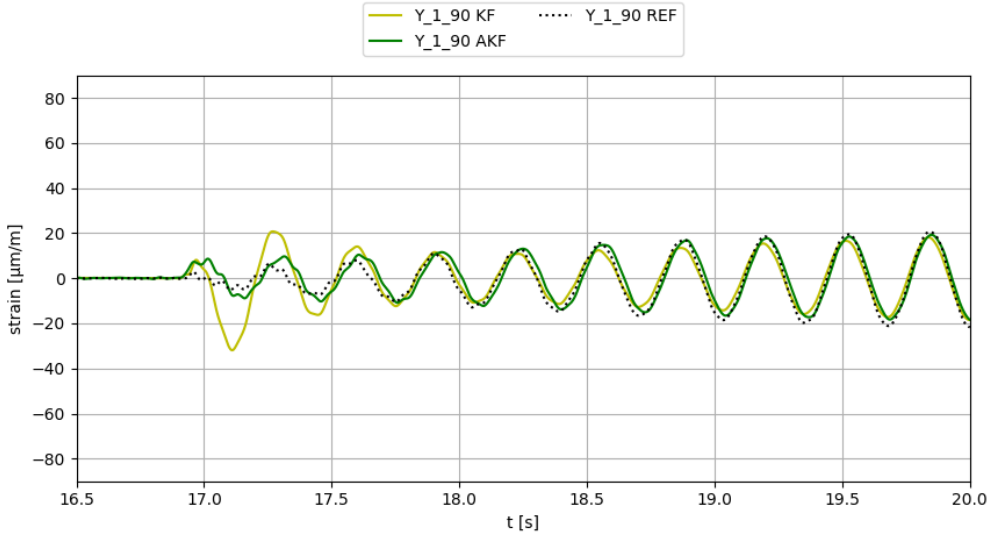

Figure 4-61 *Plot of results obtained at gauge Y-1-90 using sensor config. 8, applying an impact in X direction.*

In this study case, multiple experiments have been carried out with the OWT prototype. 12 sensor configurations have been tested with three different VS algorithms, under 6 different types of external forces and applied in different directions. In all tested cases, the same modal-truncated model with 4 modes has been used. Two strain virtual sensors have been implemented in the positions of the strain gauges X-1-90 and Y-1-90, with the aim of evaluating the performance of each VS algorithm in each of the experiments performed.

In first place, the results obtained with the sensor configurations that only use strain gauges as input sensors are commented. The first thing observed is that the performance of the three VS algorithms tested (KF, AKF and LSSE) is very similar in most cases. In some example plots, such as those that can be seen in **Figure 4-24**, **Figure 4-29** or **Figure 4-36**, differences between the responses of the three VS algorithms tested are practically imperceptible. In some other example plots, a certain difference can be observed between the responses of the tested algorithms, such as in the **Figure 4-25**, **Figure 4-32** or **Figure 4-38**.

One of the conclusions that can be obtained from analyzing the results is that there is no direct relation between the number of input sensors used and the quality of the results obtained. Another of the conclusions that can be obtained from the results is that not only the number of input sensors used, but also their position, has a significant impact on the quality of the results obtained.

In **Figure 4-62** it can be seen the evolution of the error present in the virtual measurements obtained as the number of input sensors is reduced, and as the present input sensors are moved further from the virtual sensors.

In the case of the KF, it can be observed that the average percent error increases as the number of input sensors is reduced, and also as these sensors are located further from the virtual sensors.

In the case of the AKF, the average percent error remains stable in the first three sensor configs., to increase significantly in the 4 and 5.

In the case of the LSSE, the average percent error reaches a minimum in sensor config 3, and then increases significantly in the following ones. This can be explained because, in this algorithm, the condition of the input matrix $\mathbf{G_i}$ is related to the quality of the estimates obtained, being possible that a specific sensor config. to has a lower condition number than others. **Table 4-21** shows the condition number of the different sensor configs. tested.

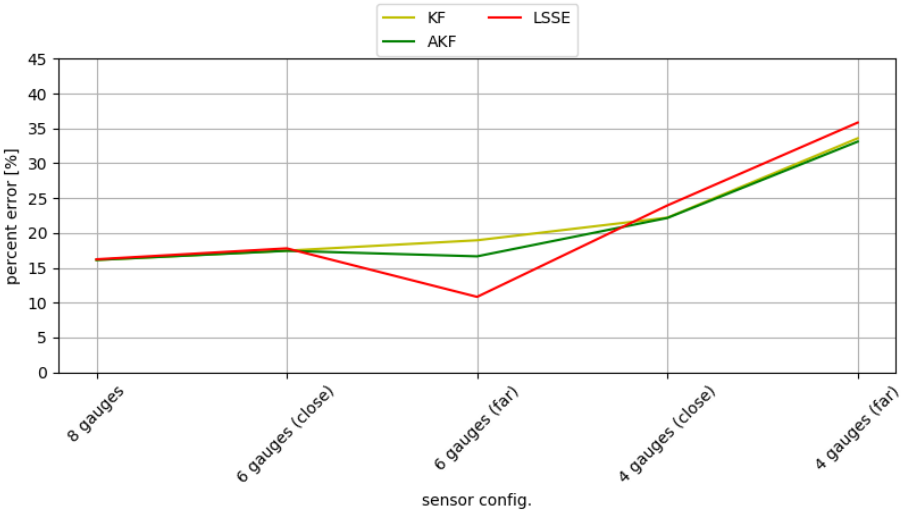

Figure 4-62 *Evolution of the percent error (averaged over all cases) as fewer input sensors are available. The adjective "close" refers to the fact that the gauges closest to the virtual sensors are used as input sensors (sensor configs. 2 and 4), and the adjective "far" refers to the fact that the gauges furthest from the virtual sensors are used as input sensors (sensor configs. 3 and 5)*

Sensor config.	**1**	**2**	**3**	**4**	**5**
Cond (G_i)	7.21	6.27	5.73	9.91	32.6

Table 4-21 *Evolution of cond(**Gi**) in the sensor configs. tested in the LSSE.*

If the results obtained with stochastic events are analyzed (see **Table 4-16**), it can be seen that the AKF and the LSSE can obtain good quality estimates both in the case of variable direction forces and in the case of sudden impacts. On the contrary, the KF shows a bigger divergence under some stochastic loads (as can be seen in **Figure 4-38** and **Figure 4-40**, for example).

In almost all the results obtained using the sensor configs. 1 to 5, PCCs (after delay compensation) are very high, with values above 0.9. This means that, regardless of whether the accuracy is higher or lower, the estimated signals are consistent with the input data, which indicates that there are no malfunctions in the VS algorithms used.

In second place, the results obtained with the sensor configurations that combines acceleration and strain measurements as input data, are commented. In this occasion, only the KF and the AKF algorithms can be tested, due to the LSSE is designed to work only with strain measurements as input data. The first thing observed in this case is an important difference between the results obtained with the KF and with the AKF.

The KF shows identical results for sensor configs. 6 to 10, and for sensor configs 11 to 12, in both cases with a high degree of error (as can be seen in **Figure 4-63**). If PCCs of the KF results are observed (see **Table 4-17**, **Table 4-18**, **Table 4-19** and **Table 4-20**) low values (under 0.9 and even under 0.8) can be seen in many of then. This indicates that the results offered by this algorithm are not very consistent with the input data, under the conditions of these experiments (that can be seen in **Figure 4-42**, **Figure 4-45** and **Figure 4-46**, for example).

The AKF offers estimations of considerably better quality than the KF in sensor configs 6 to 8, but error increases considerably in sensor configs. 9 to 12. If PCCs of the AKF results are observed, high values (over 0.9) can be seen in sensor configs. 6 to 8 (which indicates consistent results) per lower values can be seen from sensor config 9 onwards.

As seen in the results of the VS algorithms with sensor configs 1 to 5, in this case with the AKF it is also seen that there is no direct relation between the number of input sensors used and the quality of the obtained results: in fact, better results have been obtained with sensor configs. 7 and 8 than with sensor config 6.

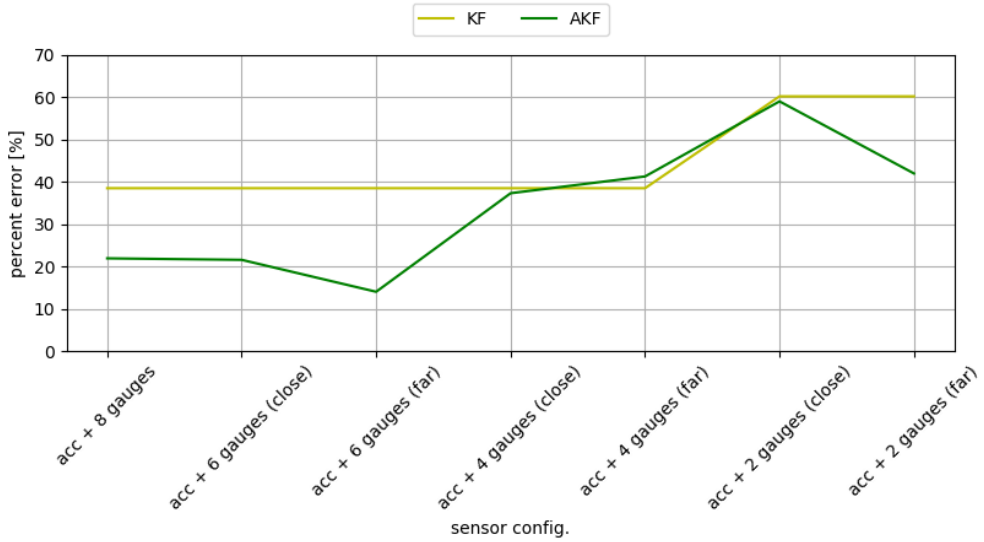

Figure 4-63 *Evolution of the percent error (averaged over cases with X, Y and XY direction forces applied) as fewer input sensors are available. The same accelerometer (with three channels) is present in all sensor configs. The adjective "close" refers to the fact that the gauges closest to the virtual sensors are used as input sensors (sensor configs. 7, 9 and 11), and the adjective "far" refers to the fact that the gauges furthest from the virtual sensors are used as input sensors (sensor configs. 8, 10 and 12)*

In third and last place, the obtained results are evaluated globally. The **Table 4-22** shows the averaged results of each VS algorithm tested for each sensor config. used. The results obtained with the forces applied in X, Y and XY directions are used to obtain the averaged results.

VS algorithm:

Sensor config.	KF		AKF		LSSE	
	e%	**PCC**	**e%**	**PCC**	**e%**	**PCC**
1	16.13	1.00	16.13	1.00	16.23	1.00
2	17.47	1.00	17.44	1.00	17.79	0.99
3	18.95	0.97	16.65	0.97	10.83	1.00
4	22.21	0.99	22.16	0.99	23.96	0.99
5	33.60	0.94	33.12	0.95	35.85	0.90
6	38.51	0.83	21.95	0.99	-	-
7	38.51	0.83	21.59	0.99	-	-
8	38.51	0.83	14.05	0.95	-	-
9	38.51	0.83	37.33	0.92	-	-
10	38.51	0.83	41.29	0.78	-	-
11	60.21	0.76	59.03	0.81	-	-
12	60.21	0.76	41.99	0.83	-	-

Table 4-22 *Global results obtained (averaged over cases with X, Y and XY direction forces applied). The better estimations obtained for each VS algorithms are remarked in green.*

The first conclusion reached after analyzing the global results is that, in the conditions in which this study case is carried out (unmeasured external loads, and strain estimation as the objective of virtual sensors), the addition of an accelerometer to the input sensors does not provide any benefit. In the case of the KF the quality of estimates is significantly reduced. In the case of the AKF, in some specific experiments there are slight improvements and in others slight worsening, with no overall improvement perceived (as can be seen in **Table 4-23**).

External forces	Virtual sensor	AKF with sensor config 3 e%	AKF with sensor config 8 e%
XY dir. Noise	X-1-90	18.82	14.67
XY dir. Noise	Y-1-90	10.98	30.48
XY dir. Sin 10Hz	X-1-90	1.61	12.33
XY dir. Sin 10Hz	Y-1-90	37.17	29.34
XY dir. Sin 15Hz	X-1-90	69.55	19.71
XY dir. Sin 15Hz	Y-1-90	14.09	40.72
XY dir. Sin 2Hz	X-1-90	19.68	9.30
XY dir. Sin 2Hz	Y-1-90	10.48	11.51
XY dir. Sin 5Hz	X-1-90	40.88	10.89
XY dir. Sin 5Hz	Y-1-90	4.72	13.82
VAR dir. Sin 15Hz	X-1-90	10.67	9.39
VAR dir. Sin 15Hz	Y-1-90	7.11	33.89
VAR dir. Sin 5Hz	X-1-90	29.30	3.15
VAR dir. Sin 5Hz	Y-1-90	2.52	10.48
X dir. impacts	X-1-90	11.67	0.23
X dir. impacts	Y-1-90	1.70	4.38

Table 4-23 *Comparison experiment by experiment between the results obtained with the AKF: sensor config 3 vs sensor config 8. The better estimation obtained for each experiment is remarked in green.*

Study case 1

Between the KF and the AKF algorithms, in the conditions of this study case is preferable to choose the AKF, because it improves the operation of the KF without having any disadvantage compared to it.

Due to, as mentioned above, the addition of accelerometers as input sensors does not improve in the quality of the estimates, it is concluded that the best way to obtain virtual strain measurements is using only strain sensors as input sensors. Taking this into account, both the use of AKF and LSSE are good alternatives, since both provide very similar results when the same sensor configs. are used. It should be taken into account that the LSSE is an algorithm simpler to program and faster to execute than the AKF.

When implementing the LSSE for strain/stress virtual sensing, it can be concluded that it is not preferable to have as many input sensors as possible, but rather to implement a configuration of input sensors that minimize cond(**Gi**) (see equation 2-42).

It is also a notable conclusion that using a reduced model using modal truncation and a reduced number of modes (those within the frequency range that is intended to be excited, 4 in this study case) allows to accurately recreate the behavior of a complex structure (such as the OWT prototype) when static, quasistatic and dynamic loads of different nature and different direction are applied.

Chapter 5
STUDY CASE 2

5.1 Experiment description

The study case 2 consists of a scaled prototype of the bed of an industrial press. The bed of a press is a component that consists of the lower part of the complete structure of the machine (see **Figure 5-1**) and must resist significant stress consequence of the load cycles due to the operation of the press. Generally, a press bed is made of welded steel plates. Due to the load cycles suffered, fatigue damage can occur in stress concentration areas, such as welded joints.

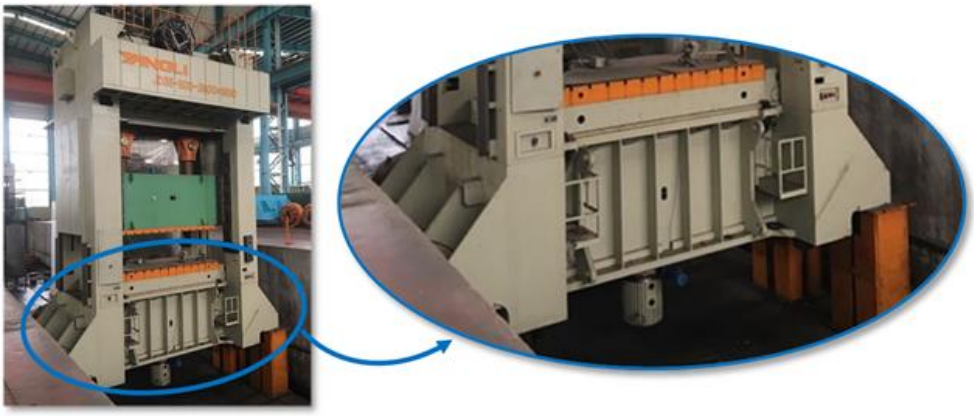

Figure 5-1 *Industrial press, with a detailed view of the bed. Source: https://yanglipress.com/products/*

The scaled prototype used in this section is a simplification of the bed of an industrial press (see **Figure 5-2**). It is built with three steel plates welded together, forming an inverted U-shape. Inside the prototype, three reinforcement bars are welded to increase the main stiffness of the prototype. The three main plates are welded with geometric preparation V-groove type (see **Figure 5-3**) and the reinforcement bars are welded to the main plates with full penetration filled welds (see **Figure 5-4**).

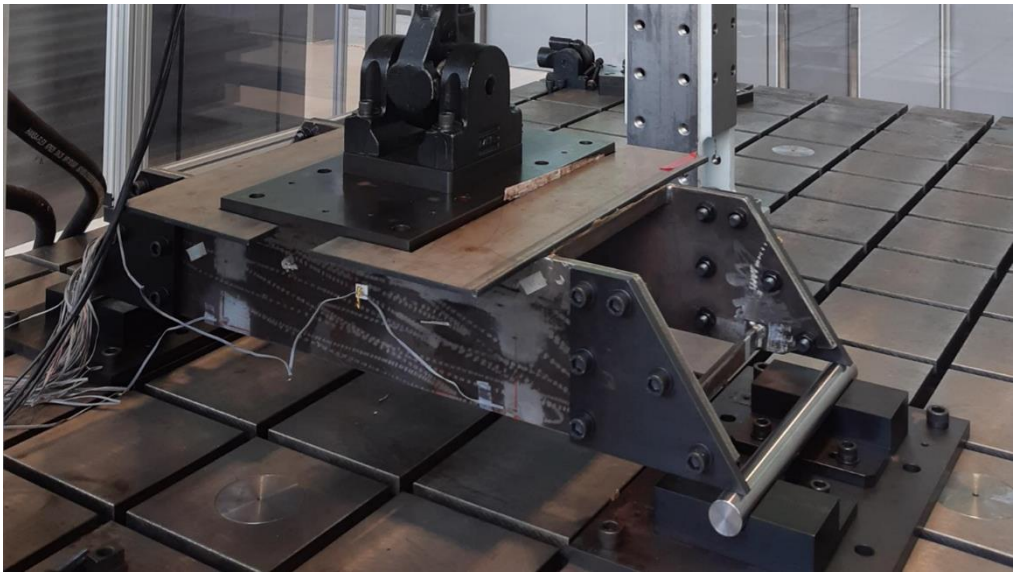

Figure 5-2 *Scaled prototype of a press bed used in this section as study case.*

Figure 5-3 *Welded joint between two main plates.*

Figure 5-4 *Welded joint a reinforcement bar and a main plate.*

The supports of the scaled prototype originally consisted of four rounded slots (in each corner of the prototype), which fit into four corresponding pieces of the same shape (see **Figure 5-5**). After a first test, it was observed that these supports were not working properly, so they were redesigned. The new supports consist of four steel plates, screwed in the four corners of the prototype, that rest on two metal bars (see **Figure 5-6**).

Figure 5-5 *Original slot-piece supports.*

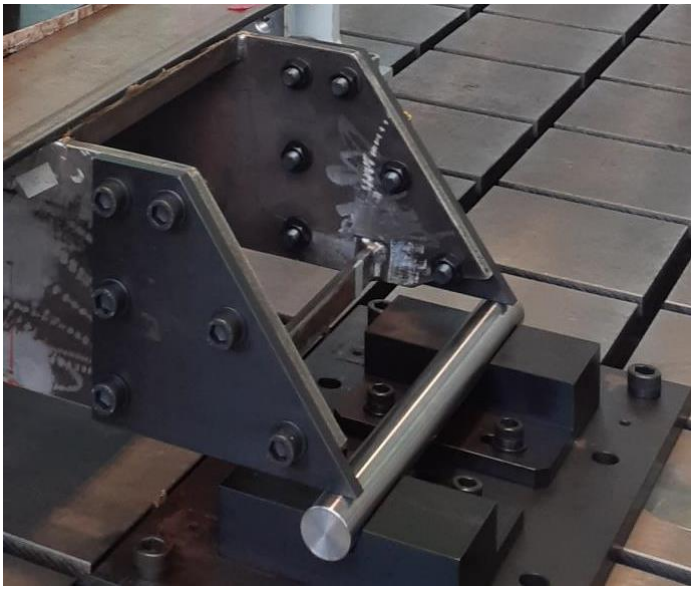

Figure 5-6 *Redesigned supports.*

The main features of the scaled prototype (including weight, dimensions, and material) are collected in **Table 5-1**.

Characteristic	Value
Weight	127 kg
Length	1120 mm
Height	210 mm
Width	410 mm
Main plates thickness	15 mm
Reinforcement bars thickness	10 mm
Material	Steel S-275

Table 5-1 *Main features of the scaled prototype.*

Study case 2

A fatigue test is performed with the prototype in order to replicate the operating conditions of a real press. For this purpose, is used a large-scale fatigue testing machine consisting of a steel frame with a hydraulic piston (installed vertically) capable of generating a force of up to 150 kN (see **Figure 5-7**). During the fatigue test, compressive cyclic loads are applied at the top of the prototype, simulating the stamping operation of a real press. The characteristics of the fatigue test performed are collected in **Table 5-2**. The experiment is performed in a laboratory of Ikerlan.

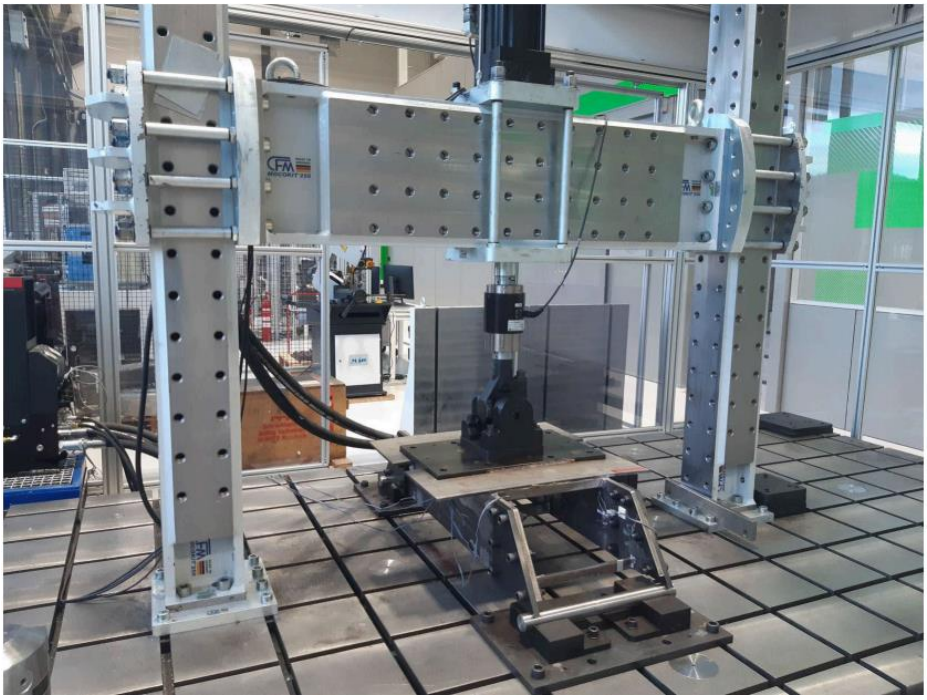

Figure 5-7 *Fatigue test machine used in the study case 2.*

Feature	Value
Type	Sinusoidal
Max load	150 kN
Min load	15 kN
Stress ratio (R)	0.1
Mean load	82.5 kN
Frequency	3 Hz

Table 5-2 *Main characteristics of the performed fatigue test.*

The applied load cycles have sufficient amplitude to cause fatigue damage at the critical points of the prototype. During the experiment, the prototype is sensorized using two sets of strain gauges. One set consist of those gauges used as input sensors, used to obtain real measurement data to feed the implemented VS algorithms. The other set consist of reference sensors, used only to check if the performance of the VS algorithms is correct. The exact number and location of the installed sensors, as well as the criteria used, is discussed in subchapter 5.3.

A 3D CAD model of the press bed prototype is created. The model includes all the details of the prototype, including the weldings (see **Figure 5-8**). The model also includes the two steel bars on which the prototype rests and the supports of the bars, and a steel plate connected to the piston of the fatigue machine through which the loads are applied.

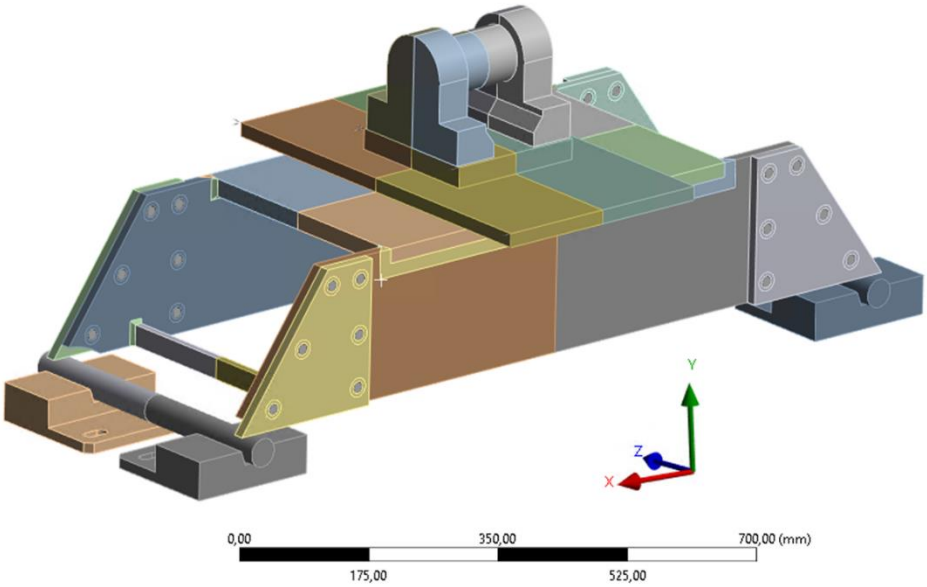

Figure 5-8 *CAD model of the press bed prototype.*

A FEM model is generated from the CAD model. A dense mesh is used, to accurately estimate strain and stress at all zones of the prototype, specially near the welded joints. External components that are not part of the prototype are meshed with thicker elements. All contacts are properly defined to generate adequate boundary conditions. The main characteristics of the FEM model are collected in **Table 5-3**.

Feature	Value
Number of elements	2,140,000
Element order	Quadratic
Element size	Variable, generally 5mm.
Contacts with support bars	Frictional
Contacts with upper steel plate	Frictional

Table 5-3 *Main characteristics of the generated FEM model.*

Once the FEM model is created, it is used to perform a static simulation with the aim of identifying the critical points of the prototype. In the simulation, a 150kN force (similar to the maximum force applied during the fatigue test) is applied at the top of the model. It is observed that the model bends along the X axis, so two different magnitudes are plotted: Von Mises stress and normal stress in X direction. The results can be seen in **Figure 5-9**. Two critical points are identified: A and B.

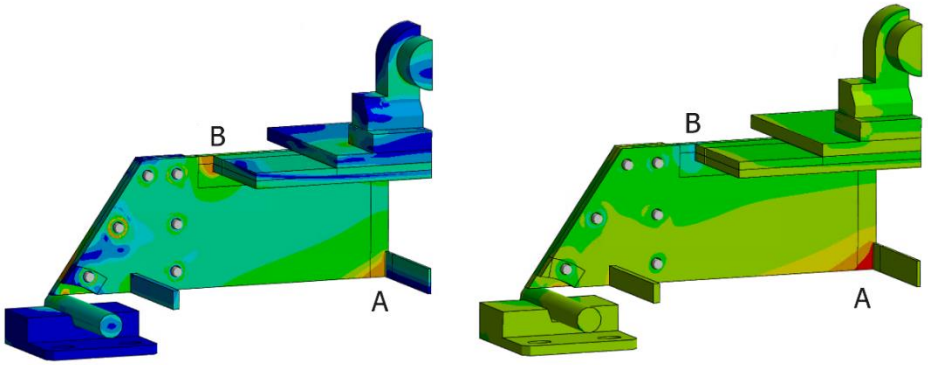

Figure 5-9 *Distribution of Von Misses stress (left) and normal Y-direction stress (right) in the model. Cut view. Identified critical points A and B are shown.*

Both critical points correspond to welded joints, so HSS method is used to determine the maximum stress to which they are subjected, and thus determine which of both is the most critical. Both critical points are located on the surface of main plates, so they are considered type A hot spots.

Study case 2

The critical point A correspond to a transverse attachment, with two-sided filled welds, not thicker than main plate (no. of detail 511 in the IIW guide [113]). The critical point B correspond to a single sided T-joint (no. of detail 411 in the IIW guide).

Some correction factors are applied to the selected FAT class: the stress ratio factor and the wall thickness factor. In the case of the stress ratio factor f(R), the case III is selected (of the possible ones presented by the IIW guide), which assumes f(R)=1. In the case of the wall thickness factor f(t), the equation 5-1 is used. t_{ref} is 25mm and t_{eff} is the thickness of the plate where the critical point is located. For the exponent, n=0.2 is used (according to the categories exposed in the IIW guide). For both critical points, t_{eff}=15 mm.

$$f(t) = \left(\frac{t_{ref}}{t_{eff}}\right)^{n} \qquad 5\text{-}1$$

The main characteristics of the A and B critical points, and their estimated number of cycles for crack initiation (using equation 3-14) are shown in **Table 5-4**. After analyzing both points using HSS, it is deduced that point B (see **Figure 5-10**) is the most critical point, and therefore, is the point chosen to be monitored because is where a crack is expected to initiate during the experiment. The FAT curve corresponding to point B is remarked in **Figure 5-11**.

Point	HS type	Detail no.	HSS [MPa]	FAT	FAT corrected	Nº cycles for crack initiation
A	A	511	167.8	100	110.8	575,000
B	A	411	174.5	90	99.7	370,000

Table 5-4 *Characteristics of the selected critical points.*

Because the prototype is doubly symmetrical, it contains 4 points B, one for each corner: B-1, B-3, B-4, and B-5.

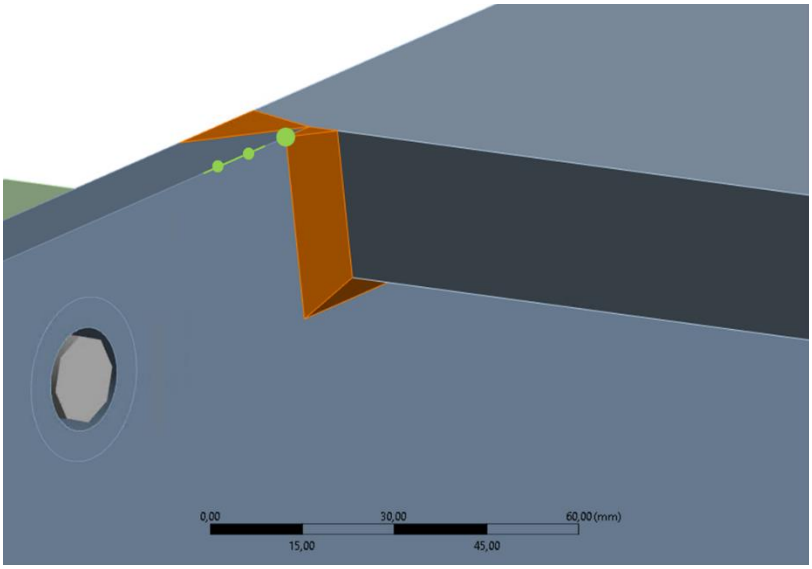

Figure 5-10 *Detailed view of the welded joint where critical point B is located. The HSS is remarked in green.*

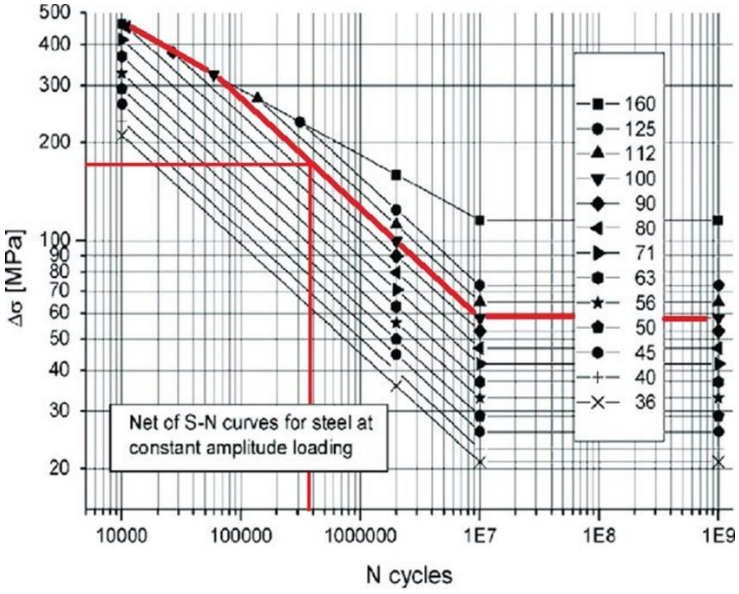

Figure 5-11 *FAT curve for the critical point B remarked in red.*

5.3. Sensors

To carry out the experiment of the study case 2, the prototype is sensorized using strain gauges, to be used as input sensors for the later implemented VS algorithms. The location of these sensors is chosen following two criteria: to be accessible points and to be points that experiment significant deformation under the applied cyclic loads. Four strain gauges are installed: gauge 1, gauge 3, gauge 4 and gauge 5 (following the same numeration criteria as with the four critical points). The selected 4 points are accessible in the case of a real press in operation, because they are located on the outside of the frame of the bed press. Also, according to the static simulation performed with the FEM model, the selected 4 points suffer significant deformation when the max load is applied.

To monitor the four corners of the prototype with four independent strain gauges allows to study each of the 4 selected critical points separately, with the objective to estimate (using VS algorithms) the critical point of the four possibles where the crack initiation is expected to occur.

For the implementation of virtual sensors, the strategy described below is used: on one hand, virtual sensors are implemented at points where real strain gauges are also installed. These sensors are called REF sensors, and they are used to verify the proper operation of the implemented VS algorithms. On the other hand, other virtual sensors are implemented at points where real sensors are not installed, due to the unfeasibility.

In the experiment carried out in this study case, two REF sensors are implemented: gauge 2-REF and gauge 6-REF. Other four non-referenced virtual sensors are implemented in the critical points B-1, B-3, B-4, and B-5. The position of the real sensors is described in **Figure 5-12**.

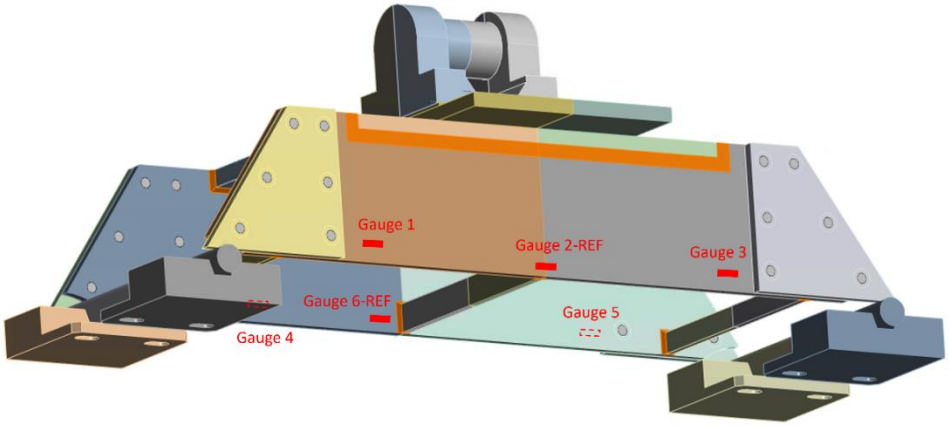

Figure 5-12 *Location of the real strain gauges in the prototype.*

In addition to the strain gauges, the measurement of the force applied by the piston of the fatigue test machine is available. This force measurement can be used both to verify that the applied force by the piston is correct, and as input sensor for some VS algorithms. Even so, in this case study it is preferred not to use external force measures as input measurements in the implemented VS.

During the experiment, sensor data is collected using a National Instruments data acquisition system, in combination with LabView. A NI CompactDAQ-9189 rack (with 8 slots) and NI-9235 acquisition cards are used for reading the installed strain gauges.

5.4. Expected uncertainties.

In the experiment carried out on this study case, different uncertainties are expected, that are listed and commented in this subchapter.

In first place, geometric and manufacturing imperfections may cause certain behavior differences between the real prototype and the FEM model. Small differences in the symmetry of the prototype can lead to slight strain differences between the different corners. The quality of the welds (hand-made in the case of the used prototype, see **Figure 5-3** and **Figure 5-4**) can have a greater impact, both in the difference in stiffness between the different corners of the prototype (and consequently, differences in the measured strain) and in the fatigue life of the critical points. Poor quality welds can suppose a significant decrease of the fatigue life of the prototype.

Because simple cylindrical supports are used (without guides or notches, see **Figure 5-6**), involuntary irregularities in the placement of the prototype or small undesired displacements that may occur during the test can suppose certain degree of uncertainty in the strain measurements.

Possible errors in the installation of the strain gauges, both in the exact position of the sensors and in their orientation, can also imply certain degree of uncertainty in the obtained strain measurements.

Regarding the fatigue test machine, the force applied by the piston and its displacement are measured in real time by sensors integrated into the machine, and no significant uncertainties are expected due to this. Otherwise, centring errors in the force application can be a source of uncertainty, but to minimize this problem, steel guides have been installed in the prototype to minimize possible decentring in the applied loads.

5.5. Implemented VS algorithms.

In the study case 2, three VS algorithms are implemented: direct observer, LSSE and SSKF.

This study case has two peculiarities compared to the previous study case. First, only strain gauges are used in this experiment as input sensors, as well as a load measurement provided by the fatigue test machine (which its use is intended to be minimized). Besides, only quasistatic loads are applied in this experiment, so it is not expected to cause dynamic effects in the prototype. These peculiarities are taken into account when choosing and implementing VS algorithms in this study case.

In the case of the direct observer, the load signal obtained from the fatigue test machine is used as input sensor. A static reduced model consisting of a Guyan reduced **K** matrix is created and using equation 2-41, the displacements of the selected master nodes (corresponding to the positions of gauges 1, 3, 4 and 5) are obtained. The diagonal values for **Q** and **R** covariance matrices are 1E-6. Using a strain matrix **G** (see equation 2-39), the strain at REF points (2 and 6) is estimated. The strain at critical points B-1, B-3, B-4, and B-5 is not estimated in this case, because this algorithm does not allow to identify the differences between the critical points.

In the case of the LSSE, the strain gauges 1, 3, 4 and 5 are used as input sensors and, therefore, incorporated in the half-matrix $\mathbf{G_i}$ (see equation 2-42). Strain estimations are obtained at the points REF (2 and 6) and at the critical points (B-1, B-3, B-4, and B-5), so these points are incorporated in the half-matrix $\mathbf{G_{VS}}$ (see equation 2-43).

The **G** matrix is created using a SMR model that contains three SDS. The first SDS corresponds to a deformation shape generated applying a centered load. The second and third SDSs correspond to deformation shapes generated applying slightly decentered forces (along the X and Z axis). By using more than one SDSs, it is

intended to capture the strain differences between critical points B-1, B-3, B-4, and B-5, and therefore, estimate at which of these points a crack will initiate.

In the case of the SSKF, a state-space model with three states is used (obtained from the SMR model with three SDS used in the LSSE). Each state of the model corresponds to an SDS. The strain gauges 1, 3, 4 and 5 are used as input sensors, being the observation matrix **H** the same half-matrix $\mathbf{G_i}$ used in the LSSE. Strain estimations are obtained at the points REF (2 and 6) and at the critical points (B-1, B-3, B-4, and B-5) using the outputs matrix **C**, corresponding to the same half-matrix $\mathbf{G_{VS}}$ used in the LSSE.

5.6. Results

In this subchapter, the VS results obtained in the study case 2 are presented. In a first phase, the virtual strains obtained at the REF points (2 and 6) are compared with the real measurements from gauge 2-REF (see **Figure 5-13** and **Table 5-5**) and gauge 6-REF (see **Figure 5-14** and **Table 5-6**).

The e. mean, e. range, and RRMSE are the indicators selected to compare the virtual measurements estimated at the REF points with the real measurements obtained from the REF strain gauges installed at these same points (gauge 2-REF and gauge 6-REF).

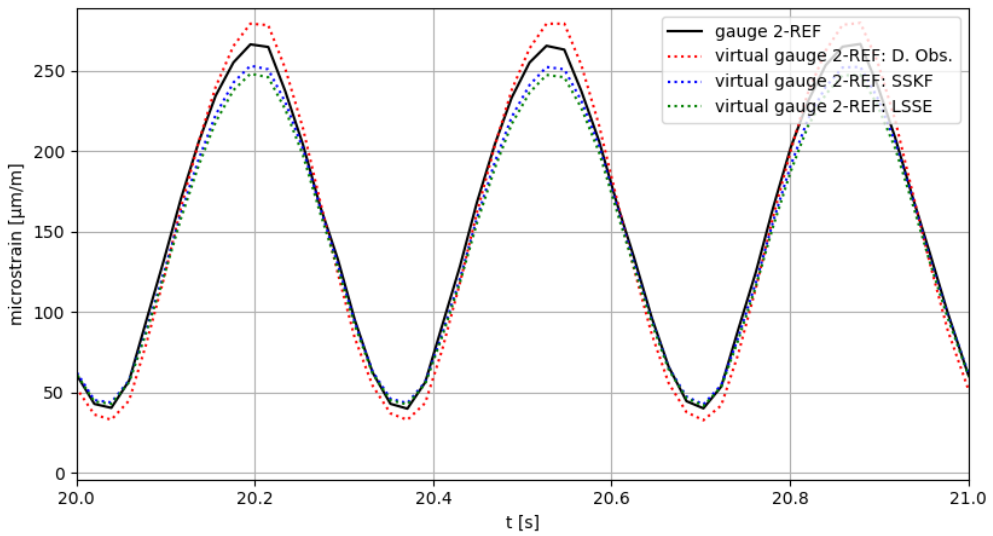

Figure 5-13 *Plot of virtual strain measurements obtained at gauge 2-REF, compared with the real signal.*

D. Obs.			SSKF			LSSE		
RRMSE [%]	**e. mean [%]**	**e. range [%]**	**RRMSE [%]**	**e. mean [%]**	**e. range [%]**	**RRMSE [%]**	**e. mean [%]**	**e. range [%]**
6.6	0.6	7.5	7.0	5.6	10.1	6.8	5.5	8.1

Table 5-5 *Results of virtual strain measurements obtained at gauge 2-REF, compared with the real signal.*

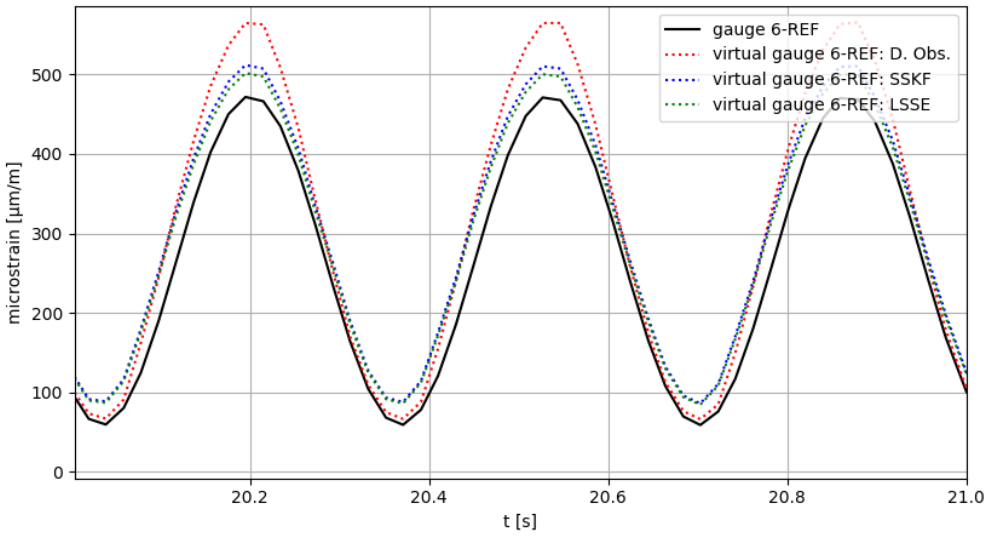

Figure 5-14 *Plot of virtual strain measurements obtained at gauge 6-REF, compared with the real signal.*

D. Obs.			SSKF			LSSE		
RRMSE [%]	**e. mean [%]**	**e. range [%]**	**RRMSE [%]**	**e. mean [%]**	**e. range [%]**	**RRMSE [%]**	**e. mean [%]**	**e. range [%]**
22.1	18.1	21.2	13.4	12.1	1.8	13.3	12.2	1.3

Table 5-6 *Results of virtual strain measurements obtained at gauge 6-REF, compared with the real signal*

In a second phase, the virtual strain measurements obtained at the critical points B-1, B-3, B-4, and B-5 are used to estimate the HSS at those same points. With the estimated stress, the number of cycles to reach damage 1 (which implies crack-initiation) is calculated. The critical point (of the four possible) with the lowest number of cycles to reach damage 1 is the point where the crack is expected to initiate. As explained previously, only the LSSE and SSKF are able to work with the strain differences between the critical points.

Because real gauges can not be installed at the locations of the critical points due to feasibility reasons, it is not possible to compare the virtual measurements obtained at these points with equivalent real measurements. Therefore, these virtual sensors are validated by comparing the estimated number of cycles for crack-initiation with the experimental results.

Algorithm	**Number of cycles for crack initiation**			
	B-1	**B-3**	**B-4**	**B-5**
DSO	258,000			
SSKF	301,000	332,000	496,000	486,000
LSSE	300,000	331,000	495,000	485,000

Table 5-7 *Comparison of the estimated number of cycles for crack initiation between the different VS algorithms tested.*

The number of cycles for crack initiation estimated with the VS algorithms are compared with the experimental results for validation. It can be seen in **Figure 5-15** the evolution of the range values of the measured strain during the fatigue test. From the results, three phases can be differentiated: in the first phase (between n=0 and n=300,000 cycles), a stable behavior of the prototype can be observed, so this phase can be associated with the damage accumulation prior to crack initiation. In the second phase (between n=300,000 and n=400,000), a sudden change in the behavior of the prototype is captured by the gauges, that can be associated with the appearance

of a crack in one of the critical points. In the third phase (between n=400,000 and the end of the fatigue test) a slower process of change in the range values captured by the gauges can be observed, that can be associated with a crack growth process. In the **Figure 5-16** can be seen a comparison with the first phase and the third phase, in a plot that shows the loading and unloading phases of a load cycle. In the first phase, an approximately linear behavior can be observed in the four gauges. Instead, in the third phase, a hysteresis can be observed between the loading and unloading of a load cycle, which implies a change in the behavior of the prototype attributable to the appearance of a crack.

After stopping the fatigue test at n=1,150,000 cycles, a large crack is observed in the prototype, initiated from the welded joint corresponding with the critical point B-1. The crack can be seen in **Figure 5-17**.

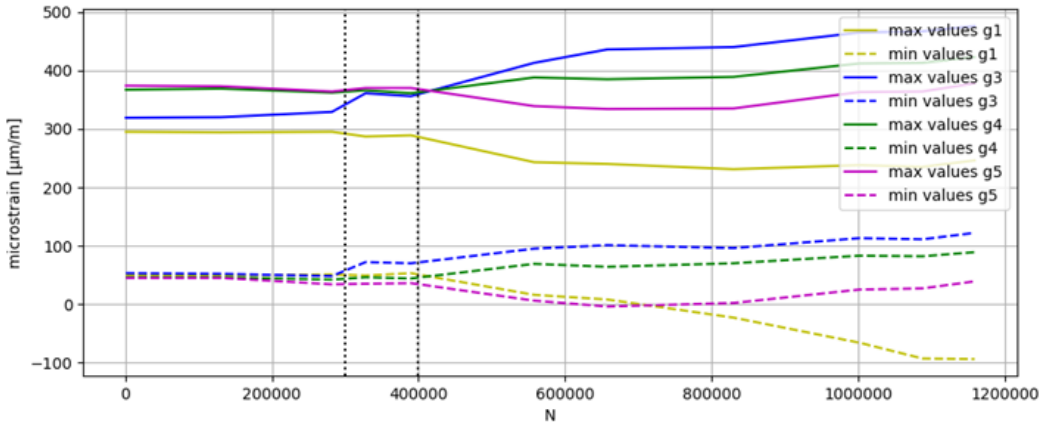

Figure 5-15 *Evolution of strain measured at gauges 1, 3 ,4 and 5 during the experiment. The range values of strain (max. and min.) are plotted. The two dashed vertical lines separate the three described phases.*

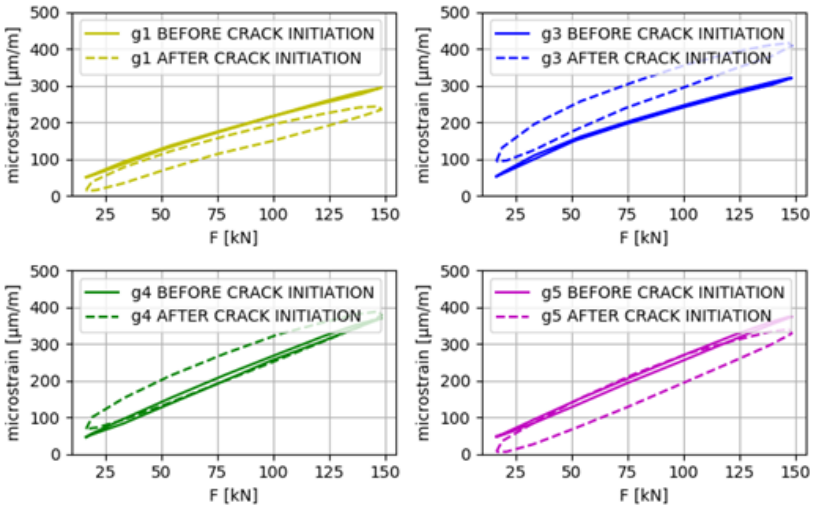

Figure 5-16 *Plot of applied load vs. measured strain at gauges 1, 3, 4 and 5. The loading and unloading phases can be seen. The continuous lines corresponds to a load cycle before crack initiation (n=130,000) and the dashed lines corresponds to a load cycle after a crack has initiated (n=550,000).*

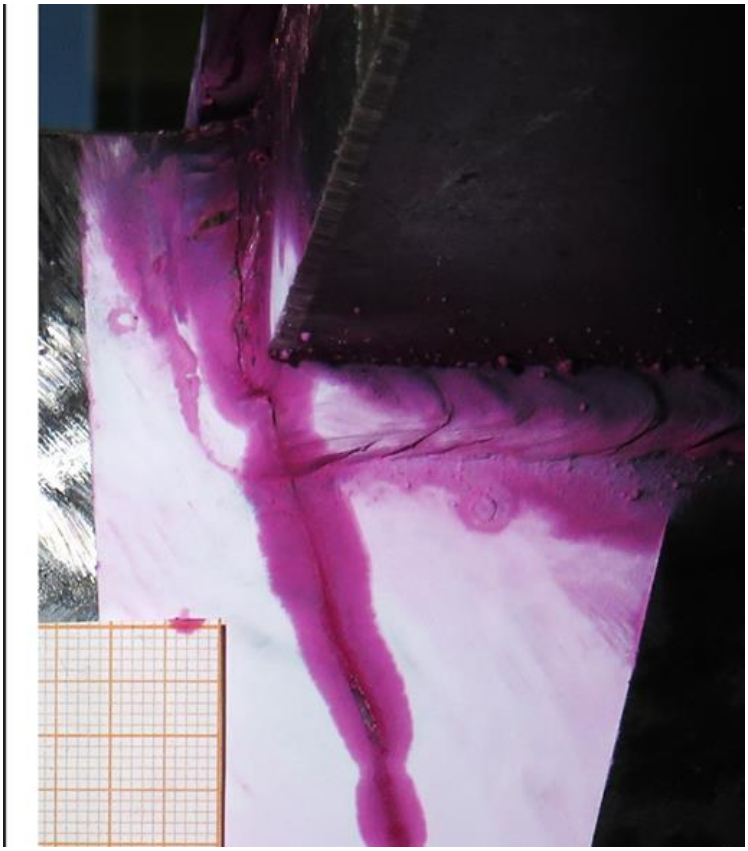

Figure 5-17 *Crack initiated at critical point B-1, highlighted with pink penetrating liquid. A millimeter scale is included as reference.*

5.7. Results discussion

In the first phase of the performed experiment, the implemented VS algorithms have been tested by comparing the virtual strain estimates with their corresponding real strain measurements at the REF points.

In the gauge 2-REF, very similar VS results are obtained with the three algorithms tested (the direct obs., the LSSE and the SSKF), very close to the reference signal (RRMSE below 10% in all cases), being the direct obs. the most accurate algorithm for this virtual gauge. In the gauge 6-REF, greater disparity can be observed in the VS results: the direct obs. offers worst results (with RRMSE above 20%) and the LSSE and SSKF improve the results significantly (with RRMSE below 15% in both cases).

In the second phase of the experiment, the virtual strain measurements at the critical points of the prototype are used to estimate the accumulated damage using the HSS method, in order to estimate the number of cycles until crack initiation. The FEM model gives an estimation of 370,000 cycles for crack initiation, being unable to differentiate between the different critical points of the prototype. The direct obs. is also not able to differentiate between the different critical points, therefore it only gives a generic estimation of 258,000 cycles. Both the LSSE and the SSKF give an estimation of approximately 300,000 cycles at critical point B-1.

The experimental results show that at critical point B-1 a crack has initiated between n=300,000 and n=400,000 cycles, therefore, the VS results obtained with the LSSE and the SSKF can be considered validated. On the other hand, the VS results obtained with the direct observer show certain degree of error, giving a number of cycles for crack initiation lower than the number estimated with the FEM model and than the number of obtained with experimental results.

Chapter 6

CONCLUSIONS

The main objective of this thesis has been set as to propose a methodology, and to adapt, test and evaluate different on VS algorithms for strain/stress estimation at unmeasured points of structural systems. In order to make a relevant contribution in the field of CM and SHM systems, this thesis focuses on the obtaining of strain/stress estimations when external loads measurements are not available, due to the complexity of obtaining load measurements in many cases.

Due to the fact that in this thesis virtual strain/stress sensors have been successfully implemented in several use cases, under conditions of unmeasured external loads, it can be concluded that its main objective has been achieved.

In subchapter *1.3*, five specific objectives have been also proposed, and the main conclusions for each specific objective are presented next.

The first objective has been to establish variants of existing VS algorithms, specifically oriented for strain/stress estimation in conditions of unmeasured external loads. Two VS algorithms have been adapted in this thesis: the SSKF (a stochastic model-based algorithm specifically designed for strain/stress estimation in cases of static/quasistatic loads, using only strain measurements as input data) and the LSSE (a deterministic model-based algorithm designed for strain/stress estimation using only strain measurements as input data, both in cases of static/quasistatic and dynamic loads). The LSSE have been successfully tested in the two use cases of this thesis, and the SSKF have been successfully tested in the second use case.

The second objective has been the implementation of different VS algorithms in different industrial applications, to study the feasibility of implementation of virtual sensors in different scenarios (with different requirements and needs). To achieve this objective, different VS algorithms have been implemented in two different scaled prototypes, representing two different cases of industrial applications (offshore wind turbines and industrial presses). In both use cases, satisfactory results have been obtained: reliable virtual strain/stress measurements have been obtained at unmeasured points of the monitored systems, without using external load

measurements. The virtual measurements have been validated using reference real measurements or with indirect methods (using fatigue cycle counting).

In the first study case, percent errors below 15% in the virtual strain sensors are obtained using some specific sensor configurations, and in the second study case, RRMSE below 15% in the virtual strain sensors are obtained.

Some weaknesses have been identified in the implementation of some of the VS algorithms with certain sensor configurations. For example, a malfunction on the KF has been detected when only strain gauges are used as input sensors.

The third objective has been the test of different VS algorithms under cases of quasistatic and dynamic loads. In the first use case (corresponding to the OWT scaled prototype), different dynamic loads (sinusoidal waves, random noise and impacts) have been applied in different directions (non-variable and variable along time) using an inertial shaker attached to the prototype. Adequate virtual strain measurements have been obtained using the KF, AKF and LSSE algorithms, a modal reduced model with 4 DoFs and a reduced number of strain measurements as input data. In the second use case (corresponding to the press bed scaled prototype), quasistatic cyclic loads have been applied to the prototype using a fatigue testing machine. Satisfactory virtual strain and stress measurements have been obtained using the SSKF and LSSE algorithms, a reduced model with 3 SDS as DoFs and a reduced number of strain measurements as input data.

The fourth objective has been the study of the possibility of using strain/stress measurements to calculate accumulated fatigue damage. The second use case (corresponding to the press bed scaled prototype) have been used for this purpose, first identifying its critical points using a FEM model and then implementing virtual sensors at these points. Using the SSKF and LSSE algorithms, a reduced model with 3 SDS as DoFs and a reduced number of strain measurements as input data, the most critical point (within a defined set of points) has been identified and the number of loading cycles until crack initiation has been estimated with satisfactory precision.

Both results have been experimentally validated. Some weaknesses have been identified in the implementation of the DSO, which shows greater inaccuracy in its results.

Among all VS algorithms tested in the two study cases carried out in this thesis, the proposed LSSE stands out for its simplicity of implementation, time of computation and flexibility. In most of the experiments performed, this algorithm provides similar results to those provided by the AKF or SSKF. Compared to these two, the LSSE has a much faster execution time (because, unlike KFs, it does not perform an inverse in each iteration), and it has no adjustment parameters (like the Q and R parameters of the KFs) which implies greater ease of implementation and use.

The fifth objective has been the creation of a software library (in open-source code) that contains the VS algorithms used in this thesis, facilitating its implementation in different types of structural systems and making easier transferring this technology to the industry. The *ikerlanVS.py* library has been developed in this thesis (using Python), which contains all the VS algorithms used in this thesis functionalized to be able to be adapted to different models and sensor configurations, plus some auxiliary functions.

The work presented in this thesis can be continued by following different research lines.

An interesting line to continue this work is to research in VS algorithms for external loads estimation. In the field of mechanical engineering, knowledge of external loads is of special interest. In the design or validation phases of machines or structures, to know the loads received by the system can be necessary to study the dynamic behavior, mechanical resistance, or safety of the system. In the operational phase of a system, for example in CM or SHM approaches, knowledge of external loads can be useful to apply a reconstruction of them in a model and be able to estimate accumulated fatigue or the degradation of the system due to damage. The direct measurement of external loads (using for example force transducers) is often

expensive, intrusive, or even unfeasible. Consequently, in many cases it is interesting not to directly measure the external loads, but to reconstruct them using other measurements, then using a VS approach.

Another interesting line to extend this work is to focus on using VS algorithms for detecting behavior anomalies in the monitored systems, which can indicate degradation or the apparition of damage in the system. With the detection of behavior changes, model updating can be performed, which consists of updating the parameters of the used model so that the model can reflect the evolution of the real system. This line of work is promising if it is integrated into more complex digital twin approaches. A possible example would be the use of virtual sensors for first crack detection and then crack growth monitoring in structural systems, helping to optimize maintenance and repairs on the system to increase safety and reduce costs.

BIBLIOGRAPHY

[1] S. Tewolde, R. Höffer, H. Haardt, and J. Krieger, “Structural Health Monitoring results as an input for asset management of offshore wind turbine support structures,” in *SMAR 2019- Fifth Conference on Smart Monitoring, Assessment and Rehabilitation of Civil Structures*, 2019, pp. 1–8.

[2] I. Antoniadou, N. Dervilis, E. Papatheou, A. E. Maguire, and K. Worden, “Aspects of structural health and condition monitoring of offshore wind turbines,” *Philosophical Transactions of the Royal Society A: Mathematical, Physical and Engineering Sciences*, vol. 373, no. 2035, 2015, doi: 10.1098/rsta.2014.0075.

[3] U. Leturiondo, “Hybrid Modelling in Condition Monitoring,” Lulea University of Technology, 2016.

[4] L. Zhou, F. Duan, D. Mba, W. Wang, and S. Ojolo, “Using frequency domain analysis techniques for diagnosis of planetary bearing defect in a CH-46E helicopter aft gearbox,” *Eng Fail Anal*, vol. 92, no. April, pp. 71–83, 2018, doi: 10.1016/j.engfailanal.2018.04.051.

[5] J. Schijve, “Fatigue of structures and materials in the 20th century and the state of the art,” *Int J Fatigue*, vol. 25, no. 8, pp. 679–702, 2003, doi: 10.1016/S0142-1123(03)00051-3.

[6] R. Reed, J. H. Smith, and B. W. Christ, “The Economic Effects of Fracture in the United States,” 1983. [Online]. Available: http://download.springer.com/static/pdf/590/art%3A10.1007%2FBF00028828.pdf?auth66=1412104181_6537bec9f5fbaf2d94003143decafcc5&ext=.pdf

[7] W. Rih-Teng and J. Mohammad Reza, “Data fusion approaches for structural health monitoring and system identification : Past , present , and future,” *SAGE: Structural Health Monitoring*, pp. 1–35, 2018, doi: 10.1177/1475921718798769.

[8] M. P. Limongelli *et al.*, “Lifecycle management, monitoring and assessment for safe large-scale infrastructures: Challenges and needs,” in *GEORES 2019 – 2nd International Conference of Geomatics and Restoration*, 2019, pp. 727–734. doi: 10.5194/isprs-Archives-XLII-2-W11-727-2019.

[9] C. P. Fritzen, P. Kraemer, and M. Klinkov, “An integrated SHM approach for offshore wind energy plants,” in *IMAC-XXVIII*, 2010, pp. 727–740. doi: 10.1007/978-1-4419-9834-7_63.

[10] D. M. Steinweg and M. Hornung, “Cost and Benefit of Scheduled Structural Health Monitoring for Commercial Aircraft,” in *32nd Congress of the International Council of the Aeronautical Sciences, ICAS 2021*, 2021, pp. 1–16.

[11] M. Martinez-Luengo and M. Shafiee, “Guidelines and cost-benefit analysis of the Structural Health Monitoring implementation in offshore wind turbine support structures,” *MDPI Energies*, vol. 12, no. 6, pp. 1–26, 2019, doi: 10.3390/en12061176.

[12] P. Avitabile and P. Pingle, “Prediction of full field dynamic strain from limited sets of measured data,” *Shock and Vibration*, vol. 19, pp. 765–785, 2012, doi: 10.3233/SAV-2012-0686.

[13] C. Papadimitriou, E. M. Lourens, G. Lombaert, G. De Roeck, and K. Liu, “Prediction of fatigue damage accumulation in metallic structures by the estimation of strains from operational vibrations,” in *Life-Cycle and Sustainability of Civil Infrastructure Systems - Proceedings of the 3rd International Symposium on Life-Cycle Civil Engineering, IALCCE 2012*, 2012, pp. 304–310.

[14] H. Xiao and L. Sen Chen, “Henky’s logarithmic strain and dual stress-strain and strain-stress relations in isotropic finite hyperelasticity,” *Int J Solids Struct*, vol. 40, no. 6, pp. 1455–1463, 2003, doi: 10.1016/S0020-7683(02)00653-4.

[15] G. Ballio and C. A. Castiglioni, “A unified approach for the design of steel structures under low and/or high cycle fatigue,” *J Constr Steel Res*, vol. 34, no. 1, pp. 75–101, 1995, doi: 10.1016/0143-974X(95)97297-B.

[16] L. Liu, S. M. Kuo, and M. C. Zhou, “Virtual sensing techniques and their applications,” in *IEEE International Conference on Networking, Sensing and Control 2009*, Okayama, Japan, 2009, pp. 31–36. doi: 10.1109/ICNSC.2009.4919241.

[17] K. Maes, A. Iliopoulos, W. Weijtjens, C. Devriendt, and G. Lombaert, “Dynamic strain estimation for fatigue assessment of an offshore monopile

wind turbine using filtering and modal expansion algorithms," *Mech Syst Signal Process*, vol. 76–77, pp. 592–611, 2016, doi: 10.1016/j.ymssp.2016.01.004.

[18] C. Papadimitriou, C. P. Fritzen, P. Kraemer, and E. Ntotsios, "Fatigue predictions in entire body of metallic structures from a limited number of vibration sensors using Kalman filtering," *Struct Control Health Monit*, vol. 18, no. 5, pp. 554–573, 2011, doi: 10.1002/stc.395.

[19] I. Ahmad, A. Ayub, M. Kano, and I. I. Cheema, "Gray-box soft sensors in process industry: Current practice, and future prospects in era of big data," *MDPI Processes*, vol. 8, no. 2, pp. 1–20, 2020, doi: 10.3390/pr8020243.

[20] S. Sun, Y. He, S. Zhou, and Z. Yue, "A Data-Driven Response Virtual Sensor Technique with Partial Vibration Measurements Using Convolutional Neural Network," *MDPI Sensors*, vol. 17, no. 2888, 2017, doi: 10.3390/s17122888.

[21] N. Shah, "Left and Right Neural Networks -Inspired by Our Bicameral Brains," 2019. [Online]. Available: https://www.researchgate.net/publication/337186250_Left_and_Right_Neural_Networks_-Inspired_by_Our_Bicameral_Brains

[22] B. Azzam, R. Schelenz, B. Roscher, A. Baseer, and G. Jacobs, "Development of a wind turbine gearbox virtual load sensor using multibody simulation and artificial neural networks," *Forschung im Ingenieurwesen/Engineering Research*, vol. 85, no. 2, pp. 241–250, 2021, doi: 10.1007/s10010-021-00460-3.

[23] B. Puruncajas, Y. Vidal, and C. Tutivén, "Vibration-response-only structural health monitoring for offshore wind turbine jacket foundations via convolutional neural networks," *MDPI Sensors*, vol. 20, no. 12, pp. 1–19, 2020, doi: 10.3390/s20123429.

[24] D. M. Polanski and C. M. Angelopoulos, "Modelling Virtual Sensors for Indoor Environments with Machine Learning," *Proceedings - 18th Annual International Conference on Distributed Computing in Sensor Systems, DCOSS 2022*, pp. 222–228, 2022, doi: 10.1109/DCOSS54816.2022.00046.

[25] B. Lin, B. Recke, J. K. H. Knudsen, and S. B. Jørgensen, "A systematic approach for soft sensor development," *Comput Chem Eng*, vol. 31, no. 5–6, pp. 419–425, 2007, doi: 10.1016/j.compchemeng.2006.05.030.

[26] C. Wei and Z. Song, “Virtual sensors of nonlinear industrial processes based on neighborhood preserving regression model,” *IFAC*, vol. 53, no. 2, pp. 11926–11931, 2020, doi: 10.1016/j.ifacol.2020.12.714.

[27] R. Kalman, “A new approach to linear filtering and prediction problems,” *Transactions of the ASME–Journal of Basic Engineering*, vol. 82, pp. 35–45, 1960, doi: 10.1115/1.3662552.

[28] N. J. Gordon, D. J. Salmond, and A. F. M. Smith, “Novel approach to nonlinear/non-gaussian Bayesian state estimation,” *IEE Proceedings, Part F: Radar and Signal Processing*, vol. 140, no. 2, pp. 107–113, 1993, doi: 10.1049/ip-f-2.1993.0015.

[29] Z. Chen, “Bayesian Filtering: From Kalman Filters to Particle Filters, and Beyond,” *Statistics: A Journal of Theoretical and Applied Statistics*, no. January 2003, 2003, doi: 10.1080/02331880309257.

[30] K. Maes, G. De Roeck, A. Iliopoulos, W. Weijtjens, C. Devriendt, and G. Lombaert, “Kalman filter based strain estimation for fatigue assessment of an offshore monopile wind turbine,” in *Proceedings of ISMA 2016*, 2016, pp. 1649–1661.

[31] R. P. Palanisamy, S. Cho, H. Kim, and S. H. Sim, “Experimental validation of Kalman filter-based strain estimation in structures subjected to non-zero mean input,” *Smart Struct Syst*, vol. 15, no. 2, pp. 489–503, 2015, doi: 10.12989/sss.2015.15.2.489.

[32] B. Friedland, “Treatment of Bias in Recursive Filtering,” *IEEE Trans Automat Contr*, vol. AC-14, no. 4, pp. 359–367, 1969, doi: 10.1109/TAC.1969.1099223.

[33] E. Lourens, E. Reynders, G. Lombaert, G. De Roeck, and G. Degrande, “Dynamic force identification by means of state augmentation: A combined deterministic-stochastic approach,” *Proceedings of ISMA 2010 - International Conference on Noise and Vibration Engineering, including USD 2010*, pp. 2069–2080, 2010.

[34] E. Lourens, E. Reynders, G. De Roeck, G. Degrande, and G. Lombaert, “An augmented Kalman filter for force identification in structural dynamics,” *Mech Syst Signal Process*, vol. 27, no. 1, pp. 446–460, 2011, doi: 10.1016/j.ymssp.2011.09.025.

[35] E. Branlard, D. Giardina, and C. S. D. Brown, “Augmented Kalman filter with a reduced mechanical model to estimate tower loads on a land-based wind turbine: A step towards digital-Twin simulations,” *Wind Energy Science*, vol. 5, no. 3, pp. 1155–1167, 2020, doi: 10.5194/wes-5-1155-2020.

[36] S. J. Julier and J. K. Uhlmann, “Unscented Filtering and Nonlinear Estimation,” in *PROCEEDINGS OF THE IEEE*, 2004.

[37] G. A. Borges, A. N. Vargas, J. Y. Ishihara, and H. M. T. Menegaz, “A systematization of the Unscented Kalman Filter theory,” *IEEE-TAC*, vol. 9286, 2015, doi: 10.1109/TAC.2015.2404511.

[38] M. Jouin, R. Gouriveau, D. Hissel, M. C. Péra, and N. Zerhouni, “Particle filter-based prognostics: Review, discussion and perspectives,” *Mech Syst Signal Process*, vol. 72–73, pp. 2–31, 2016, doi: 10.1016/j.ymssp.2015.11.008.

[39] M. Henkel, W. Weijtjens, and C. Devriendt, “Fatigue Stress Estimation for Submerged and Sub-Soil Welds of Offshore Wind Turbines on Monopiles Using Modal Expansion,” *MDPI Energies*, vol. 14, 2021, doi: https://doi.org/10.3390/en14227576.

[40] T. N. J. Geelen, “Time Domain Force Identification for Noise and Vibration Prediction in Vehicles,” TU Delft, 2019.

[41] K. Tatsis, E. Chatzi, and E. Lourens, “RELIABILITY PREDICTION OF FATIGUE DAMAGE ACCUMULATION ON WIND TURBINE SUPPORT STRUCTURES,” in *UNCECOMP 2017*, 2017, pp. 76–89. doi: 10.7712/120217.

[42] P. Ren and Z. Zhou, “Strain estimation of truss structures based on augmented Kalman filtering and modal expansion,” *SAGE: Advances in Mechanical Engineering*, vol. 9, no. 11, pp. 1–10, 2017, doi: 10.1177/1687814017735788.

[43] E. Lourens and D. J. M. Fallais, “On the use of equivalent forces for structural health monitoring based on joint input-state estimation algorithms,” in *Procedia Engineering*, Elsevier Ltd, 2017, pp. 2140–2145. doi: 10.1016/j.proeng.2017.09.152.

[44] L. Ziegler, U. Smolka, N. Cosack, and M. Muskulus, “Structural monitoring for lifetime extension of offshore wind monopiles: Can strain measurements at

one level tell us everything?," *Wind Energy Science*, vol. 2, no. September, pp. 469–476, 2017, doi: 10.5194/wes-2017-21.

[45] M. Tarpø, B. Nabuco, C. Georgakis, and R. Brincker, "Expansion of experimental mode shape from operational modal analysis and virtual sensing for fatigue analysis using the modal expansion method," *Int J Fatigue*, vol. 130, 2020, doi: 10.1016/j.ijfatigue.2019.105280.

[46] F. K. Moghadam and A. R. Nejad, "Online condition monitoring of floating wind turbines drivetrain by means of digital twin," *Mech Syst Signal Process*, vol. 162, 2022, doi: https://doi.org/10.1016/j.ymssp.2021.108087.

[47] S. Vettori, E. Di Lorenzo, B. Peeters, M. M. Luczak, and E. Chatzi, "An adaptive-noise Augmented Kalman Filter approach for input-state estimation in structural dynamics," *Mech Syst Signal Process*, vol. 184, 2023, doi: 10.1016/j.ymssp.2022.109654.

[48] J. Wang, Y. Zheng, L. Duan, J. Xie, and L. Zhang, "Virtual sensing for gearbox condition monitoring based on extreme learning machine," *JVE INTERNATIONAL LTD. JOURNAL OF VIBROENGINEERING*, vol. 19, no. 2, pp. 1000–1013, 2017, doi: 10.21595/jve.2016.17379.

[49] T. Moi, A. Cibicik, and T. Rølvåg, "Digital twin based condition monitoring of a knuckle boom crane: An experimental study," *Eng Fail Anal*, vol. 112, no. March, p. 104517, 2020, doi: 10.1016/j.engfailanal.2020.104517.

[50] M. González, "Virtual sensor approaches for condition monitoring of vertical transportation systems," PhD, KU Leuven, 2019.

[51] E. Risaliti, B. Cornelis, T. Tamarozzi, and W. Desmet, "A state-input estimation approach for force identification on an automotive suspension component," *Conference Proceedings of the Society for Experimental Mechanics Series*, vol. 3, pp. 359–369, 2016, doi: 10.1007/978-3-319-29754-5_35.

[52] J. Runesson, "Vibration Analysis for Condition Monitoring," Lund University, 2019.

[53] C. Conese, F. Conti, S. Cinquemani, F. M. Bono, A. Zavalloni, and M. Tarabini, "Vibration analysis for condition monitoring of an automatic press machine for thermoplastic polymers," *2021 IEEE International Workshop on*

Metrology for Industry 4.0 and IoT, MetroInd 4.0 and IoT 2021 - Proceedings, pp. 270–274, 2021, doi: 10.1109/MetroInd4.0IoT51437.2021.9488525.

[54] M. Eltabach, S. Sieg-Zieba, G. Song, Z. Li, P. Bellemain, and N. Martin, "Vibration condition monitoring in a paper industrial plant: Supreme project," in *13th International Conference on Condition Monitoring and Machinery Failure Prevention Technologies, CM 2016/MFPT 2016*, 2016.

[55] R. Kurth, M. Alaluss, R. Tehel, W. Reichert, and S. Ihlenfeldt, "Towards Cognitive Forming Machines: Utilization of Digital Twin-Based Virtual Sensors †," *MDPI Engineering Proceedings*, vol. 26, no. 1, 2022, doi: 10.3390/engproc2022026010.

[56] D. Kinet, P. Mégret, K. W. Goossen, L. Qiu, D. Heider, and C. Caucheteur, "Fiber Bragg grating sensors toward structural health monitoring in composite materials: Challenges and solutions," *Sensors (Switzerland)*, vol. 14, no. 4, pp. 7394–7419, 2014, doi: 10.3390/s140407394.

[57] D. Anastasopoulos, M. De Smedt, L. Vandewalle, G. De Roeck, and E. P. B. Reynders, "Damage identification using modal strains identified from operational fiber-optic Bragg grating data," *Struct Health Monit*, vol. 17, no. 6, pp. 1441–1459, 2018, doi: 10.1177/1475921717744480.

[58] R. Soman, "Semi-automated methodology for damage assessment of a scaled wind turbine tripod using enhanced empirical mode decomposition and statistical analysis," *Int J Fatigue*, vol. 134, no. April 2019, 2020, doi: 10.1016/j.ijfatigue.2020.105475.

[59] R. Aghlara and M. M. Tahir, "Measurement of strain on concrete using an ordinary digital camera," *Measurement (Lond)*, vol. 126, no. May, pp. 398–404, 2018, doi: 10.1016/j.measurement.2018.05.066.

[60] M. Arena and M. Viscardi, "Strain State Detection in Composite Structures: Review and New Challenges," *Journal of Composites Science*, vol. 4, no. 2, p. 60, 2020, doi: 10.3390/jcs4020060.

[61] J. Wang, Y. Zheng, P. Wang, and R. X. Gao, "A virtual sensing based augmented particle filter for tool condition prognosis," *J Manuf Process*, vol. 28, pp. 472–478, 2017, doi: 10.1016/j.jmapro.2017.04.014.

[62] W. Weijtjens, T. Verbelen, G. De Sitter, and C. Devriendt, “Foundation structural health monitoring of an offshore wind turbine: a full-scale case study,” *SAGE: Structural Health Monitoring*, pp. 1–14, 2015, doi: 10.1177/1475921715586624.

[63] P. Guo and D. Infield, “Wind turbine tower vibration modeling and monitoring by the nonlinear state estimation technique (NSET),” *MDPI Energies*, pp. 173–196, 2014, doi: 10.1201/b16587.

[64] N. Noppe, A. Iliopoulos, W. Weijtjens, and C. Devriendt, “Full load estimation of an offshore wind turbine based on SCADA and accelerometer data,” *J Phys Conf Ser*, vol. 753, no. 7, 2016, doi: 10.1088/1742-6596/753/7/072025.

[65] D. Augustyn, U. Smolka, U. T. Tygesen, M. D. Ulriksen, and J. D. Sørensen, “Data-driven model updating of an offshore wind jacket substructure,” *Applied Ocean Research*, vol. 104, pp. 1–16, 2020, doi: 10.1016/j.apor.2020.102366.

[66] M. Lydon, S. E. Taylor, D. Robinson, A. Mufti, and E. J. O. Brien, “Recent developments in bridge weigh in motion (B-WIM),” *J Civ Struct Health Monit*, vol. 6, no. 1, pp. 69–81, 2016, doi: 10.1007/s13349-015-0119-6.

[67] D. Hajializadeh, E. J. OBrien, and A. J. O’Connor, “Virtual structural health monitoring and remaining life prediction of steel bridges,” *Canadian Journal of Civil Engineering*, vol. 44, no. 4, pp. 264–273, 2017, doi: 10.1139/cjce-2016-0286.

[68] V. Martínez-Martínez, F. J. Gomez-Gil, J. Gomez-Gil, and R. Ruiz-Gonzalez, “An Artificial Neural Network based expert system fitted with Genetic Algorithms for detecting the status of several rotary components in agro-industrial machines using a single vibration signal,” *Expert Syst Appl*, vol. 42, no. 17–18, pp. 6433–6441, 2015, doi: 10.1016/j.eswa.2015.04.018.

[69] B. Mora, J. Basurko, U. Leturiondo, and J. Albizuri, “Kalman-based virtual sensing for structural health monitoring,” in *DinEst 2021: 2nd Conference on Structural Dynamics*, Gijón, 2021, pp. 22–23.

[70] B. Mora, J. Basurko, I. Sabahi, U. Leturiondo, and J. Albizuri, “Strain Virtual Sensing for Structural Health Monitoring under Variable Loads,” *MDPI Sensors*, vol. 23, no. 10, 2023, doi: 10.3390/s23104706.

[71] B. Mora, J. Basurko, U. Leturiondo, and J. Albizuri, “Strain Virtual Sensing Applied to Industrial Presses for Fatigue Monitoring,” *MDPI Sensors*, 2024.

[72] T. G. Hunter, “Experimental correlation of an n-dimensional load transducer augmented by finite element analysis,” *Wolf Star Technologies, LLC*.

[73] R. E. Kalman, “A new approach to linear filtering and prediction problems,” *Journal of Fluids Engineering, Transactions of the ASME*, vol. 82, no. 1, pp. 35–45, 1960, doi: 10.1115/1.3662552.

[74] R. Zanetti and C. D’Souza, “Recursive implementations of the consider filter,” *Advances in the Astronautical Sciences*, vol. 147, pp. 297–312, 2013.

[75] P. J. Costa, “Adaptive Model Architecture and Extended Kalman-Bucy Filters,” *IEEE Trans Aerosp Electron Syst*, vol. 30, no. 2, pp. 525–533, 1994, doi: 10.1109/7.272275.

[76] H. V. Poor, “On Robust Wiener Filtering,” *IEEE Trans Automat Contr*, vol. 25, no. 3, pp. 531–536, 1980, doi: 10.1109/TAC.1980.1102349.

[77] L. A. McGee and S. F. Schmidt, “Discovery of the Kalman Filter as a Practical Tool for Aerospace and Industry,” *NASA Tech Memo*, no. November, p. 21, 1985, [Online]. Available: http://ntrs.nasa.gov/archive/nasa/casi.ntrs.nasa.gov/19860003843_1986003843.pdf

[78] F. Elies Henar, “Application of a Kalman filter with augmented measurement model in non-invasive cardiac imaging,” *Kalsruhe Institute of Technology*, 2011.

[79] E. Lourens, C. Papadimitriou, S. Gillijns, E. Reynders, G. De Roeck, and G. Lombaert, “Joint input-response estimation for structural systems based on reduced-order models and vibration data from a limited number of sensors,” *Mech Syst Signal Process*, vol. 29, pp. 310–327, 2012, doi: 10.1016/j.ymssp.2012.01.011.

[80] J. R. Magnus, “Gauss on Least-Squares and Maximum-Likelihood Estimation,” *SSRN Electronic Journal*, 2022, doi: 10.2139/ssrn.3990758.

[81] R. Penrose, “A generalized inverse for matrices,” in *Mathematical Proceedings of the Cambridge Philosophical Society*, 1955, pp. 406–413. doi: 10.1017/S0305004100030401.

[82] W. M. Stacey, “A General Modal-Expansion Method for Obtaining Approximate Equations for Linear Systems,” *Nuclear Science and Engineering*, vol. 28, no. 3, pp. 438–442, 1967, doi: 10.13182/nse67-a28958.

[83] K. Graugaard-Jensen, J.; Brincker, Rune; Hjelm, H. P.; Munch, “Modal Based Fatigue Monitoring of Steel Structures Structural Dynamics,” *Structural Dynamics EURODYN 2005*, 2005.

[84] A. Iliopoulos, R. Shirzadeh, W. Weijtjens, P. Guillaume, D. Van Hemelrijck, and C. Devriendt, “A modal decomposition and expansion approach for prediction of dynamic responses on a monopile offshore wind turbine using a limited number of vibration sensors,” *Mech Syst Signal Process*, vol. 68–69, pp. 84–104, 2016, doi: 10.1016/j.ymssp.2015.07.016.

[85] G. P. Nikishkov, “INTRODUCTION TO THE FINITE ELEMENT METHOD,” *Lecture Notes. University of Aizu*. 2004. doi: 10.7142/igakutoshokan.55.211.

[86] W. K. Liu, S. Li, and H. S. Park, “Eighty Years of the Finite Element Method: Birth, Evolution, and Future,” *Archives of Computational Methods in Engineering*, vol. 29, no. 6, pp. 4431–4453, 2022, doi: 10.1007/s11831-022-09740-9.

[87] J. F. Gómez-Aguilar, H. Yépez-Martínez, C. Calderón-Ramón, I. Cruz-Orduña, R. F. Escobar-Jiménez, and V. H. Olivares-Peregrino, “Modeling of a mass-spring-damper system by fractional derivatives with and without a singular kernel,” *MDPI Entropy*, vol. 17, no. 9, pp. 6289–6303, 2015, doi: 10.3390/e17096289.

[88] S. Krenk, “Complex modes and frequencies in damped structural vibrations,” *J Sound Vib*, vol. 270, no. 4–5, pp. 981–996, 2004, doi: 10.1016/S0022-460X(03)00768-5.

[89] M. H. Richardson, “Modal mass, stiffness and damping.” Vibrant Technology, Inc., Jamestown, CA, pp. 1–6, 2000.

[90] F. L. Contreras, “Study of the Model Order Reduction of an Entire Aircraft Configuration,” UPC, 2017.

[91] R. Guyan, “Reduction of stiffness and mass matrices.,” *AIAA J*, vol. 3, no. 2, p. 380, 1965.

[92] M. I. Friswell, S. D. Garvey, and J. E. T. Penny, “Model reduction using dynamic and iterated IRS techniques,” *J Sound Vib*, vol. 186, no. 2, pp. 311–323, 1995.

[93] R. Craig and M. Bampton, “Coupling of Substructures for Dynamic Analyses,” *AIAA J*, vol. 6, no. 7, pp. 1313–1319, 1968.

[94] S. K. Tolani, “Modal truncation of substructures used in vibration analysis,” University of Missouri-Rolla, 1972.

[95] M. Tarpø and M. Vigsø, “Modal Truncation in Experimental Modal Analysis,” in *Topics in Modal Analysis & Testing*, vol. 9, 2019, pp. 143–152. doi: 10.1007/978-3-319-74700-2.

[96] P. Koutsovasilis and M. Beitelschmidt, “Comparison of model reduction techniques for large mechanical systems --- A study on an elastic rod,” in *Multibody Syst Dyn*, 2008, pp. 111–128. doi: 10.1007/s11044-008-9116-4.

[97] E. N. Glass and J. Winicour, “A geometric generalization of Hooke’s law,” *J Math Phys*, vol. 14, no. 9, pp. 1285–1290, 1973, doi: 10.1063/1.1666481.

[98] M. Rupp, M. Eichhorn, and C. Kieleck, “Iterative 3D modeling of thermal effects in end-pumped continuous-wave HO3+:YAG lasers,” *Appl Phys B*, vol. 129, no. 1, pp. 1–11, 2023, doi: 10.1007/s00340-022-07939-z.

[99] W. Schütz, “A history of fatigue,” *Eng Fract Mech*, vol. 54, no. 2, pp. 263–300, 1996, doi: 10.1016/0013-7944(95)00178-6.

[100] J. A. Sauer and G. C. Richardson, “Fatigue of Polymers,” *Int J Fract*, vol. 16, no. 6, pp. 499–532, 1980, doi: 10.1016/B978-0-12-822944-6.00017-7.

[101] F. Kun, H. A. Carmona, J. S. Andrade, and H. J. Herrmann, “Universality behind Basquin’s law of fatigue,” *Phys Rev Lett*, vol. 100, no. 9, 2008, doi: 10.1103/PhysRevLett.100.094301.

[102] R. Wagener and T. Melz, “Fatigue life curve – A continuous Wöhler curve from LCF to VHCF,” *Materials Testing*, vol. 60, pp. 924–930, 2018.

[103] D. Sornette, T. Magnin, and Y. Brechet, “The physical origin of the Coffin-Manson law in low-cycle fatigue,” *Europhys Lett*, vol. 20, no. 5, pp. 433–438, 1992, doi: 10.1209/0295-5075/20/5/009.

[104] E. V. Zaretsky, “A. Palmgren revisited: A basis for bearing life prediction,” *NASA Tech Memo*, 1997.

[105] H. F. Hardrath, “A review of cumulative damage for fatigue.,” in *NASA Langley Research Center*, 1965, pp. 0–16.

[106] M. Prados-Privado, J. C. Prados-Frutos, Á. Manchón, R. Rojo, P. Felice, and J. A. Bea, “Dental implants fatigue as a possible failure of implantologic treatment: The importance of randomness in fatigue behaviour,” *Biomed Res Int*, 2015, doi: 10.1155/2015/825402.

[107] N. Santhosh, U. N. Kempaiah, G. Sajjan, and A. C. Gowda, “Fatigue Behaviour of Silicon Carbide and Fly Ash Dispersion Strengthened High Performance Hybrid Al 5083 Metal Matrix Composites,” *Journal of Minerals and Materials Characterization and Engineering*, vol. 05, no. 05, pp. 274–287, 2017, doi: 10.4236/jmmce.2017.55023.

[108] S. D. Downing and D. F. Socie, “Simple rainflow counting algorithms,” *Int J Fatigue*, vol. 4, no. 1, pp. 31–40, 1982, doi: 10.1016/0142-1123(82)90018-4.

[109] S. R. ; Mettu *et al.*, “NASGRO 3.0 - A SOFTWARE FOR ANALYZING AGING AIRCRAFT S.,” 1999.

[110] J. Fan, X. Guo, and Y. Zhao, “An energetic method to evaluate the macro and micro high-cycle fatigue behavior of the aluminum alloy,” *Journal of Mechanical Engineering Science*, vol. 232, no. 8, pp. 1456–1469, 2018, doi: 10.1177/0954406217742939.

[111] K. O. Ronold and A. T. Echtermeyer, “Estimation of fatigue curves for design of composite laminates,” *Compos Part A Appl Sci Manuf*, vol. 27, no. 6, pp. 485–491, 1996, doi: 10.1016/1359-835X(95)00068-D.

[112] K. Krishnamoorthy and X. Lian, “Closed-form approximate tolerance intervals for some general linear models and comparison studies,” *J Stat Comput Simul*, vol. 82, no. 4, pp. 547–563, 2012, doi: 10.1080/00949655.2010.545061.

[113] A. Hobbacher, “RECOMMENDATIONS FOR FATIGUE DESIGN OF WELDED JOINTS AND COMPONENTS,” 2008.

[114] S. Thakur, K. A. Abhinav, and N. Saha, “Load mitigation using slotted flaps in offshore wind turbines,” *Journal of Offshore Mechanics and Arctic Engineering*, vol. 140, no. 6, 2018, doi: 10.1115/1.4040234.

[115] D. O’Donnell, B. Srbinovsky, J. Murphy, E. Popovici, and V. Pakrashi, “Sensor measurement strategies for monitoring offshore wind and wave energy devices,” *J Phys Conf Ser*, vol. 628, no. 1, 2015, doi: 10.1088/1742-6596/628/1/012117.

[116] J. Weinzettel, M. Reenaas, C. Solli, and E. G. Hertwich, “Life cycle assessment of a floating offshore wind turbine,” *Renew Energy*, vol. 34, no. 3, pp. 742–747, 2009, doi: 10.1016/j.renene.2008.04.004.

[117] W. Dong, T. Moan, and Z. Gao, “Fatigue reliability analysis of the jacket support structure for offshore wind turbine considering the effect of corrosion and inspection,” *Reliab Eng Syst Saf*, vol. 106, pp. 11–27, 2012, doi: 10.1016/j.ress.2012.06.011.

[118] D. S. Li, H. N. Li, and C. P. Fritzen, “The connection between effective independence and modal kinetic energy methods for sensor placement,” *J Sound Vib*, vol. 305, pp. 945–955, 2007, doi: 10.1016/j.jsv.2007.05.004.

[119] M. Seidel, “Substructures for offshore wind turbines: Current trends and developments,” *Festschrift Peter Schaumann*, no. September, pp. 1–6, 2014, doi: 10.2314/GBV.